UNIVERSITY OF WARSAW

FACULTY OF PHYSICS

Submitted to fulfill the requirement for the Doctor of Philosophy degree in Physical Sciences

Temporal Shaping and Measurement of Pulsed Quantum Light

University of Warsaw

Faculty of Physics
Institute of Experimental Physics
Quantum Photonics Lab

Submitted to fulfill the requirement for the Doctor of Philosophy degree in Physical Sciences

Temporal Shaping and Measurement of Pulsed Quantum Light

Author:	Ali Golestani
Advisor:	prof. dr hab. Czesław Radzewicz
Co-Advisor:	dr Michał Karpiński
Submission Date:	June 2023

I confirm that the submitted dissertation is my own work and I have documented all sources and material used except for the quoted literature and other sources mentioned in the dissertation.

Warsaw, June 2023 Ali Golestani

Financial support:

This work was funded in part by the First TEAM (project no. POIR.04.04.00-00-5E00/18) and HOMING (project no. POIR.04.04.00-00-1E2B/16) programs of the Foundation for Polish Science, co-financed by the European Union under the European Regional Development, and in part by the National Science Centre of Poland QuantERA project QuICHE (project no. 2019/32/Z/ST2/00018)

List of abbreviations

QIP	Quantum Information Processing
EOM	Electro-Optic Modulator
EOPM	Electro-Optic Phase Modulator
RF	Radio Frequency
FWHM	Full Width at Half Maximum
RMS	Root Mean Square
TBP	Time Bandwidth Product
GVD	Group Velocity Dispersion
SFG	Sum Frequency Generation
DFG	Difference Frequency Generation
SHG	Second Harmonic Generation
THG	Third Harmonic Generation
FWM	Four Wave Mixing
FROG	Frequency-Resolved Optical Gating
SPIDER	Spectral Phase Interferometry for Direct Electric Field Reconstruction
SSI	Spectral Shearing Interferometry
FBG	Fiber Bragg grating
MZI	Mach–Zehnder Interferometer
PM	Polarization Maintaining
PBS	Polarization Beam Splitter
HWP	Half-Wave Plate
PC	Polarization Controller
FPC	Fiber Polarization Controller
PD	Photodiode
AMP	Amplifier
SMF	Single Mode Fiber
BSC	Babinet-Soleil Compensator
FTS	Fourier Transform Spectroscopy
FTC	Fourier Transform Chronometry
GDD	Group Delay Dispersion
UV	Ultraviolet
DUT	Device Under Test
OFDR	Optical Frequency Domain Reflectometry
TLS	Tunble Laser Source

Abstract

Single photon manipulation and measurement is a critical necessity to quantum information processing and communication. Developing techniques for shaping the flying single-photon states is a crucial task in quantum technology as they should be coherent operations that preserve the quantum state of the photons.In this thesis, the time-frequency degree of freedom is considered for information encoding as it offers a high dimensional information encoding platform. To realize the spectral-temporal pulse shaping, nonlinear optical methods are most often used in optical signal processing but they are not applicable in low light regime. In this thesis, an electro-optic approach is taken to manipulate the single photon in the time-frequency domain which is electro-optic phase modulation. This approach is a coherent and deterministic operation that can be applied to both classical and quantum light pulses.

The first task within the thesis was to characterize the temporal phase modulation process in which a time-varying phase is applied to the optical pulses. In such a scheme, the electro-optic phase modulator is driven by the time varying electronic signal taken from a fast photodiode that is amplified and then synchronized with the optical pulse passing through the modulator. This characterization was performed using the electro=optic sampling technique.

In the second task, a method for measuring single photon pulse envelope is presented. An interferometric optical setup was developed where the optical pulse is employed to measure itself. The optical pulse propagates through a balanced Mach-Zehnder interferometer where a tunable spectral shear is applied to one arm of the interferometer. The frequency of the optical pulse is scanned with respect to its replica in the reference arm. Then a photodiode at the output of the interferometer is used to measure the integrated energy per pulse as a function of the spectral shear. This measurement yields an interference fringe pattern in the spectral domain. One can take the Fourier transform of the interference fringes to obtain the energy envelope of the optical pulse in the time domain. This technique was employed to measure the energy envelope of both classical and quantum light pulses. This novel technique can measure temporal duration of short optical pulses without time-resolved and spectrally-resolved detection and is central wavelength independent and intrinsically free of photon noise.

In the third task, optical devices based on grating structures were fabricated and characterized for passive shaping optical pulses. One promising platform to realize such a device is chirped fiber Bragg grating (CFBG) structures. The CFBGs can be engineered to deliver arbitrary dispersion and spectral profiles. In the CFBG structures, a specific apodization (amplitude) grating profile can be applied through the grating fabrication process, in a way to achieve desired spectral reflectivity response. The group velocity dispersion can also be controlled through engineering the positioning of Bragg gratings inside the optical fiber. In this task, chirped grating samples at telecom and two micron wavelengths with specific dispersion, reflectivity and bandwidth were fabricated.

In summary, I worked on advancing the use of electro-optic approach for manipulation of short optical pulses that is applicable in both classical and quantum regimes. The presented approach gives an active control for shaping of optical pulses. Based on this electro-optic approach, the tunable spectral shearing interferometry technique for measuring single photon pulse was introduced. In addition, the chirped Bragg grating structures for passive shaping of optical pulses was fabricated. These sets of developed optical devices open new ways in optical pulse shaping for quantum information processing and communication.

Strzeszczenie

Modyfikacja własności pojedynczych fotonów i ich pomiar są kluczowe z punktu widzenia przetwarzania informacji oraz komunikacji kwantowej. Opracowanie technik kształtowania impulsów jednofotnowych to istotne zagadnienie w ramach technologii kwantowych, gdyż powinny to być operacje spójne, które zachowują stan kwantowy fotonów. Różne stopnie swobody pojedynczych fotonów mogą być wykorzystane do przetwarzania informacji kwantowej. W tej pracy rozważany jest stopień czasowo-widmowy, gdyż umożliwia wielowymiarowe kodowanie informacji. Do realizacji czasowo-widmowego kształtowania impulsów w optycznym przetwarzaniu sygnałów zwykle stosuje się metody optyki nieliniowej, które nie mają zastosowania dla słabych sygnałów. W tej pracy wykorzystano elektro-optyczną modulację fazy do realizacji przekształceń pojedynczych fotonów w domenie czasowo-widmowej. To podejście umożliwia realizację spójnych i deterministycznych przekształceń, które można zastosować zarówno dla klasycznych, jak i kwantowych impulsów światła.

Pierwszym zadaniem było scharakteryzowanie procesu czasowej modulacji fazy. W tym schemacie elektrooptyczny modulator fazy jest sterowany przez zmienny w czasie sygnał elektroniczny wytwarzany przez szybką fotodiodę, który jest wzmacniany, a następnie synchronizowany z impulsem optycznym przechodzącym przez modulator. Charakteryzacja została przeprowadzona przy użyciu techniki próbkowania elektro-optycznego.

W kolejnej części pracy przedstawiono metodę pomiaru obwiedni impulsu pojedynczego fotonu. Opracowano interferometryczny układ optyczny, w którym impuls optyczny jest wykorzystywany do pomiaru samego siebie. Impuls przechodzi przez zrównoważony interferometr Macha-Zehndera. W jednym ramieniu interferometru impuls jest przesuwany widmowo: częstotliwość impulsu jest skanowana względem sygnału w ramieniu odniesienia. Następnie fotodioda na wyjściu interferometru mierzy scałkowaną energię na impuls w funkcji przesunięcia widmowego. W wyniku pomiaru uzyskuje się prążki interferencyjne w domenie widmowej. Transformata Fouriera prążków pozwala otrzymać obwiednię energii impulsu w dziedzinie czasu. Technikę tę wykorzystano do pomiaru obwiedni zarówno klasycznych, jak i kwantowych impulsów światła. Ta nowa technika pozwala mierzyć czas trwania krótkich impulsów optycznych bez wykorzystania detekcji z rozdzielczością czasową i spek-

tralną. Ponadto jest niezależna od centralnej długości fali sygnału i wolna od szumów optycznych.

W ostatniej części pracy opisano fabrykację i charakteryzację pasywnych struktur periodycznych do kształtowania impulsów światła. Jedną z obiecujących platform do realizacji takich przekształceń są światłowodowe siatki Bragga ze zmiennym okresem (ang. chirped fiber Bragg gratings, CFBG). CFBG można zaprojektować tak, aby zapewniały dowolne profile dyspersji i odpowiedzi widmowej. Możliwe jest zastosowanie apodyzacji kontrastu struktury CFBG w celu uzyskania pożądanej odpowiedzi widmowej dla sygnałów odbitych od struktury. Ponadto możliwe jest kontrola dyspersji prędkości grupowej poprzez odpowiednie pozycjonowania struktur braggowskich wzdłuż światłowodu. Opisano wytwarzanie światłowodowych siatek Bragga o określonych dyspersjach, współczynnikach odbicia oraz pasmach dla telekomunikacyjnych długości fali oraz dla długości fali powyżej 2 um.

Podsumowując, pracowałem nad rozwojem podejścia elektro-optycznego do modyfikacji krótkich impulsów optycznych, które ma zastosowanie zarówno dla sygnałów klasycznych, jak i kwantowych. Przedstawione podejście umożliwia aktywne kształtowanie impulsów optycznych. W oparciu o to podejście wprowadzono technikę przestrajalnej interferometrii z przesunięciem widmowym do pomiaru impulsów jednofotnowych. Ponadto wyprodukowano światłowodowe siatki Bragga do pasywnego kształtowania impulsów optycznych. Opracowane techniki i struktury optyczne otwierają nowe możliwości kształtowania impulsów optycznych na potrzeby kwantowego przetwarzania informacji i komunikacji kwantowej.

Contents

List of Figures

Chapter 1

Introduction to time-frequency optical modes

1.1 Encoding information into light

In classical computation, the fundamental unit of information is the bit, which is typically represented by a 0 or 1. Any physical system that has two possible distinct states, such as two distinct energy levels, can be used to represent a single bit of information. By extension, quantum computation and communication rely on the use of quantum bits, or qubits, as the basic unit of information. The state of a qubit can be represented as either $|0\rangle$ or $|1\rangle$ in quantum mechanics notation. However, unlike classical bits, which can only be in one of these two states at a time, qubits can exist in a superposition of both states simultaneously. In order to represent a qubit, the physical system that is being used must have the capability to exhibit all of the possible superpositions of states that a qubit can take on. This means that the physical system must be able to exist in a linear combination of multiple quantum states simultaneously, rather than just a single state at any given time. To encode qubits into photons, we utilize various physical states of light's degrees of freedom. These states can include the horizontal and vertical polarization modes, various spatial distributions (transverse modes) and longitudinal modes of electromagnetic wave that can be independently controlled and modified. In this thesis, the focus is primarily on using the frequency and time degrees of freedom of light to encode the information.

1.1.1 Time-Frequency degree of freedom

Time-Frequency encoding

So far, most experimental efforts to manipulate quantum states have focused on using spatial degrees of freedom [1]. However, modern telecommunications offer

a promising alternative or complementary approach that relies on time-frequency encodings. This method can provide access to high-dimensional Hilbert spaces [2] while still keeping the compact design of the optical devices. It also takes advantage of the existing infrastructure for classical optical communication systems. In addition, time-frequency encodings are relatively insensitive to inhomogeneities in the medium through which they are transmitted [3, 4].

Polarization and path encodings have been important in the development of basic functions in photonic quantum information processing [5]. However, the limited two-dimensional Hilbert space of polarization states in spatial encodings suggest that other degrees of freedom should also be considered. Time-frequency properties offer a promising alternative. Time-frequency modes can have a high dimensionality, can exist within a single spatial mode, and can be used with existing techniques for multiplexing and modulation in classical optical communications. Time-frequency encodings can be divided into three main categories: time bins [4], which are based on temporal properties; frequency bins [6], which are based on spectral properties; and temporal modes [7], which involve both temporal and spectral properties.

Time bins

A time-bin qubit is a type of quantum information that is encoded in the relative arrival times of light pulses. The first time-bin encoding was introduced by Franson in the context of the violation of Bell inequalty that was dependent upon interference between the probability amplitudes associated with pair of photons that have been generated at various times [8]. In general, the time-bins acn be generated by sending a short pulse of light through an unbalanced interferometer in which the light is split into two paths which then are combined again. Consider a single-photon wave packet passing through a two-path Mach-Zehnder interferometer: if the two paths have different lengths, the photon wave packet will exit the interferometer in a quantum-mechanical superposition of an "early time bin" and "later time bin" [9]. Note that the interferometer is required to be stable by controlling its temperature. By adjusting the parameters of the interferometer to control the relative phase and amplitude, one can accurately produce arbitrary time-bin qubits that can be used to store and process quantum information. This superposition describes a photon that is present in two time bins, which are separated by a time difference that is much larger than the coherence time of the photon. The time bins are defined by the difference in the optical path length between the short and long arms of the interferometer [10].

This method of encoding qubits is particularly robust and well-suited for long-distance quantum communication and fundamental experiments since they are not sensitive to polarization fluctuation in optical fibers [9]. Using the time-bin degree of freedom to encode qubits allows for the transmission of quantum information

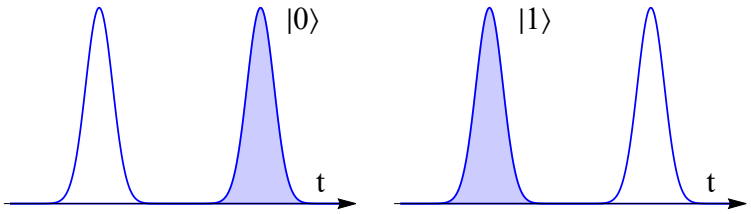

Figure 1.1: Representation of time-bin states in which information is encoded in the arrival time of the light pulses

over long distances with very little decoherence and with high fidelity, making it a promising approach for practical applications in quantum communication and computing [4, 11]. The time-bins are also a basis for implementation of quantum key distribution schemes to achieve high key generation rate where the idea is to acquire the secret bits by simple measurement of time of arrival [12, 13].

Frequency bins

In quantum information processing (QIP) in the spectral domain, the fundamental unit of information is the frequency-bin qubit. This is a single photon that occupies a coherent superposition of two narrowband frequency modes, meaning that it exists simultaneously in both modes. This superposition can be created using electro-optic phase modulators (EOMs), which are devices that can control the phase of light passing through them. The EOMs work by applying a periodic voltage at a frequency equal to the spacing between the two frequency bins. This causes the phase of the light to vary periodically, creating an interference pattern between the two bins. However, EOMs also introduce upper and lower sidebands around the bins of interest at a distances equal to multiples of the modulating frequency. These additional frequencies that are created as a result of the modulation process can scatter the photon energy outside of the intended qubit Hilbert space. This can lead to errors in the QIP process and reduce the overall efficiency of the system. Therefore, it is important to minimize the scattering of photon energy outside of the intended qubit Hilbert space in order to improve the performance of spectral QIP systems [14, 15].

In the context of two-color interference, one approach is nonlinear mixing of strong classical pumps based on four-wave mixing Bragg scattering. In this scheme, two pumps generate a grating through interference that translates the frequency of the initial state to a new frequency without adding noise [16]. However, another approach that can be used is to employ a system based on alternating series of electro-optic modulators (EOMs) and pulse shapers which is known as a "quantum frequency processor" [6]. Frequency bins have also been generated in integrated photonic

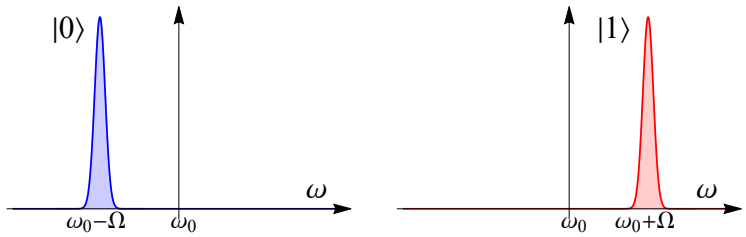

Figure 1.2: Representation of frequency-bin states in which information is encoded in different frequencies of the light pulses.

platforms [15] based on coherently pumped multiple micro-ring resonators in which each resonator generates photons in specific frequency bin and its separation is independent of the micro-ring's free spectral range. This approach offers a scalable and efficient way of frequency-bin generation [17].

Frequency bins offer several practical advantages such as multiplexing, or the ability to transmit multiple signals simultaneously over a single channel. This is because frequency bins can be used to clearly distinguish between different signals based on their frequency. Frequency bins also provide high-resolution measurement capabilities, allowing for precise measurement of the frequency of a signal. Additionally, the use of frequency bins places relatively moderate demands on the jitter, or timing instability, of photon detectors, making them a suitable choice for applications where precise timing is important [6]. Finally, frequency bins are particularly applicable for scalable on-chip photonics, as they allow for the simultaneous processing of many qubits in parallel, and recent demonstrations have shown that they can be used to produce high-dimensional entangled states [18].

Temporal modes

The time-frequency degree of freedom of an optical pulse can be employed by encoding quantum information in photonic temporal modes [7] in which information is encoded in both the time and frequency domains of the optical signal. In this approach, the information is encoded in the complex time-frequency amplitude of the electric field of single photons. The Hilbert space, or the set of all possible quantum states, available in the time-frequency domain is unlimited, allowing for high-dimensional encodings. This is in contrast to spatial encodings, which are limited by the physical size of the system. Time-frequency encodings are also intrinsically compatible with waveguides and fiber transmission, making them a useful tool for transmitting quantum information over long distances. Temporal-mode bases can be represented in different forms in either time or frequency as long as they provide an orthonormal basis [19] as illustrated in Figure 1.3.

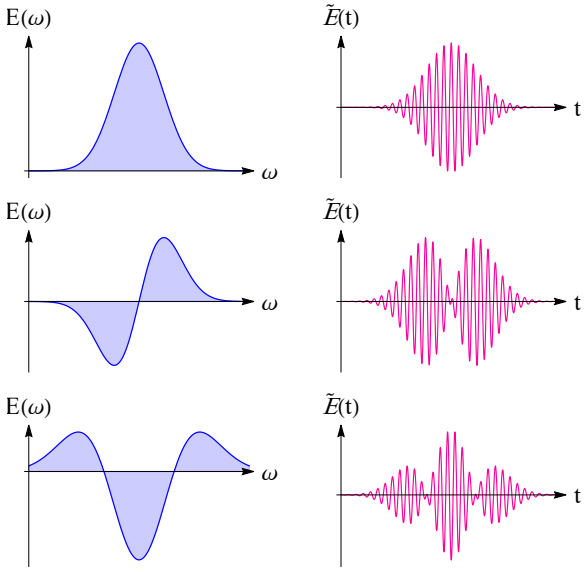

Figure 1.3: Representation of classical temporal modes basis in the frequency and time domains. For applications in QIP, single photons are considered in superposition of such modes.

Temporal modes are considered as another flexible and high-dimensional basis for the time-frequency degree of freedom of light. One example of temporal modes is the Hermite-Gauss modes, which are analogous to the Hermite-Gauss spatial modes in which modes overlap in time and frequency, but each mode is mutually orthogonal. Temporal modes can be generated using parametric down-conversion, a nonlinear optical process that involves the conversion of photons of one frequency to photons of lower frequency [19].

1.2 Spectral-Temporal electric field

The electric field can be described in either time or frequency domain. The real electric field in temporal domain can be written as follows

$$\mathcal{E}(t) = E(t) + E^*(t), \tag{1.1}$$

where $E(t)$ is defined as the complex electric field and $E^*(t)$ is the complex conjugate of the electric field. The complex electric filed can be expressed in terms of an amplitude and phase as

$$E(t) = |E(t)| \exp[i(\phi(t) + \phi_0 - \omega_0 t)], \tag{1.2}$$

where $|E(t)|$ is time-dependent envelope function, $\phi(t)$ is time-dependent phase function, ϕ_0 is initial phase and ω_0 is the carrier angular frequency. In this representation, the square of the envelope function expresses the temporal intensity as

$$I(t) \propto |E(t)|^2. \tag{1.3}$$

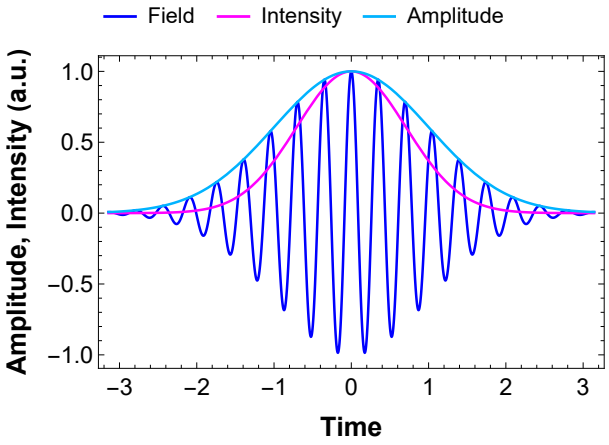

Figure 1.4: Representation of electric field, amplitude of the electric field (real part) and intensity of the electric field in time domain.

The complex temporal electric filed and the complex spectral electric field are linked to each other through the Fourier transform as follows

$$\tilde{E}(\omega) = \frac{1}{2\pi}\int_{-\infty}^{\infty} dt E(t)\exp[i\omega t] = |\tilde{E}(\omega)|\exp[i\varphi(\omega)], \tag{1.4}$$

in this representation, $\tilde{E}(\omega)$ is spectral amplitude and $\mathrm{Arg}[\tilde{E}(\omega)]$ is the spectral phase. Therefore the spectral intensity is expressed as

$$\tilde{I}(\omega) \propto |\tilde{E}(\omega)|^2. \tag{1.5}$$

1.2.1 Moments of the electric field

Working with ultrashort optical pulses requires us to have primary information about main characteristics of the optical pulse such as pulse shape and its temporal and spectral width. This information allows to model and study the optical transformations and operations that are applied to the optical pulse. In this context, definig the temporal width Δt and spectral width $\Delta\omega$ of the optical pulse is crucial in optical experiments. There are multiple definitions to describe these quantities, the most widely used is the full width at half maximum (FWHM) as the quantity representative

of the pulse duration. However, pulse temporal and spectral width determined by the FWHM values are not always suitable measures. In practice, the optical pulse may not be ideally symmetric or its distribution has broad wings causing a considerable part of the energy to be outside the range given by the FWHM. In these cases, it is more accurate to use averaged values derived from the statistical moments of the field's intensity envelope. In this regard, the second-order moment of the field distribution gives better estimation of the temporal and spectral width of the optical pulse which involves calculating the second moment of the intensity profile of the optical pulse. In general, for a given function $f(x)$ as a function of the variable x, the moment of order n for the quantity x with respect to its intensity profile is expressed as [20]

$$\langle x^n \rangle = \frac{\int_{-\infty}^{\infty} x^n |f(x)|^2 dx}{\int_{-\infty}^{\infty} |f(x)|^2 dx}, \tag{1.6}$$

where $|f(x)|^2$ is the intensity profile of the given function. A good criterium for the width of a distribution can estimated using the Root Mean Square (RMS) width concept as

$$\langle \Delta x \rangle = \sqrt{\langle x^2 \rangle - \langle x \rangle^2}, \tag{1.7}$$

where the first term under the square root is the variance of the distribution function and the second term is the mean of the distribution function. Considering an electric field distribution in temporal domain, $E(t)$, the first-order moment, $\langle t \rangle$, of the electric field intensity distribution is defined as

$$\langle t \rangle = \frac{\int_{-\infty}^{\infty} t |E(t)|^2 dt}{\int_{-\infty}^{\infty} |E(t)|^2 dt}, \tag{1.8}$$

and the second-order moment is also expressed as

$$\langle t^2 \rangle = \frac{\int_{-\infty}^{\infty} t^2 |E(t)|^2 dt}{\int_{-\infty}^{\infty} |E(t)|^2 dt}. \tag{1.9}$$

Considering the definition for calculating the width of a distribution function in Equation 1.7, the temporal and spectral widths can be calculated by following equations

$$\langle \Delta t \rangle = \sqrt{\langle t^2 \rangle - \langle t \rangle^2}, \tag{1.10}$$

$$\langle \Delta \omega \rangle = \sqrt{\langle \omega^2 \rangle - \langle \omega \rangle^2}. \tag{1.11}$$

The temporal and spectral widths are related through the time–energy uncertainty principle

$$\langle \Delta t \rangle \langle \Delta \omega \rangle \geq \frac{1}{2}. \tag{1.12}$$

1.2.2 Gaussian optical pulse

The temporal shape of optical pulses that are commonly used in ultrafast optical experiments can be approximately described with a Gaussian function as

$$E(t) = E_0 \exp\left[-\frac{t^2}{2T_0^2}\right], \tag{1.13}$$

where T_0 is the temporal duration of the transform-limited Gaussian optical pulse. By taking the Fourier transform, the Gaussian pulse in the spectral domain is expressed as

$$\tilde{E}(\omega) = \frac{1}{2\pi}\int_{-\infty}^{\infty} E_0 \exp\left[-\frac{t^2}{2T_0^2}\right] \exp\left[-i\omega t\right] dt = \frac{E_0 T_0}{\sqrt{2\pi}} \exp\left[-\frac{T_0^2}{2}\omega^2\right]. \tag{1.14}$$

By considering the full width at half-maximum of the Gaussian pulse in time and frequency domains, the relation between the temporal FWHM, Δt, and the spectral FWHM, $\Delta\omega$, can be calculated as

$$\exp\left[-\frac{t^2}{2T_0^2}\right] = \frac{1}{2} \Rightarrow \Delta t = 2T_0\sqrt{\ln 2}, \tag{1.15}$$

$$\exp\left[-\frac{T_0^2}{2}\omega^2\right] = \frac{1}{2} \Rightarrow \Delta\omega = 2\frac{\sqrt{\ln 2}}{T_0}. \tag{1.16}$$

For the Gaussian optical pulses, the relation between spectral bandwidth and the temporal duration, i.e. the time-bandwidth product, is defined as:

$$\Delta\omega\Delta t = 4\ln 2 \Rightarrow \Delta\nu\Delta t = 0.441. \tag{1.17}$$

1.3 Pulse propagation through dispersive media

Having introduced the Gaussian pulse characteristics, we continue to study how its temporal and spectral widths changes when an optical pulse propagates through a linear dispersive medium. First, I consider a monochromatic and paraxial beam propagating in spatial domain and later, I will use space-time analogy to describe

pulse propagation in temporal domain. The space-time anology has been fully described by Víctor Torres-Company in [21]. Starting from Maxwell's equations, one can obtain the wave equation for a scalar field that is used to describe propagation of the optical beam in the dielectric medium:

$$\nabla^2 E(\vec{r},t) - \frac{1}{c^2}\frac{\partial^2 E(\vec{r},t)}{\partial t^2} = \frac{\partial^2 P(\vec{r},t)}{\partial t^2}, \tag{1.18}$$

where $E(\vec{r},t)$ is the electric field, $P(\vec{r},t)$ is the dielectric polarization and c is the speed of light in vacuum. In this equation, the symbol ∇^2 indicates the Laplace operator. The dielectric polarization stands for the impact of the medium on propagation of the optical pulse. For the monochromatic and paraxial beam propagation and assuming that the propagating beam is not effected by the external charges, $P = 0$, the wave equation leads to Helmholtz equation

$$(\nabla^2 + k_0)\mathcal{E}(\vec{r}) = 0, \tag{1.19}$$

where k_0 is the propagation constant and the $\mathcal{E}(\vec{r})$ is the time-independent complex amplitude of the electric field:

$$E(\vec{r},t) = \mathcal{E}(\vec{r})\exp\left[i\omega_0 t\right], \tag{1.20}$$

with ω_0 being the angular frequency and $k_0 = \omega_0/c$.

In order to reduce the wave equation to first order, the slowly varying envelope approximation is usually considered. This approximation requires that the envelope of the traveling optical pulse varies slowly in time and space compared to the period and wavelength, respectively. In this case, it is assumed that the pulse duration is much larger than the carrier oscillation period. Considering the Cartesian coordinates and assuming that the optical beam travels along the z-axis, the paraxial Helmholtz equation in one-dimension is simplified as [21]

$$i\frac{\partial}{\partial z}\mathcal{E}(x;z) = -\frac{1}{2k_0}\frac{\partial^2}{\partial x^2}\mathcal{E}(x;z). \tag{1.21}$$

The propagation behavior of the optical pulse in dispersive medium is determined by the dispersion relation. Due to wavelength dependency of the refractive index $n(\lambda)$, different wavelength components of the optical pulse, travel at different speeds so that the optical pulse experiences a change in temporal domain when it propagates in the dispersive medium. The dispersion is expressed as the frequency dependent phase

$$\Phi(\omega,z) = \beta(\omega)z, \tag{1.22}$$

where $\beta(\omega)$ is the propagation coefficient. For narrowband optical pulses, this coefficient can be approximated by a propagation constant while for a broadband pulse different phase changes are accumulated throughout the propagation for the different wavelength components of the optical pulse. This is due to wavelength dependency of the refractive index as

$$\beta(\omega) = n(\omega)\frac{\omega}{c}. \tag{1.23}$$

In this case, the Taylor expansion of the frequency dependent propagation coefficient is used to study the impact of the dispersion to the optical pulse. The Taylor expansion of $\beta(\omega)$ is expressed as [21]

$$\beta(\omega) = \beta_0 + \beta_1(\omega - \omega_0) + \frac{\beta_2}{2!}(\omega - \omega_0)^2 + \frac{\beta_3}{3!}(\omega - \omega_0)^3 + ... \tag{1.24}$$

where ω_0 is the central angular frequency and β_n is the nth-order dispersion coefficient of the medium as

$$\beta_n = \frac{d^n\beta(\omega)}{d\omega_m}|_{\omega-\omega_0} \quad , \quad n = 0, 1, 2, 3, ... \tag{1.25}$$

Considering the Equation 1.24, the first term is referred as the phase velocity of the central frequency and the second term is related to the group velocity of the optical pulse. The third term, β_2 is the group velocity dispersion (GVD) coefficient that introduces a parabolic phase with respect to the central frequency of the optical pulse. The GVD introduces a chirp in which the instantaneous frequency of the optical pulse is increasing or decreasing. The optical pulse with increasing instantaneous frequency, positive β_2, is called the up-chirp and the decreasing instantaneous frequency, negative β_2, corresponds to the down-chirp as illustrated in Figure 1.5.

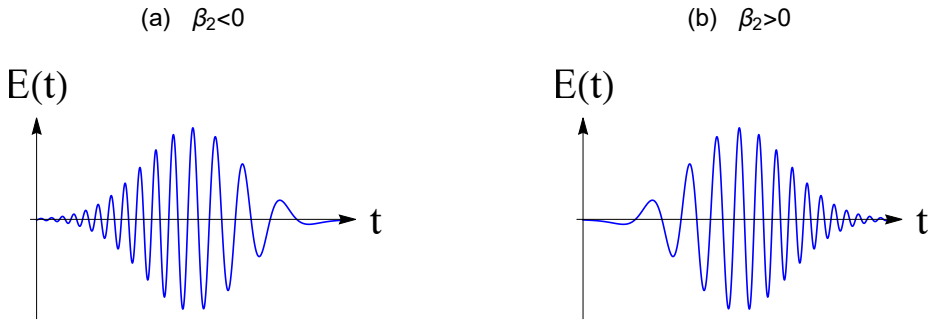

Figure 1.5: Representation of chirped optical pulse. a) negatively chirped $\beta_2 < 0$ and b) positively chirped $\beta_2 > 0$

Now, the impact of dispersion on Gaussian optical pulse, as defined in Equation 1.13, propagating in a linear dispersive medium is investigated. Considering the paraxial Helmholtz equation, Equation 1.21, and using the space-time analogy [22], the pulse propagation equation in temporal domain is expressed as

$$i\frac{\partial E(z,t)}{\partial z} = \frac{\beta_2}{2}\frac{\partial^2 E(z,t)}{\partial t^2}, \tag{1.26}$$

this equation can be solved by using Fourier transform. If $\tilde{E}(z,\omega)$ is the Fourier transform of the $E(z,t)$ such that

$$E(z,t) = \frac{1}{2\pi}\int_{-\infty}^{\infty} \tilde{E}(z,\omega)\exp\left[-i\omega t\right]d\omega, \tag{1.27}$$

that satisfies the following ordinary differential equation as

$$i\frac{\partial \tilde{E}(z,\omega)}{\partial z} = -\frac{1}{2}\beta_2\omega^2\tilde{E}(z,\omega). \tag{1.28}$$

The solution for the equation is an exponential as

$$\tilde{E}(z,\omega) = \tilde{E}(0,\omega)\exp\left[\frac{i}{2}\beta_2\omega^2 z\right]. \tag{1.29}$$

This indicates that by applying the dispersion, the phase of each spectral component of the optical pulse is changed that depends on both the frequency and the propagation distance. The applied dispersion does not effect the pulse in the spectral domain while it modifies the optical pulse shape in the temporal domain. By substituting Equation 1.27 in Equation 1.29, the general solution of Equation 1.26 is expressed by

$$E(z,t) = \frac{1}{2\pi}\int_{-\infty}^{\infty} \tilde{E}(0,\omega)\exp\left[\frac{i}{2}\beta_2\omega^2 z\right]\exp\left[-i\omega t\right]d\omega, \tag{1.30}$$

where $\tilde{E}(0,\omega)$ is the Fourier transform of the initial Gaussian pulse that can be calculated as following

$$\tilde{E}(0,\omega) = \int_{-\infty}^{\infty} E(0,t)\exp\left[i\omega t\right]dt. \tag{1.31}$$

By considering the initial Gaussian pulse as defined in Equation 1.13 and substituting Equation 1.31 into Equation 1.30, the optical pulse after propagating length of z through the dispersive medium in the temporal domain is calculated as

$$E(z,t) = E_0\frac{T_0}{\sqrt{T_0^2 - i\beta_2 z}}\exp\left[-\frac{t^2}{2(T_0^2 - i\beta_2 z)}\right]. \tag{1.32}$$

Considering the exponent part of this relation that consists both real and imaginary components, and performing mathematical calculations, the temporal broadening of the optical pulse can be calculated as [23]

$$\exp\left[-\frac{t^2}{2(T_0^2 - i\beta_2 z)}\right] = \exp\left[-\frac{t^2}{2T^2(z)} - i\frac{\beta_2 z}{2(T_0^4 + \beta_2^2 z^2)}t^2\right], \tag{1.33}$$

where

$$T^2(z) = \frac{T_0^4 + \beta_2^2 z^2}{T_0^2}, \tag{1.34}$$

So temporal width of the optical pulse as a function of propagating length, z, through the dispersive medium is given by

$$T(z) = T_0\sqrt{1 + (\frac{z}{L_D})^2}, \tag{1.35}$$

where $L_D = T_0^2/|\beta_2|$ is called dispersion length.

1.4 Nonlinear optical effects

The advent of nonlinear optics has opened new ways to develop optical pulse characterization techniques and generate quantum light states. Furthermore, manipulation of light properties via nonlinear interaction of light and matter is used to spectrally modify optical light pulses. In the current thesis, a linear approach for optical pulse characterization will be proposed but before that, previously developed nonlinear techniques is being reviewed.

In nonlinear optics, an optical media exhibit nonlinear response when an electric field is applied to the medium. In such interaction, the optical properties of the medium change as the intensity of the electric field increases. In such a condition, the refractive index and consequently the speed of light in the medium depends on intensity of the applied electric field. This nonlinear interaction also leads to interesting effects such as frequency conversion of light as it passes through the medium. These effects make it possible to control the propagation of the light in the medium [24].

In the context of nonlinear interaction of light with dielectric medium, the response of the medium is described by the higher orders of nonlinear relation between polarization density and applied electric field as

$$\mathcal{P}(t) = \varepsilon_0[\chi^{(1)}E(t) + \chi^{(2)}E^2(t) + \chi^{(3)}E^3(t) + ...], \tag{1.36}$$

where ε_0 is the permittivity of free space and χ is known as optical susceptibility. The second order nonlinear interaction leads to phenomena like frequency conversion in

which mixing of two monochromatic waves generates a wave at a frequency that is sum or difference frequency of the incident wave that are known as sum frequency generation (SFG) and difference frequency generation (DFG), frequency doubling of a monochromatic wave that is referred as second harmonic generation (SHG). However, third order nonlinear interaction offers applications such as third harmonic generation (THG), self-phase modulation, self-focusing and four wave mixing (FWM). In this section, some of these effects that are commonly employed in characterization techniques of classical light pulses are reviewed [25].

1.4.1 Second Harmonic Generation

The second harmonic generation (SHG) is a second order nonlinear effect that appears in noncentrosymmetric crystals. This effect can not be demonstrated in centrosymmetric materials due to the inversion symmetries in polarization and electric field [26]. The SHG is a coherent optical process associated with radiation of dipoles in the material. The dipoles oscillate not only with the applied electric field (pump wave) at frequency of ω but also at the frequency of 2ω, then as result of interaction of the applied filed with the material, the second-harmonic wave with doubled frequency of 2ω is generated as dipicted in Figure 1.6.

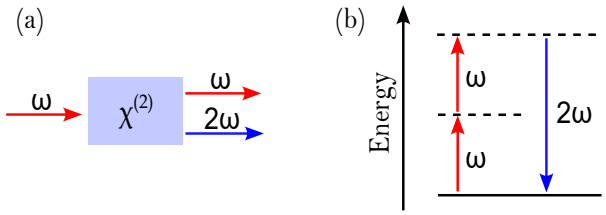

Figure 1.6: a) Schematic of second harmonic generation process. b) Energy level diagram representing second harmonic generation. The dashed lines represent virtual energy levels.

As result of this process, energy is transferred from pump wave to the second-harmonic wave. Major application of the SHG process is to convert a laser beam at specific wavelength to a laser beam operating in different spectral region. The SHG process can also be seen in terms of the exchange of photons between the different frequency components of the electric field so that two photons with frequency ω are destroyed to form a new photon with frequency of 2ω through a quantum mechanical process.

1.4.2 Sum and Difference Frequency Generation

Sum frequency generation (SFG) is a second-order nonlinear optical process in which two optical fields with distinct frequency components ω_1 and ω_2 propagate through a second-order nonlinear crystal to generate a new wave with frequency of the sum of the input frequencies, $\omega_3 = \omega_1 + \omega_2$. In fact, the SHG process is a special case of the SFG process. This nonlinear interaction can also be designed in different way to implement down conversion process that is called difference frequency generation (DFG). This is realized by an interaction between waves ω_3 and ω_2 to generate wave ω_1 as illustrated in Figure 1.7, $\omega_1 = \omega_3 - \omega_2$. The SFG and DFG processes are commonly used to generate light at wavelengths at which no coherent light sources are available.

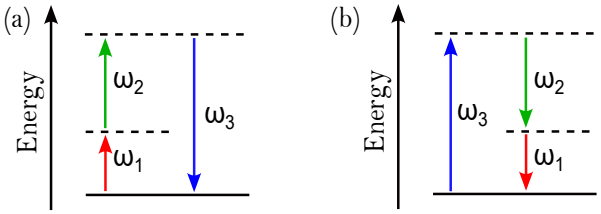

Figure 1.7: Energy level diagram representing sum (a) and difference (b) frequency generation. The dashed lines represent virtual energy levels.

1.5 Optical pulse characterization techniques

The temporal duration of ultrashort optical pulses can be on the order of picoseconds or less, however, modern electronic measurement devices are not able to accurately detect such short optical pulses. In principle, in order to measure the temporal duration of any event, an event shorter than that event is required [25]. The solution is to gate the pulse with itself and establish interferometric measurement techniques.

For performing experiments using laser pulses, it is crucial to have information about the characteristics of the laser pulse that is being used. Such information helps researchers to have better understanding about the experiment when they make interaction between laser and the matter. For this purpose, autocorrelation and spectrum analysis measurement techniques have been developed in either the time domain or the frequency domain. However, performing separate measurements in time and frequency domains do not yield a precise information about the laser pulse duration and phase evolution. A simultaneous measurements in both time and frequency domain are required to more precisely measure intensity and phase characteristics of ultrashort optical pulses.

In this section, a brief review of main developed optical pulse characterization techniques is presented. Some of them only estimate the optical pulse duration while others are able to measure both the spectral intensity and the spectral phase profiles of the optical pulse from which the complete optical pulse characterization can be obtained. The most well known techniques for measuring the temporal profile of the electric field rely on nonlinear optical interactions. Here we begin to describe techniques based on intensity autocorrelation and then move on to techniques that have been developed to characterize the full electric field, such as frequency resolved optical gating (FROG) and spectral phase interferometry for direct electric field reconstruction (SPIDER).

1.5.1 Autocorrelation techniques

Autocorrelation optical setups were the first tools employed to characterize the optical pulses. In this regard, several methods have been introduced with different capabilities in delivering information about the shape, temporal duration, spectrum and phase profile of the optical pulse [27, 28, 29].

Fourier transform spectrometry

One of the most common technique for optical pulse characterization is Fourier transform spectrometry. It is basically a Michelson interferometer in which the input pulse is split into two identical replicas and after introducing a time delay τ in one arm of the interferometer then are recombined. The optical setup of the measurement is shown in Figure 1.8. The measurement consists of recording the average power using a photodiode at the output of the interferometer that gives the interference signal as a function of delay. Then by taking Fourier transform of the interference signal, the optical pulse in spectrum is achieved [30].

The output field measurement at the output of the interferometer can be written as

$$I(\tau) = \int_{-\infty}^{+\infty} |E(t) + E(t-\tau)|^2 dt. \tag{1.37}$$

By expanding the equation as in [25]

$$I(\tau) = \int_{-\infty}^{+\infty} |E(t)|^2 dt + \int_{-\infty}^{+\infty} |E(t-\tau)|^2 dt + 2Re\{\Gamma^{(2)}(\tau)\}, \tag{1.38}$$

where $\Gamma^{(2)}(\tau)$ is called light's second-order coherence function and is defined as

$$\Gamma^{(2)}(\tau) = I(\tau) = \int_{-\infty}^{+\infty} E(t)E^*(t-\tau)dt. \tag{1.39}$$

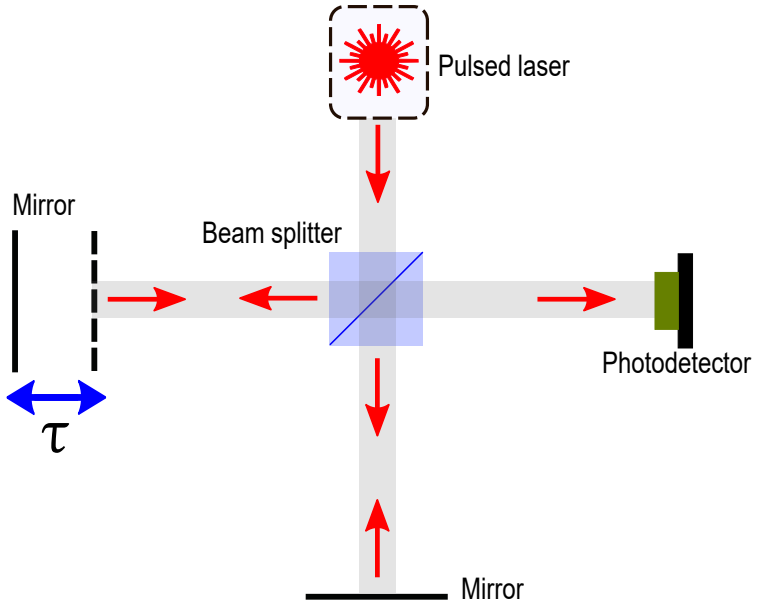

Figure 1.8: Michelson interferometer setup for measuring the electric field autocorrelation function.

Based on the Wiener–Khinchin theorem [31, 32], Fourier transform of the field autocorrelation, $\Gamma^{(2)}(\tau)$, gives the spectrum of the optical pulse.

$$\mathcal{F}\{\Gamma^{(2)}(\tau)\} = |\tilde{E}(\nu)|^2. \tag{1.40}$$

This linear measurement technique only gives information on spectrum and is not capable of determining ultrashort pulse intensity or phase profiles.

Intensity autocorrelation

The intensity autocorrelation is the first pulse characterization technique that was developed to measure the temporal duration of the optical pulse but it does not give information about its phase profile. It is based on the interaction of two temporally separated replicas of the optical pulses in a nonlinear crystal in which the generated upconverted optical pulse is recorded by a photodetector as depicted in Figure 1.9.

In this optical setup, an optical pulse is split into two pulse replicas by a beam splitter. One of the replicas is directed into a variable optical path that introduces a delay time respect to the other replica. Then both optical pulses are overlapped and focused into a nonlinear crystal such as Second-Harmonic-Generation (SHG) that generates the upconverted optical pulse. The intensity of the generated optical pulse is recorded as a function of the relative delay time between the two replicas [29].

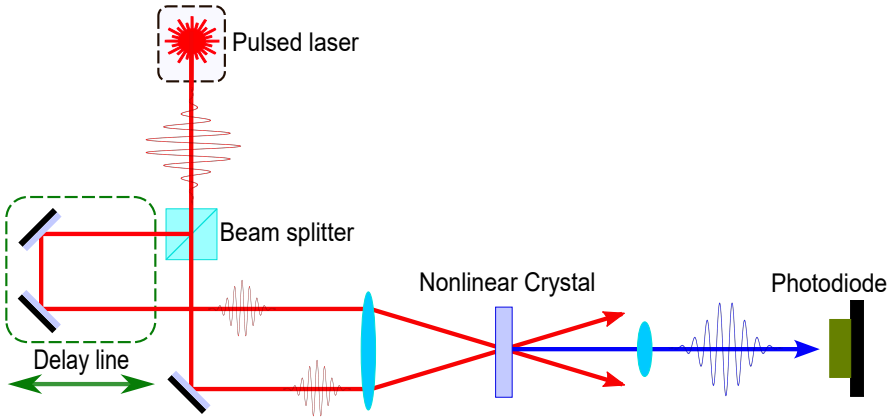

Figure 1.9: Schematic of intensity autocorrelation optical setup.

The nonlinear crystal produces light at twice the frequency of the incident light with the optical field that is given by

$$E_{SHG}(t,\tau) \propto E(t)E(t-\tau), \tag{1.41}$$

therefore, the intensity of the output optical field is given by [25]

$$I_{SHG}(t,\tau) \propto \int_{-\infty}^{+\infty} |E(t)E(t-\tau)|^2 dt. \tag{1.42}$$

The intensity autocorrelation, $I_{SHG}(t,\tau)$, describes how well the optical pulse, $E(t)$, overlaps with the shifted optical pulse, $E(t-\tau)$. This technique is able to measure temporal duration of the pulse and overlapping between the two pulses is an important factor. In the case that the relative delay is increased, consequently the overlapping between the two optical pulses in the nonlinear crystal is reduced that results in a weaker mixing product of the pulses.

Interferometric autocorrelation

The interferometric autocorrelation technique is known as fringe resolved autocorrelation (FRAC) that employs a Michelson interferometer to retrieve the pulse duration from measured autocorrelation. The optical setup is illustrated in Figure 1.10 in which the input optical pulse is split into two replicas and one of replicas is delayed by using a movable mirror. Then both optical pulses are interferred at the beam splitter and focused into a nonlinear crystal (SHG crystal) which generates an upconverted optical pulse. The initial pulse is blocked by a filter and the upconverted pulse is recorded by a photodiode.

The measured interference signal at the photodiode is expressed as

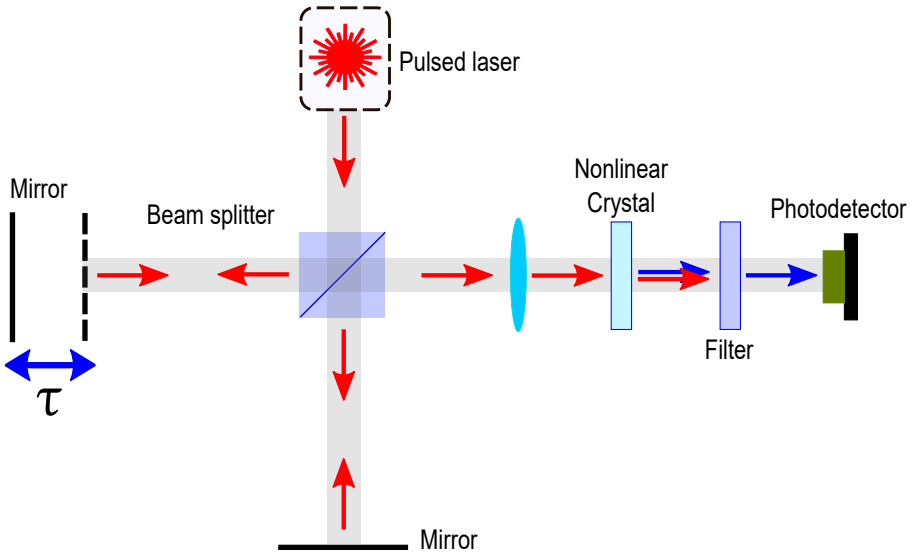

Figure 1.10: Schematic of interferometric autocorrelation optical setup.

$$I_{FRAC}(\tau) = \int_{-\infty}^{+\infty} |[E(t) + E(t-\tau)]^2|^2 dt. \tag{1.43}$$

This relation indicate that the interferometric autocorrelation is a symmetric function similar to other autocorrelation techniques. However, in contrast to the intensity autocorrelation technique, it contains some phase information and it is known as phase-sensitive autocorrelation technique [25]. This is due to interferes of the second harmonic light generated in the nonlinear crystal with light generated by the individual beams, which are then coherently combined. In fact, interference signal results from the coherent addition of the several beams. Finally, the interference fringes are measured as a function of delay time.

The autocorrelation based measurement techniques mainly give information about the temporal duration or intensity of the optical pulse and not its phase profile. This is not sufficient specially for the ultrashort optical pulses, since the phase can significantly change the shape of the optical pulse. In addition, these autocorrelation technique are not applicable to single photons due to existence of nonlinear interaction that can destroy the quantum state of the photon. In the next sections, other technique such as FROG and SPIDER are being reviewed that give information about both phase and intensity profiles.

1.5.2 Frequency resolved optical gating

Frequency-Resolved Optical Gating (FROG) technique is able to characterize the optical pulses by overlapping delayed optical pulse replicas in a second-harmonic generation (SHG) nonlinear crystal. This measurement technique allows for fully characterizing ultrashort optical pulses. Not only optical pulse energy and its temporal duration are measured, but also the full time-dependent electric field including the phase profile can be achieved. The FROG setup is similar to the intensity autocorrelation technique that was presented in subsection 1.5.1, however instead of measuring the autocorrelation of pulse energy as function of delay time, the FROG technique involves measuring the pulse spectrum as a function of delay time. Basically in the FROG measurement setup is similar to the intensity autocorrelator setup as shown in Figure 1.9, except that the photodetector is replaced with a spectrum analyzer. The optical pulses are overlapped in the crystal and through a frequency-doubling process, an up converted pulse is generated. The produced pulse is encoded with the characteristics of the initial optical pulse. In this process, the delayed optical pulse gradually overlaps the stationary optical pulse over a delay time range, and the resulting SHG optical pulse then spectrally resolved [33]. The SHG optical pulse is defined as

$$E_{SHG}(t,\tau) = E(t)E(t-\tau). \tag{1.44}$$

The SHG signal is focused onto the entrance slit of an imaging spectrometer. The spectrometer disperses the light in a direction perpendicular to the slit, resulting in a two-dimensional image with delay time and frequency as axes. The linear detector (a CCD array) detects the intensity (the FROG trace) as [[34]]

$$I_{FROG}(\omega,\tau) = |\int_{-\infty}^{+\infty} E_{SHG}(t,\tau)\exp[i\omega t]dt|^2. \tag{1.45}$$

The FROG trace is a positive real-valued function of the frequency and the time delay between the two pulses. This experimentally recorded FROG trace is then used as an input to a numerical algorithm, which determines the full complex electric field [35]. By analyzing the measured FROG trace, information about the phase and temporal duration of the initial optical pulse is achieved. However, this technique requires an optical spectrum analyzer that is a limiting factor as it is not available in some wavelengths. Furthermore, existence of nonlinear interaction in the optical setup is another obstacle to employ it in quantum regime.

1.5.3 SPIDER

SPIDER stands for Spectral Phase Interferometry for Direct Electric field Reconstruction that is a self-referencing interferometric technique in which measurement process is performed in the frequency domain. The SPIDER is a version of spectral shearing interferometry (SSI) that employs nonlinear interaction to generate the required spectral shift. In the SSI technique two ultrashort optical pulses are spectrally shifted with respect to each other and then are recombined to generate an interference signal in a spectrometer [36].

In the SPIDER scheme, a direct (noniterative) inversion routine is performed to retrieve the spectral phase from the recorded spectral interferogram. This process only requires two one-dimensional Fourier transforms. In other words, the SPIDER technique, not only independently measures the pulse spectrum but also after taking the Fourier transform, it obtains the time-dependent phase and intensity profiles.

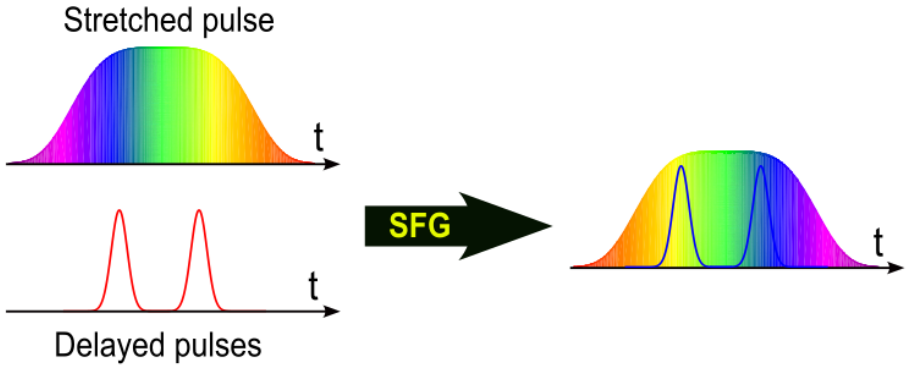

Figure 1.11: Conceptual schematic of the SPIDER.

To implement the SPIDER optical setup, an optical pulse to be characterized is sent into two paths. In first path, the pulse is sent into a passively stabilized Michelson interferometer to generate a pair of replicas in which the optical pulses are separated in time by a fixed delay time that are mixed with a stretched optical pulse in a nonlinear medium. The stretched optical pulse is prepared in the second path that is a portion of the initial test pulse. These pulses are upconverted in the nonlinear crystal. Note that the stretched pulse must be highly chirped such that each wavelength occurs at a different time. As the optical pulses, in the first path, are delayed with respect to each other by a fixed delay time, each of the optical pulses is mixed with a different temporal, and hence spectral, slice of the stretched pulse. This results a pair of replicas of the pulse to be characterized that have been spectrally shifted. The upconverted pulse pair is passed to a spectrometer, and then the spectral interferogram is recorded with a slow detector. Finally the Fourier transform is applied to the recorded spectral interferogram [37]. Note that the SPIDER is typically

done by using the SFG process but it can also be implemented using electro-optic approach to achieve spectral shear [38]. In this way, it is applicable to characterize single photon pulses [39].

In despite that the SPIDER is able to fully characterize the ultrashort optical pulses but it requires a complicated optical setup to make nonlinear interaction and also it relies on using an optical spectrum analyzer that is not available in some wavelength ranges.

1.6 Pulse stretching techniques

Optical pulse stretching is a process in which the duration of an optical pulse is lengthened, or stretched, in time. This can be introduced into an optical system through various techniques, such as the use of dispersive media or designing the optical system and structures.

Optical pulse stretching is often used in applications such as pulse compression, spectral broadening, and ultrafast spectroscopy. For instance, one interesting application is to use it in the Chirped-pulse Amplification technique where the optical pulse is temporally stretched before passing through the amplifier medium that reduces the peak power of the pulse and consequently avoids damage of the amplifier medium [40].

1.6.1 Pulse stretching by dispersive medium

Optical pulse stretching can be achieved through the use of dispersion, which is the variation of the speed of light with frequency. When an optical pulse propagates through a dispersive medium, the different frequency components of the pulse experience different amounts of delay due to their different speeds of propagation which results in pulse spreading in time.

The dispersive pulse stretcher consists of dispersive medium that introduces wavelength dependent optical delays leading to frequency chirp for temporal stretching of ultrashort optical pulses. The term frequency chirp refers to temporal arrangement of the frequency components of the optical pulse. In a medium with positive dispersion, the higher frequency components of the optical pulse travel slower than the lower frequency components that results positively-chirped or up-chirped, increasing in frequency with time. In a medium with negative dispersion, the higher frequency components travel faster than the lower frequency components that results negatively-chirped or down-chirped, decreasing in frequency with time [41, 42].

A dispersive pulse stretcher using an optical fiber is shown in Figure 1.12. In this configuration, the long-wavelength (red) components of the pulse propagate faster

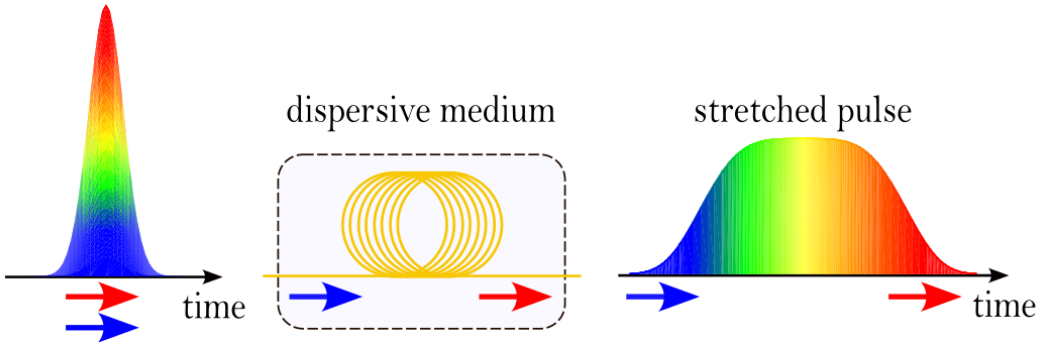

Figure 1.12: Dispersive optical pulse stretcher.

than its Short wavelength (blue) components and the pulse is temporally stretched.

1.6.2 Pulse stretching by diffractive gratings

Another technique to stretch an optical pulse in time is based on using dispersive elements such as prisms or diffraction gratings. These elements can be placed in the optical path of the optical pulse and the amount of dispersion introduced by the element can be controlled by adjusting its properties, such as its thickness and spacing between elements. Using diffraction gratings can provide large stretching factors [43, 44]. And such s dispersive pulse stretcher can be made based on using parallel configuration of a pair of gratings as shown in Figure 1.13.

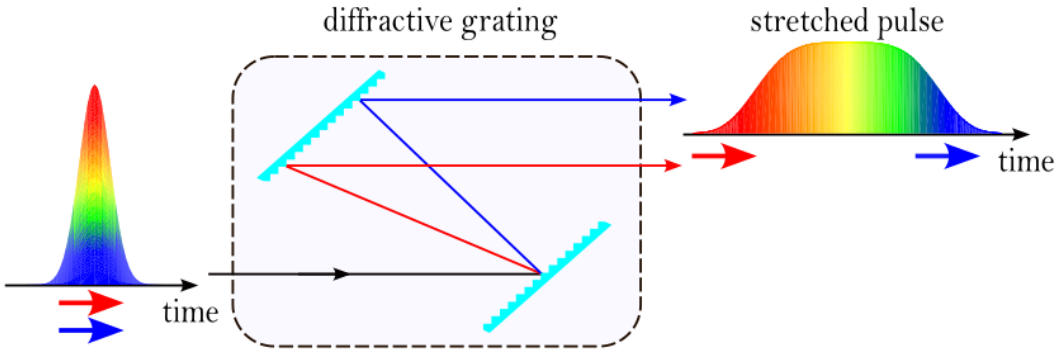

Figure 1.13: Diffraction gratings for stretching optical pulse.

The incident optical pulse is directed on the first grating where it is separated into its component wavelengths. The optical beam is spatially spread and different wavelengths propagate along different directions in the space between the two gratings. After diffraction by the second grating, the beam traces of different wavelengths become parallel while each wavelength component has traveled different optical path

length that results dispersion. As it can be seen in the figure, the longer wavelengths (red) have traveled longer distance in comparison to shorter wavelengths (blue). Thus the pulses of shorter wavelengths arrive earlier than longer wavelengths pulses in such a configuration of parallel gratings.

1.6.3 Pulse stretching by chirped fiber Bragg grating

Introducing dispersion can be implemented by designing grating structures. One popular approach is to fabricate an optical device for pulse stretching and also compression based on fiber Bragg gratings (FBG) structures. By engineering and placing Bragg grating structures inside a piece of optical fiber, a desired dispersion profile can be achieved. A chirped FBG that is an optical fiber in which there is non-uniform modulation of refractive index along the core of the fiber length [45, 46]. The modulation of the refractive index causes an chirped FBG to act as a mirror that reflects certain wavelengths and transmits others as illustrated in Figure 1.14.

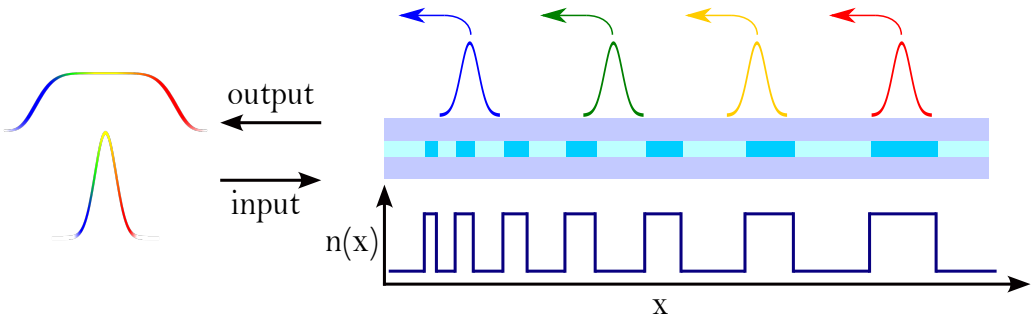

Figure 1.14: Schematic of chirped fiber Bragg grating as pulse stretcher.

In a uniform FBG structure, the Bragg wavelength is is defined as

$$\lambda_B = 2\Lambda n_{eff} \tag{1.46}$$

where Λ is the period of the refractive index modulation, and n_{eff} is the effective refractive index of the optical fiber. In a chirped FBG structure, periodicity of the refractive index modulation is not constant, and it changes along the propagation axis of the optical fiber. In this case, a refractive index function, $\Lambda(x)$, defines the chirp pattern along the propagation direction x. This implies that each different section of the grating along the fiber core, reflects a different Bragg wavelength.

Dispersion engineering based on chirped FBG structures is considered as an efficient approach to apply large dispersion and due to its compatibility with optical fiber platforms, it is highly applicable in the optical communication systems. In the

Chapter 4 of the current thesis, a comprehensive investigation is dedicated on design and fabrication of chirped FBG structures.

1.7 Dispersion effect in optical fibers

Considering an optical pulse propagating through an optical fiber, the optical pulse may experience some impairments as they are referred as different types of dispersion. These types of dispersion are consist of 1) material dispersion, 2) modal dispersion, 3) polarization mode dispersion, 4) waveguide dispersion, and 5) chromatic dispersion (GVD). As most of optical setups presented in the current thesis are implemented in fiber optic platform, here, a brief review on different dispersion effects in the optical fibers is presented.

1.7.1 Material dispersion

Fundamental dispersion effect for a given optical pulse propagating in the optical fiber originates from intrinsic material properties of the optical fiber in which different wavelength components of the optical pulse travel at different velocities through the fiber material. This is derived from the refractive index dependency of the optical fiber on the wavelength. In consequent, considering the optical pulse that contains specific spectral bandwidth, different wavelength components that enter the fiber at the same time will exit the fiber at different times.

1.7.2 Modal dispersion

Optical fibers are divided onto two major types based on their core diameter, single-mode fibers and multi-mode fibers. Single-mode fibers have small core diameter and only supports a single propagation pathway through the core, whereas multi-mode fibers have large core diameter and allows for several propagation pathways in the core. In this regard, the modal dispersion occurs in multi-mode fibers where different modes travel different optical path length. In this case, the modes that travel a longer path length arrive later at the end of the fiber than the modes that travel a shorter path length as shown in Figure 1.15. When a large number of modes (multi-mode fiber) propagate in the optical fiber this results in spreading or broadening the propagating optical pulse along the fiber. On the other hand, in a single-mode fiber, the optical pulse that propagates along the fiber core does not experience the spreading or broadening effect. This type of dispersion is referred as modal dispersion.

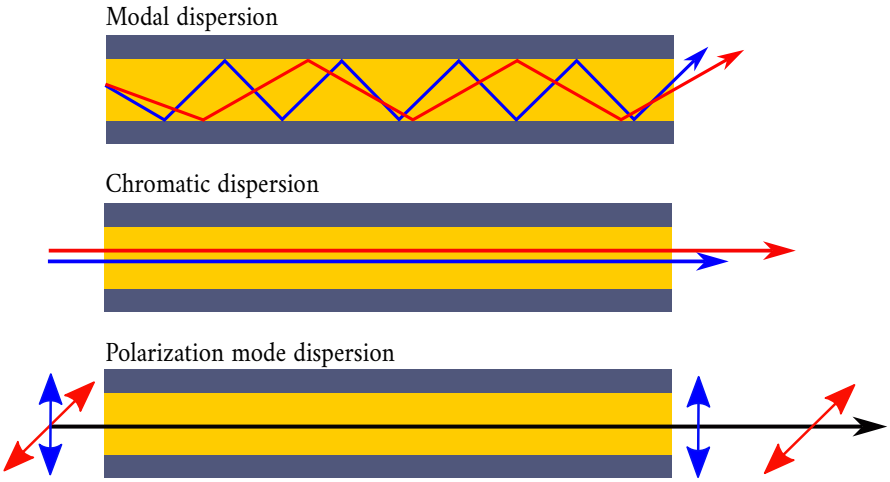

Figure 1.15: Dispersion types.

1.7.3 Polarization mode dispersion

Considering an electromagnetic field propagating along an optical fiber, Z axis, the speed of propagation of the light depends on the refraction index of the medium in the direction of polarization components of the electromagnetic field. In this case, for a given refractive index difference between the x and y directions, the light propagating along the Z axis decomposes into a pair of the lightwaves with X- and Y-directed electric fields. The two lightwaves propagate at slightly different speeds, resulting in differential delay time in propagation of the polarization components of the electromagnetic field [47]. A transmission medium that produces such a retardation in propagation of orthogonal polarization components is said to be birefringent material. This effect is the origin of the polarization mode dispersion (PMD). The PMD in single-mode optical fiber comes from non-circular shape of the core. Such a birefringence effect in optical fiber splits the input optical field into linear slow and fast polarization modes as illustrated in Figure Figure 1.15.

1.7.4 Waveguide Dispersion

The waveguide dispersion is originated from spatial distribution of a propagating optical mode inside the core and cladding regions of an optical fiber. When the optical pulse is coupled inside the optical fiber, its power partly confined in the core and partly in the cladding. In this case, the effective refractive index of the propagating mode lies between the refractive indices of the both core and cladding areas. So that the effective refractive index is determined based on the proportion of power that is confined in the core and cladding regions. In addition, the power distribution of the

mode between the core and cladding is itself a function of the wavelength. So that the longer wavelengths have more power distribution in the cladding area as shown in Figure 1.16.

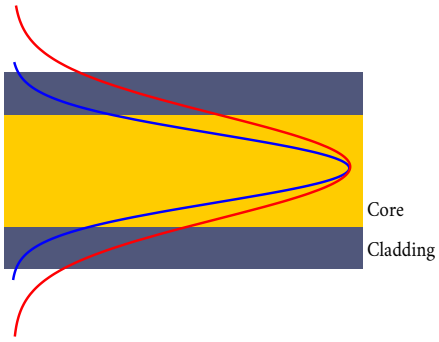

Figure 1.16: Waveguide Dispersion.

All these contribute waveguide dispersion as the mode's propagation constant is determined by the refractive indices of the core and cladding regions, operational wavelength and diameter of the core. The waveguide dispersion is most significant in case of single-mode optical fiber.

1.8 Group Velocity Dispersion

The group velocity dispersion (GVD) resulting from material dispersion and waveguide dispersion that have been discussed in the previous section. As the dispersion effects will be studied in the next chapters of the current thesis, here, a mathematical description of the GVD is presented.

Consider an optical pulse travelling in a single-mode fiber of length L. For a given spectral component at the angular frequency w, the travel time is calculated as $T = L/v_g$, where v_g is the group velocity that is defined as [48]

$$v_g = (d\beta/d\omega)^{-1} \tag{1.47}$$

By using $\beta = \overline{n}k_0 = \overline{n}w/c$, the group velocity is calculated as $v_g = c/\overline{n}_g$, where $\overline{n}_g$ is the group index that is defined as

$$\overline{n}_g = \overline{n} + \omega(d\overline{n}/d\omega) \tag{1.48}$$

This relation shows the frequency dependence of the group velocity that leads to pulse broadening in temporal domain. This is due to the fact that different spectral components of the optical pulse experience dispersion effects during propagation. For

a given input optical pulse with spectral bandwidth of $\Delta\omega$, that propagates through the optical fiber with length of L, while the spectral bandwidth does not change, the temporal width at the output of the fiber is expressed as following [48]

$$\Delta T = \frac{dT}{d\omega}\Delta\omega = \frac{d}{d\omega}(\frac{L}{v_g})\Delta\omega = L\frac{d^2\beta}{d\omega^2}\Delta w = L\beta_2\Delta\omega \tag{1.49}$$

The parameter $\beta^2 = d^2\beta/d\omega^2$ is known as GVD parameter. It determines how much an optical pulse would broaden on propagation inside the fiber.

In experimental optics, it is more convenient to express a frequency bandwidth, $\Delta\omega$, by a range of wavelengths, $\Delta\lambda$. So we can recalculate the relations by using $\omega = 2\pi c/\lambda$ and $\Delta\omega = (-2\pi c/\lambda^2)\Delta\lambda$, so Equation 1.49 can be written as

$$\Delta T = \frac{d}{d\lambda}(\frac{L}{v_g})\Delta\lambda = DL\Delta\lambda, \tag{1.50}$$

where

$$D = \frac{d}{d\lambda}(\frac{1}{v_g}) = -\frac{2\pi c}{\lambda^2}\beta_2 \tag{1.51}$$

D is called the dispersion parameter and is expressed in units of ps/(km-nm).

1.9 Photon-pair source based on spontaneous parametric down-conversion

For spectral and temporal shaping of quantum light pulses, one needs to generate single photons. The ideal case of single photon source should emit single indistinguishable photons with decreased multi-photon emission. One versatile method to get single-photon source that exhibit quantum mechanical characteristics is based on spontaneous parametric down-conversion (SPDC).

1.9.1 Spontaneous Parametric Down Conversion

Here simulation calculations of photon pair generation using the SPDC process in the periodically polled Potassium Titanyl Phosphate (PPKTP) crystal is presented [49]. In this nonlinear process, one high-energy photon, pump photon, is converted into a pair of lower-energy photons, signal and idler photons. In this interaction, a nonlinear parametric processes and phase matching condition should be satisfied in order to generate pair photons. The output profile of the generated photons can be engineered by modifying the phase matching bandwidth of the nonlinear crystal and the input pump bandwidth.

Through this parametric process the energy conservation should be satisfied as

$$\hbar_p\omega = \hbar_s\omega + \hbar_i\omega. \tag{1.52}$$

Besides this, the momentum conservation is required to be satisfied. In order to achieve the phase matching condition, the wave vectors of these three interacting photons should be matched. The phase matching can be achieved using birefringent nonlinear materials, where refractive index changes with polarization. This leads to different types of SPDC based on the polarizations of the input photon (pump) and the two output photons (signal and idler). The conventional way to convey the phase matching condition for three photons is through the definition as

$$\Delta k = k_p - k_s - k_i = 0. \tag{1.53}$$

Here type-II of the SPDC is considered so that the signal and idler photons have perpendicular polarization state with respect to each other. By considering an ordinary and extraordinary refractive indices for the nonlinear crystal, the type-II phase matching is described as: $o \rightarrow o + e$ or $e \rightarrow e + o$.

In order to acquire the phase matching condition, the Sellmeier equation is employed to obtain the ordinary and extraordinary refractive index of the KTP crystal. The Sellmerier equations for the KTP is given as [50]

$${n_y}^2 = 3.45018 + \frac{0.04341}{\lambda^2 - 0.04597} + \frac{16.98825}{\lambda^2 - 39.43799}, \tag{1.54}$$

$${n_z}^2 = 4.59423 + \frac{0.06206}{\lambda^2 - 0.04763} + \frac{110.80672}{\lambda^2 - 86.12171}. \tag{1.55}$$

By considering the refractive indices of the birefringent crystal (ordinary refractive index for both pump and signal photons and extraordinary refractive index for the idler photon), the periodicity at phase matching condition ($\Delta k = 0$) can be calculated as

$$\Lambda = \frac{2\pi}{\Delta k} = \frac{1}{(\frac{n_p}{\lambda_p}) - (\frac{n_s}{\lambda_s}) - (\frac{n_i}{\lambda_i})}. \tag{1.56}$$

For the calculations, the pump wavelength at 780 nm was considered that generates signal and idler photons at 1560 nm.

The spectral properties of the SPDC source is governed by the joint spectral amplitude $E(f_s, f_i)$ for signal and idler frequencies f_s and f_i, which is given by the product of the pump amplitude function $\alpha(f_s, f_i)$ and the phase-matching amplitude function $\phi(f_s, f_i)$ of the nonlinear crystal as

$$E(f_s, f_i) = \alpha(f_s + f_i)\phi(f_s, f_i). \tag{1.57}$$

The pump amplitude function with Gaussian profile is given by [51]

$$\alpha(f_s, f_i) \approx \exp\left(-\frac{(f_s - f_{s0} + f_i - f_{i0})^2}{4\sigma_p^2}\right), \tag{1.58}$$

note that the FWHM of the amplitude function, Δf_{amp}, should be considered in Equation 1.58.

$$\Delta f_{\text{amp}} = \sqrt{2}\,\Delta f_{\text{int}}, \tag{1.59}$$

where Δf_{int} is the intensity FWHM of the pump function. The pump frequency bandwidth is given by

$$\Delta f_{\text{amp}} = \frac{\Delta\lambda_{\text{amp}}\, c}{\lambda_{p0}^2}, \tag{1.60}$$

where c is the speed of light. So σ_p can be calculated as

$$\sigma_p = 2.3548\,\Delta f_{\text{amp}}. \tag{1.61}$$

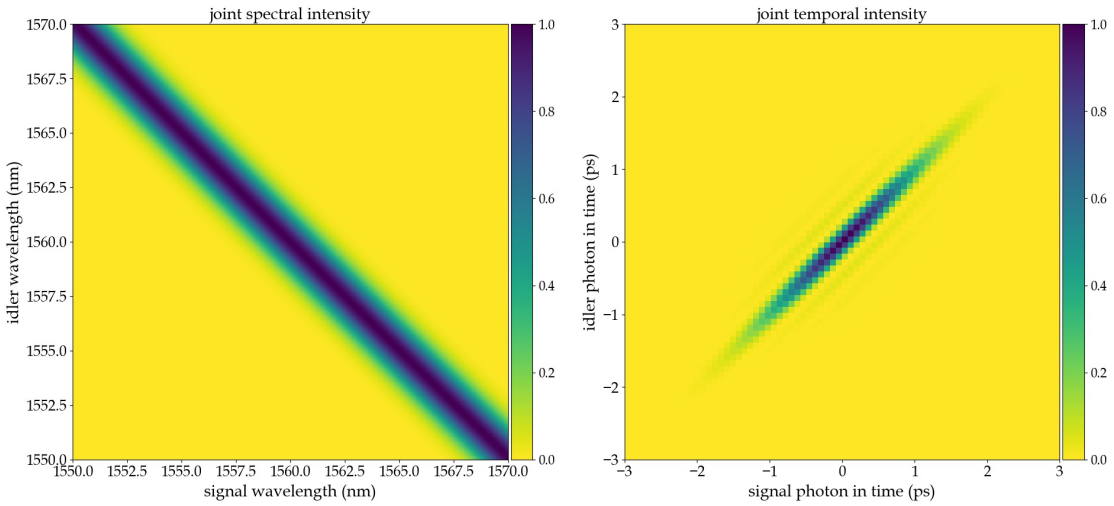

Figure 1.17: Joint intensity profiles of the pump function in spectral and temporal domains.

I did simulation calculations to illustrate the bi-photon spectral and temporal representations of the SPDC process. The joint spectral intensity (JSI) of the pump function $\mid \alpha(f_s, f_i) \mid^2$ and its Fourier transformation, joint temporal intensity (JTI), are shown in Figure 1.17.

Now, characteristics of the phase matching function is considered. The phase matching depends on the optical properties of the employed nonlinear crystal. The

length of the nonlinear crystal, L, determines the phase matching bandwidth. In the photon-pair source in this thesis, a nonlinear crystal with 10 mm-long PPKTP crystal with a polling period of 46.165 μm was used.

Considering the phase matching function as [26]

$$\phi(w_s, w_i) \approx \frac{\sin(\Delta k(w_s, w_i)L/2)}{\Delta k(w_s, w_i)L/2}, \tag{1.62}$$

the JSI of the phase matching function is illustrated in Figure 1.18. One can obtain the JTI of the phase matching function by taking Fourier transform of the JSI profile as shown in Figure 1.18.

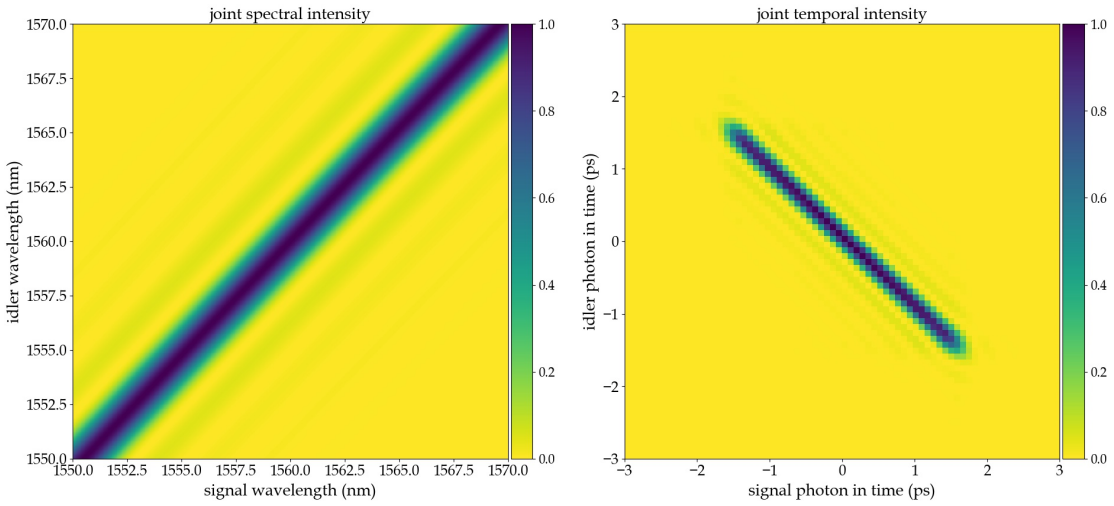

Figure 1.18: Joint intensity profiles of the phase matching function in spectral and temporal domains

To simulate the JSI and JTI profiles of the SPDC source, we should consider the multiplication of the pump amplitude function and the phase matching amplitude function. The module square of this multiplication give the JSI as it is shown in Figure 1.19.

To engineer the spectral and temporal characteristics of the JSI profile, one need to change the parameters of either pump function or phase-matching function. Since the spectral bandwidth of the phase-matching function is defined by the crystal length which is is constant, we only can modify the pump bandwidth in order to obtain our desired spectral features in the bi-photon spectrum. If one take the pump bandwidth as same as the phase-matching bandwidth, this results in uncorrelated spectrum (circular shape) of the JSI as shown in Figure 1.19. This case gives pure single photon

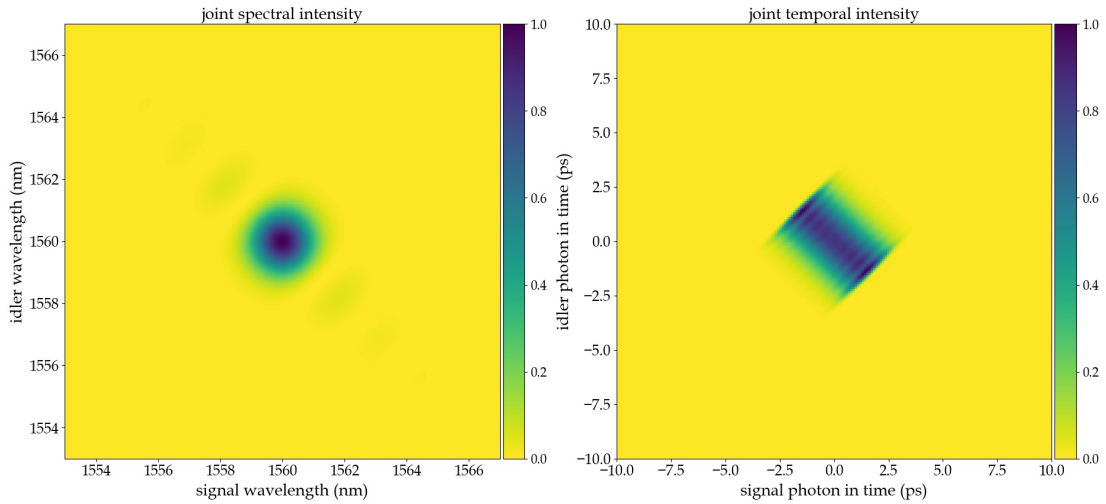

Figure 1.19: Joint intensity profiles of the SPDC source in spectral and temporal domains

generation in which there is no correlation between signal and idler photons and they can be separated. By taking a wider pump bandwidth than the phase-matching bandwidth, the JSI of the SPDC leads to positively correlated photons while taking a narrower pump bandwidth results in negatively correlated photons.

For the experiment presented in this thesis, I adjusted the pump bandwidth of the source in a way to get an uncorrelated photons and used it in the experiment on measuring temporal duration of single photon pulse that will be presented in the chapter 3. The SPDC photon-pair source used in this thesis was built by Michał Mikołajczyk.

Chapter 2

Direct characterization of temporal phase modulation by temporal interferometry

2.1 Introduction to spectral and temporal manipulation of optical pulses

In optical communication systems, manipulating spectral phase and temporal phase features of optical pulse is a common technique to shape the optical pulse in time and frequency domains. However such modifications can be a challenging task depending on spectral and temporal bandwidths of the optical pulse. Modifying the spectral phase of an optical pulse with a broad bandwidth is relatively easy, while modifying its temporal phase is more difficult due to the Fourier relationship between the spectral and temporal domains. On the other hand, modifying the temporal phase of an optical pulse with a narrow bandwidth and hence long temporal duration is relatively easy, but modifying its spectral phase is more challenging. There is a small window, on the order of 10 picoseconds in temporal duration, in which both the spectral and temporal phases can be accessible simultaneously.

2.2 Spectral phase and temporal phase

Temporal phase

Considering the pulse electric field as a complex function and neglecting its spatial dependence, it can be represented by its intensity and phase components as

$$E(t) = \sqrt{I(t)} \exp\left[i(\omega_0 t - \phi(t))\right] + c.c., \tag{2.1}$$

where $I(t)$ is the temporal intensity, ω_0 is the carrier angular frequency and $\phi(t)$ is the

temporal phase. Temporal phase manipulation involves modifying the phase of the optical pulse at different points in time. This can be accomplished using a variety of techniques, such as using electro-optic modulators to apply a phase shift to the pulse [38], or using nonlinear effects like four-wave mixing, self-phase modulation and cross-phase modulation that are based on modulating the phase of the optical pulse over time by exploiting the nonlinear optical properties of the medium through which the optical pulse is traveling. In this context, when the optical pulse is transmitted through the medium, the Kerr effect causes a time-dependent phase shift according to the time-dependent pulse intensity. In this way, the initial unchirped optical pulse acquires a chirp [52].

In self-phase modulation, the intensity of the light wave causes the refractive index of the medium to vary, which in turn modulates the phase of the light wave. The phase modulation is proportional to the intensity of the light wave, so by modulating the intensity of the light wave, it is possible to modulate the phase of the light wave. The self-phase modulation technique can approximate the required effect but is ineffective for single-photon signals [29]. In cross-phase modulation technique, a nonlinear optical effect occurs when two waves with different frequencies interact in a medium, resulting in a change in the phase of one of the waves. The phase of the wave that is being modulated can be controlled by the intensity of the other wave. In temporal phase modulation using four-wave mixing, two input light waves with different frequencies are passed through a nonlinear medium. The nonlinearity of the medium causes the two input waves to interact and generate a third wave at a different frequency. By modulating the phase of one of the input waves, it is possible to modulate the phase of the third wave. These methods for controlling the temporal phase of an optical pulse have primarily relied on nonlinear effects that are not applicable in quantum regime. In contrast, the approach presented in this thesis involves propagating the pulse through a material with a electro-optic response and applying a controlled electric field to manipulate the phase of the pulse. This allows for an alternative way to control the phase of the optical pulse.

Spectral phase

The time-domain pulse electric field, $E(t)$, is connected to frequency-domain electric field through Fourier transform. Considering the pulse electric field in the spectral domain as complex function, the frequency-domain equivalent of the temporal intensity and temporal phase are the spectral intensity and spectral phase, respectively. The frequency-domain electric field is represented as

$$\tilde{E}(\omega) = \sqrt{S(\omega - \omega_0)}\exp\left[-i(\varphi(\omega - \omega_0))\right] + c.c., \tag{2.2}$$

where $S(\omega)$ is the spectral intensity and $\varphi(\omega)$ is the spectral phase. Considering an optical pulse, the spectral phase describes its the temporal evolution, and it can

be manipulated through various techniques using dispersive medium, diffraction gratings and nonlinear interactions [53, 54]. In this context, the dispersion refers to the dependence of the refractive index of a medium on the frequency or wavelength of light. When the optical pulse passes through a material with a high dispersion, the spectral phase of the optical pulse will be modified, leading to a change in the temporal profile of the optical pulse. The later approach to manipulate the spectral phase is based on nonlinear interactions in materials. These interactions can lead to the generation of new frequencies or the modification of the spectral phase of the incident light. Both dispersion and nonlinear interactions can be used to manipulate the spectral phase of a light wave in a controlled manner, and these techniques are important in many applications, including optical pulse shaping in both classical and quantum optics.

2.3 Temporal phase modulation using electro-optic phase modulator

Temporal phase modulation is a technique that involves modulating the phase of a light wave over time. This can be achieved using an electro-optic phase modulator, which is a device that uses an electric field to alter the refractive index of a material and thereby change the phase of light passing through it. In a temporal phase modulation system, an input light wave is passed through an electro-optic phase modulator, which is driven by a control signal. The control signal modulates the electric field applied to the modulator, which in turn modulates the phase of the light wave.

2.3.1 The electro-optic phase modulator

Electro-optic crystals change their optical properties under exposure of an electric field due to forces that alter the arrangement, orientation, or shape of their constituent molecules. This phenomenon, known as the electro-optic effect, results in a change in the refractive index caused by an electric field applied to an electro-optic crystal with anisotropic properties. It can modify the refractive index and therefore affect the light passing through it. When there is a linear dependency between refractive index change and the applied electric field, it is known as Pockels effect or linear electro-optic effect while the quadratic electro-optic effect is called the Kerr effect. In the electro-optic phase modulators (EOPM), the Pockels effect is employed and one common material used in the EOPMs is lithium niobate ($LiNbO_3$), a crystalline substance that exhibits the electro-optic effect. Lithium niobate has a relatively high electro-optic coefficient, making it an attractive material for use in phase modulators

[55]. It is also highly transparent and has a low absorption coefficient, which makes it well-suited for use in telecommunications applications where high transmission efficiency is required.

In this study, we used a modulator with a channel waveguide fabricated from lithium niobate material. Lithium niobate is an electro-optic material that exhibits the transverse Pockels effect in which the effective index changes proportionally to the applied electric field. The refractive index change under exposure of external electric field E_{ext} is expressed as [26]

$$\Delta n_o = -\frac{1}{2} n_o^3 r_{13} E_{ext}, \tag{2.3}$$

$$\Delta n_e = -\frac{1}{2} n_e^3 r_{33} E_{ext}, \tag{2.4}$$

where n_o and n_e are ordinary and extraordinary indexes along optical axes of the crystal. The electro-optic coefficients r_{13} and r_{33} are appropriate element of third-rank electro-optic tensor of ($LiNbO_3$). In the EOPM fabricated with lithium niobate crystal, r_{33} coefficient is much higher than r_{13}, hence the polarization of the input optical pulse is aligned along the crystal axis with extraordinary index to get maximum refractive index change. The introduced phase shift experienced by an incident wave packet due to the modulation of the refractive index over crystal length L is given by

$$\phi = nk_0 L = \frac{2\pi}{\lambda_0} nL, \tag{2.5}$$

where λ_0 is the free space wavelength. By substituting equation Equation 2.4, phase shift introduced by the modulator is given by [24]

$$\phi = \phi_0 - \pi \frac{n_e^3 r_{33} E_{ext} L}{\lambda_0}, \tag{2.6}$$

where $\phi_0 = 2\pi nL/\lambda_0$. By considering the applied electric field as $E_{ext} = V/d$, in which d is channel waveguide width and V is the applied voltage to the nonlinear crystal, the introduced phase shift is expressed as

$$\phi = \phi_0 - \pi \frac{V}{V_\pi}, \tag{2.7}$$

where

$$V_\pi = \frac{d}{L} \frac{\lambda_0}{r_{33} n_e^3}. \tag{2.8}$$

The parameter V_π, known as the half-wave voltage, is the applied voltage at which the phase changes by π. So the half-wave voltage is dependent on physical parameters of the nonlinear crystal, therefore it is specific to each individually manufactured

modulator. Note that, due to birefringence of the crystal, it is important to send light with proper polarization state. The modulator employed in the present study was fabricated in a way that one of the polarization states experiences much higher modulation than the other polarization state.

2.3.2 Electro-optic phase modulation of optical pulses

For spectral and temporal shaping of light pulses, in this thesis, the electro-optic approach is being to employed as a coherent operation that is applicable in both classical and quantum signals. In this approach, optical pulses are modulated using the Electro-optic phase modulator (EOPM) as its main features was defined in the previous section. There are several factors that can influence the amount of introduced phase shift through the electro-optic phase modulation process, such as the strength of the applied electric field, the strength of the electro-optic coefficient and the total interaction length inside the phase modulator.

In general, an optical wave propagating through an electro-optic nonlinear crystal under exposure to a time-varying applied voltage, $V(t) = V_m \cos(\omega_m t)$, and along the z direction of the nonlinear crystal, acquires a total phase shift given by [56]

$$\phi(z,t) = \omega_0 t - k_0 z - \frac{\omega_0}{c}\int_0^z dz' \Delta n(z',t) = \omega_0 t - k_0 z - \Gamma(z,t) \tag{2.9}$$

where ω_0 is carrier angular frequency, k_0 is propagation constant, $\Delta n(z,t)$ is the index modulation and $\Gamma(z,t)$ is the phase retardation due to the electro-optic interaction with the modulating voltage signal. The index modulation along the crystal is expressed as

$$\Delta n(z,t) = \Delta n_0 \cos(kz - \omega_m t + \phi_0) \tag{2.10}$$

where Δn_0 is the peak instantaneous refraction index modulation under time-varying voltage, k is the propagation constant of driving field, ω_m is the angular frequency of the modulating signal, and ϕ_0 is the initial phase offset.

In practice, by considering the half-wave voltage of the phase modulator, based on its manufactured specification, a temporally varying applied voltage signal to the phase modulator, $V = V(t)$, results a time-dependent phase shift to the light pulse as

$$\phi_{EOPM}(t) = \frac{\pi}{V_\pi} V(t). \tag{2.11}$$

In this thesis, a pulsed light source is sent into the phase modulator in which temporal duration of the light pulse is shorter than the oscillation period of the RF modulating signal as illustrated in Figure 2.1. By adjusting the temporal alignment of the RF modulating signal and the short light pulse, by setting the initial phase offset,

it is possible to select the desired region of time-varying RF modulating signal to induce a time-varying phase. By synchronizing a different part of the RF modulation signal to the light pulse, a different effect at the output of the phase modulator is observed. In the next section, the effect of modulating with linear and quadratic regions of the time-varying voltage signal is studied.

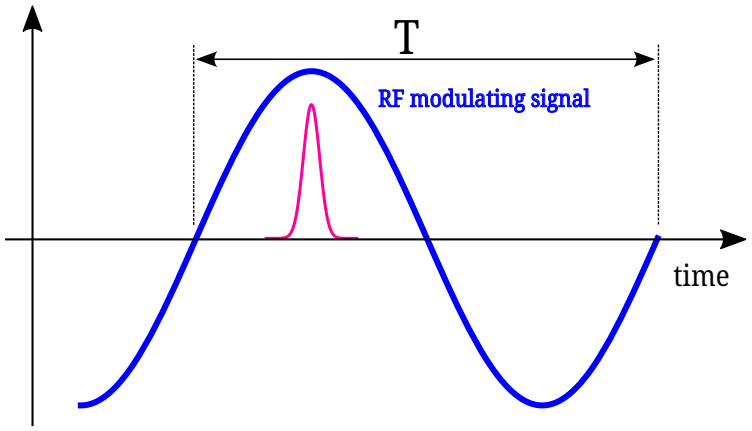

Figure 2.1: Illustration of RF modulating signal and the optical pulse passing through the phase modulator in time domain

2.4 Optical pulse shaping by temporal phase modulation

In this section, a unified formalism to describe relationship between light pulses at the input and the output of the phase modulator is presented. The action of any linear operation on the input complex envelope of a short light pulse, $\psi_{\text{in}}(t')$, can be characterized as a linear superposition [21]:

$$\psi_{\text{out}}(t) = \int dt' \psi_{\text{in}}(t') K(t, t'), \tag{2.12}$$

where the operation is described by the kernel $K(t, t')$ and $\psi_{\text{out}}(t)$ represents the output complex envelope. This formalism in time domain can be connected to its pair in the frequency domain through Fourier transform relation. Since any linear operation in time is also linear in frequency, so the spectral representation of the formalism is expressed as

$$\tilde{\psi}_{\text{out}}(\omega) = \int d\omega' \tilde{\psi}_{\text{in}}(\omega') \tilde{K}(\omega, \omega'), \tag{2.13}$$

where the kernel in the frequency domain forms a Fourier transform pair with the kernel in time as follow

$$\tilde{K}(\omega,\omega') = \iint dt'dt''K(t',t'')\exp[i(\omega t' - \omega' t'')]. \tag{2.14}$$

To modify the spectral profile of an input light pulse to the phase modulator, the temporal phase of the light pulse is manipulated through the electro-optic phase modulation process. As promised in the previous section, we study impact of linear and quadratic temporal phase modulation on the spectral profile of the light pulse. This is a linear operation and we use the presented formalism to describe the relation between input and output spectral profiles of the light pulse. Note that this process is also a coherent operation that can be applicable in quantum light pulses.

2.4.1 Linear temporal phase modulation

Consider a short light pulse in its temporal representation, $\psi_{\text{in}}(t)$, that is sent through the phase modulator. This pulse is being modulated by applying a linear temporal phase of the form $\phi(t) = \alpha t$. In practice, this can be done by synchronizing the linear region of the sinusoidal RF voltage signal to the light pulse as shown with vertical dashed lines in Figure 2.2. This process results in a modified light pulse at the output of the modulator as

$$\psi_{\text{out}}(t) = \exp[i\alpha t]\psi_{\text{in}}(t). \tag{2.15}$$

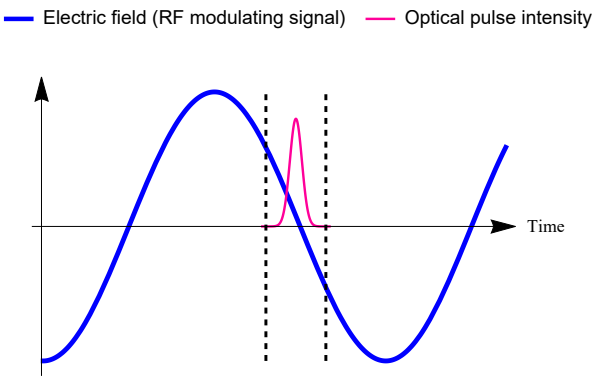

Figure 2.2: Placing light pulse in the linear region of the sinusoidal RF modulating signal

The impact of the linear temporal phase modulation on the light pulse can be seen in its spectral representation by applying Fourier transform as follow

$$\tilde{\psi}_{\text{out}}(\omega) = \int dt \exp[i\omega t]\psi_{\text{out}}(t) = \int dt \exp[i(\omega+\alpha)t]\psi_{\text{in}}(t), \tag{2.16}$$

$$\tilde{\psi}_{\text{out}}(\omega) = \tilde{\psi}_{\text{in}}(\omega + \alpha). \tag{2.17}$$

In result the light pulse after applying the linear temporal phase has experienced a spectral shift by, α, with respect to input light pulse. This is expected from spectral shift property of the Fourier transform. Note that applying a linear temporal phase with negative sign, by synchronizing the negative slope of the sinusoidal RF modulating signal, will result in spectral shift in the opposite direction in the spectral domain [57].

2.4.2 Quadratic temporal phase modulation

Now we consider the case that a short light pulse is being modulated by applying a quadratic temporal phase. In practice, this can be implemented by synchronizing the parabolic region of the sinusoidal RF voltage signal to the light pulse as shown with vertical dashed lines in Figure 2.3. By considering the time-varying sinusoidal applied voltage, $V(t) = V_m \cos(\omega_m t)$, the quadratic temporal phase can be approximated with the second-order term of the Taylor expansion of the sinusoidal signal as

$$\phi(t) = \frac{\pi}{V_\pi} V_m (1 - \frac{\omega_m^2}{2!} t^2 + \frac{\omega_m^4}{4!} t^4 - ...). \tag{2.18}$$

This process results in a modified light pulse at the output of the modulator as

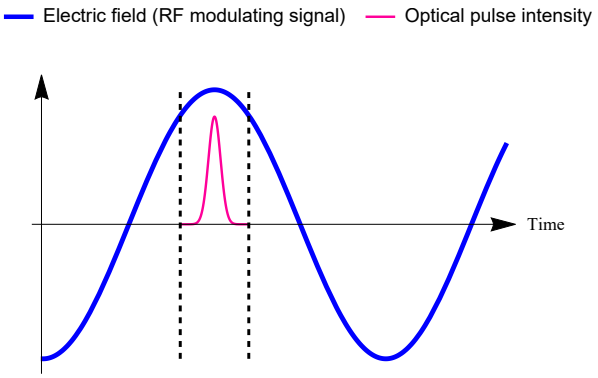

Figure 2.3: Placing light pulse in the parabolic region of the sinusoidal RF modulating signal

$$\psi_{\text{out}}(t) = \exp[-i\frac{\omega_m^2}{2} t^2] \psi_{\text{in}}(t). \tag{2.19}$$

The spectral representation is given by applying Fourier transform as

$$\tilde{\psi}_{\text{out}}(\omega) = \int dt \exp[i\omega t]\psi_{\text{in}}(t) \exp[-i\frac{\omega_m^2}{2}t^2]. \tag{2.20}$$

The result of applying a quadratic temporal phase depends on the profile of the input light pulse. By considering a Gaussian light pulse as

$$\psi_{\text{in}}(t) = A \exp[-\frac{t^2}{2\sigma_t^2}]. \tag{2.21}$$

In this case, in the time domain, the output light pulse is defined as:

$$\psi_{\text{out}}(t) = A \exp[-\frac{t^2}{2\sigma_t^2}] \exp[-i\frac{\omega_m^2}{2}t^2]. \tag{2.22}$$

By considering the following Fourier transform relation, we can calculate the output light pulse in the spectral domain [56, 21]

$$\mathcal{F}\{\exp[-(a+ib)t^2]\} = [\frac{\pi^2}{a^2+b^2}]^{\frac{1}{4}} \exp[-\frac{a-ib}{4(a^2+b^2)}\omega^2], \tag{2.23}$$

the modulated light pulse in the spectral domain can be represented as

$$\tilde{\psi}_{\text{out}}(\omega) = A[\frac{4\pi^2\sigma_t^4}{(1+\omega_m^4\sigma_t^4)}]^{\frac{1}{4}} \exp[-\frac{\sigma_t^2\omega^2}{2(1+\omega_m^4\sigma_t^4)} + i\frac{\omega_m\sigma_t^4\omega^2}{2(1+\omega_m^4\sigma_t^4)}], \tag{2.24}$$

where the spectral bandwidth of the modulated light pulse after undergoing quadratic temporal phase modulation is expressed as $\sigma_m^2 = (1+\omega_m^4\sigma_t^4)/\sigma_t^2$, that indicates the spectral amplitude is broaden by factor of $\sqrt{1+\omega_m^4\sigma_t^4/\sigma_t^2}$.

So far, a standard approach for temporal phase modulation using sinusoidal driving RF signal was considered. In the next section, we are going to modulate the short light pulses using a complex unknown driving signal resulting from electronic response of a photodiode.

2.5 Characterizing electro-optic phase modulation using temporal interferometry

In the previous section, the temporal phase modulation based on sinusoidal waveform was studied. It was shown that by synchronizing the linear or quadratic regions of the RF driving signal with the light pulse inside the phase modulator, the light pulse experiences different effects such as spectral shift or bandwidth compression/expansion. In practice, preparing the sinusoidal signal requires a waveform generator and synchronizing specific region of the electronic modulating signal to the light pulses

needs a phase locked loop. All these electronic devices are source of noise for the temporal phase modulation process. To avoid the noise resulting from the waveform generator, in the current section, an amplified electronic signal from a photodiode is used to modulate the short light pulses passing through the phase modulator. The electronic response from the photodiode depends on the intrinsic physical features of the semiconductor used in the photodiode which means its electronic response changes arbitrary. To determine the electronic signal profile of the photodiode, we measure its response using an oscilloscope and then characterize the temporal phase profile of this unknown signal using temporal interferometery technique that is also known as electro-optic sampling technique.

2.5.1 Measuring electronic response of photodiode

The simplest way to produce a voltage signal is to employ a waveform generator that is an expensive device specially when wide-bandwidth device is required. But here, we use a fast photodiode to prepare voltage signal for temporal phase modulation [58]. A photodiode basically convert optical pulse to electronic signal that can be used for modulating short optical pulses. For this purpose, optical pulses of sub-picosecond duration with repetition rate of 80 MHz pulsed laser, Menlo Systems C-Fiber HP, at central frequency of 1550 nm are directed into fast photodiode (12.5 GHz bandwidth, EOT ET-3500F). The optical pulses are converted to electrical pulses by using the photodiode then amplified to deliver RF voltage signal to the electro-optic phase modulator (EOPM). The produced RF voltage signal is used to modulate the optical pulses passing through the EOPM. The amplified electronic response of the fast photodiode is measured using an oscilloscope as shown in Figure 2.4.

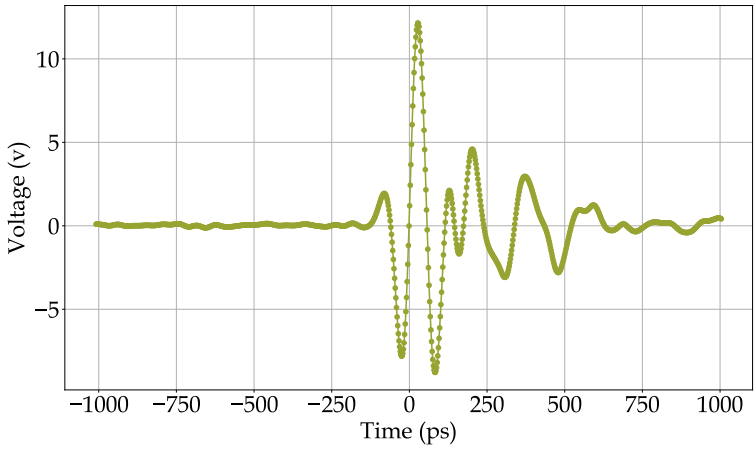

Figure 2.4: Electronic response of the high bandwidth photodiode 12.5 GHz.

As it can be seen from the response of the fast photodiode, it gives unknown voltage

signal that depends on the intrinsic characteristics of the photodiode. However, it has regions with linear and quadratic shapes that can be used for temporal phase modulation of optical pulses after characterization. The modulating signal depicted in the Figure 2.4 applies different temporal phase on the optical pulses because of its voltage changes. In fact, the temporal phase applied by the EOPM has direct relation with temporally varying voltage which is given with this formula

$$\phi(t) = \frac{\pi}{V_\pi} V(t) \tag{2.25}$$

where $V(t)$ is temporally varying voltage signal and V_π is the half-wave voltage which is determined by the modulator's technical specification. The half-wave voltage for used electro-optic modulator is 3V at frequency of 1 GHz, taken from modulator's datasheet. But its value changes in higher frequencies. By fitting Sin function to the parabolic part of the modulating signal, the frequency of $\sim$ 8 GHz was achieved for the modulating signal. By using modulator's datasheet, we can work out its half-wave voltage. Based on the definition for voltage amplification, voltage gain in $dB = 20\log(V_2/V_1)$, therefor X dB drop in the EOPM's response means the half-wave voltage is changed by factor $10^{(X/20)}$. So the half-wave voltage of the EOPM at $\sim$ 8 GHz, is calculated as $V_\pi = 3 * 10^{(2/20)} = 3.77$V.

After measuring the electronic response of the fast photodiode, the next step is to characterize the temporal phase profile resulting from the voltage signal of the fast photodiode. This was done using temporal interferometry technique that will be introduced in the next section.

2.5.2 Polarization based Mach-Zehnder interferometer

In this section, a measurement tool for characterizing complex temporal phase profile resulting from electronic response of the described fast photodiode in the section 2.5.1 is presented. The EOPM is made of birefringent material in which phase modulation is mainly applied to one of the polarization components of the optical pulse passing through the EOPM. We take this as an advantage and make an interferometer based on interfering polarization components of the optical pulse. Such interferometer, polarization based Mach-Zehnder interferometer as illustrated in Figure 2.5, offers a stable and highly sensitive measurement tool and enables to directly measure the temporal phase modulation patterns applied to optical pulses.

For performing precise measurements in ultrafast regime, it is essential to make a stable interferometer. To this purpose, a common path Mach-Zehnder interferometer (MZI) in which the reference beam and sample beam travel along the same path was developed. Generally a common path interferometer is more stable to environmental effects and vibrations than a double path interferometer.

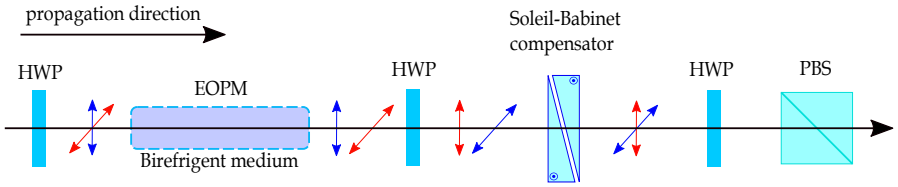

Figure 2.5: Schematic of designing a balanced polarization based Mach-Zehnder interferometer. The red and blue arrows indicate horizontal and vertical polarization components. HWP : half-wave plate, PBS : polarizing beam splitter.

The polarization MZI employs polarization maintaining (PM) fiber in which the polarization state of light pulse will be highly preserved even if the fiber undergoes external effects. The PM fiber is made of birefringent material which has two axes (fast and slow axes). An optical beam containing polarization components (vertical and horizontal) when propagates through PM fiber, each of components experiences a different refractive index that consequently travel with different velocities. In result, polarization components are temporally displaced when beam propagates through the PM fiber (in this case, a combination of the EOPM and PM fiber was used which both are made of birefringent material). Then it is possible to use a half-wave plate and also additional PM fibers with axes rotated by 90 degrees to compensate delay time introduced between polarization components, the amount of delay will be calculated by spectral inteferometry technique in the next subsection 2.5.3, and consequently to make interferometer with same optical path length for both polarization components. A part of delay time was also compensated by using calcite wedges, in the form of Soleil Babinet Compensator, in order to have variable thickness of birefringent crystal which gives capability to control the introduced retardation. Eventually, the polarization MZI was implemented with having zero delay time and high visibility for switching between dark and bright fringes. The configured polarization MZI has high stability and visibility which offers powerful tool to characterize spectral and temporal interference of ultrashort optical pulses.

2.5.3 Measuring retardance of birefringent devices by spectral interferometry

For designing the developed polarization MZI in the subsection 2.5.2, the delay time introduced between polarization states of all birefringent components is required to be calculated. These calculations help to design a balanced interferometer in which optical path length of two arms of the interferometer is almost equal or in the current case, the delay time time between the polarization states after passing through all

birefringent components is almost zero. For this purpose, characterizing the spectral interference of two interfering optical pulses is a standard technique that allows to calculate the delay time between two interfering optical pulses [59].

Here, the introduced delay time of polarization states of a optical pulse passing through the EOPM is measured. To implement the setup, optical pulses are coupled into the EOPM that is inactive in this experiment. Then at the output of the EOPM, a polarization controller and a fiber polarizing beam splitter are used. By adjusting the polarization controller, one can get interference fringes of two polarization states. An optical spectrum analyzer at the output of the beam splitter was employed to record interference fringes as depicted in Figure 2.6.

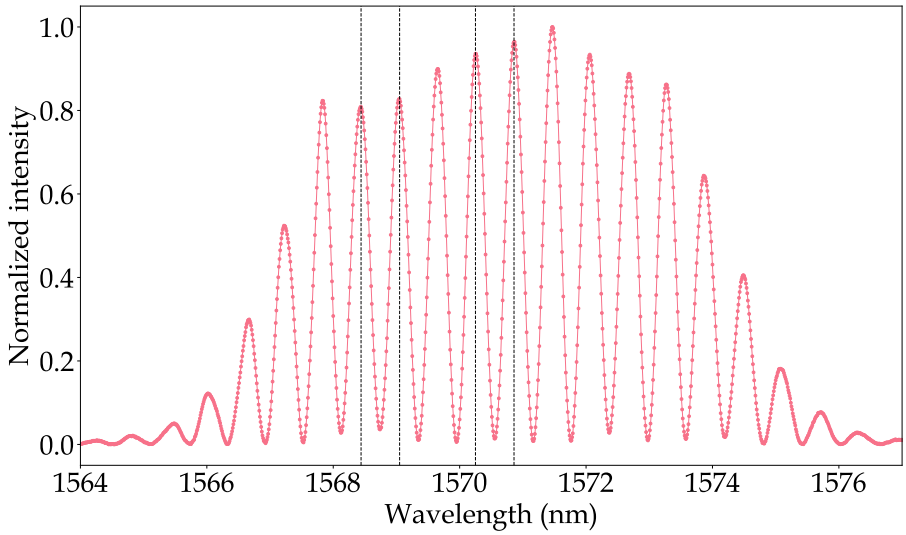

Figure 2.6: Spectral interference fringes resulting from delayed polarization components in the birefringent media of the EOPM

The delay time between polarization states of the optical pulse can be retrieved by taking inverse Fourier transform of the spectral interference pattern. In general, the distance between fringes in interference pattern has direct relation with delay time between interfering optical pulses from two arms of the interferometer. By considering the relation between the wavelength and oscillating frequency of the light, $\nu = c/\lambda$, and taking the derivative of this relation, we can work out the delay time.

$$\Delta\nu = |\frac{\lambda^2}{c\Delta\lambda}| \tag{2.26}$$

where c is speed of the light, λ is the central wavelength of the optical pulse and $\Delta\lambda$ is the separation of two adjacent fringes in the spectral interference pattern. The

delay time is calculated as $\Delta\tau = 1/\Delta\nu$. The average fringe separation as shown by vertical lines in Figure 2.6, was calculated. The delay time introduced by the EOPM is 11.7±0.5 ps. The delay time introduced by the calcite wedges, its thickest part is about 8 mm, used in the thesis was also measured 17.7±0.5 ps. For 1 meter of PM fiber, the delay time was measured about 1.5 ps.

2.5.4 Characterizing complex temporal phase modulation using temporal interferometry

Here a technique based on electro-optic sampling for characterizing complex temporal phase modulation of optical pulses is presented [60]. To implement the optical setup, the polarization MZI that has been discussed in the subsection 2.5.2 will be employed. After preparing the polarization MZI in its balanced mode, the time-varying voltage signal resulting from the fast photodiode as presented in subsection 2.5.1 is used to apply temporal phase modulation to ultrashort optical pulses propagating through the EOPM. A selected part of the fast photodiode response will be characterized as shown in Figure 2.7. In general, the electro-optic phase modulation process is a coherent operation that can be applied in single photons regime that is the ultimate goal of this research. So we first, demonstrate and confirm its performance by using classical pulsed laser and then it will be employed for applications to quantum light pulses in the next chapter.

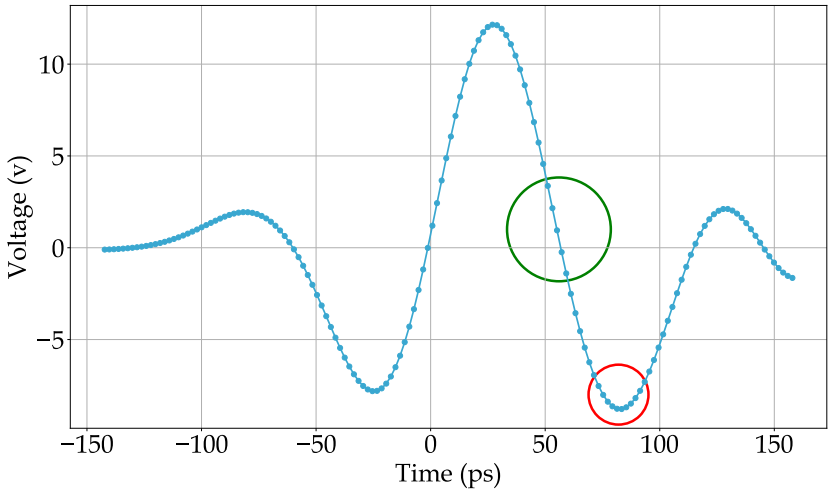

Figure 2.7: A selected part of the electronic response of the high-bandwidth photodiode

The EOPM is driven by a time-varying voltage signal with temporal duration longer than the duration of the optical pulse. In this case, when the optical pulse

propagates through the EOPM, it experiences a phase given by the instantaneous form of the temporally varying voltage as discussed in section 2.3. The challenge regarding the temporal phase modulation is related to synchronization of RF driving signal and optical pulse. Based on how these two signal are overlapped with each other, optical pulse undergoes various temporal phase modulation.

To implement the optical setup, the EOPM (EO-Space, 16 GHz bandwidth, V_π=3V @ 1 GHz) is fed by a modulating voltage signal from a high-bandwidth photodiode (12.5 GHz bandwidth, EOT ET-3500F). A free space delay line is used before the photodiode to scan modulating signal over the optical pulse passing through the EOPM. By using the polarization MZI, the EOPM and the delay line, it is possible to control the modulating signal and characterize phase modulation profiles applied to optical pulses. In particular, the linear and quadratic phase modulation profiles were characterized. For the case that optical pulse is temporally aligned with the quadratic part of the driving signal (shown by red circle in Figure 2.7), the result is quadratic phase modulation in time domain which provides spectral bandwidth modification in frequency domain. The other case is that optical pulse is temporally aligned with linear region of driving voltage (shown by green circle in Figure 2.7), that results linear temporal phase modulation which is correspond to spectral shift in frequency domain as earlier discussed in section 2.4.

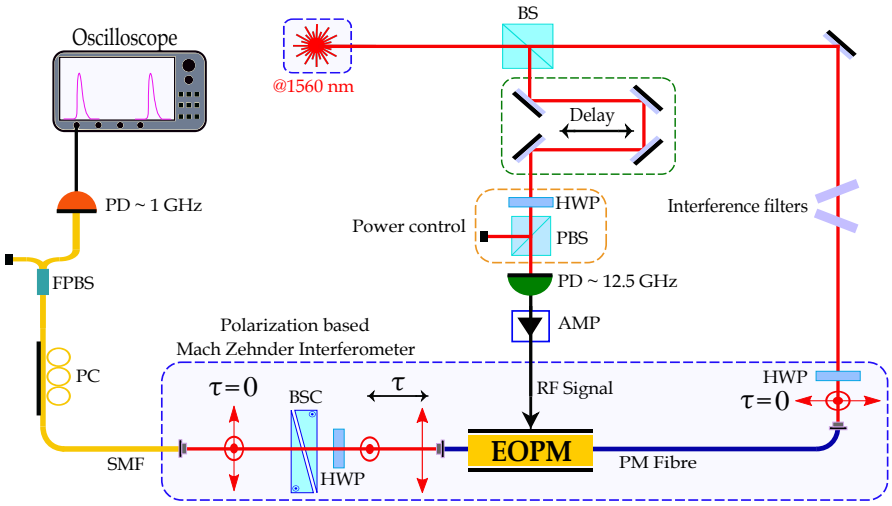

Figure 2.8: Optical setup for characterizing complex temporal phase modulation using temporal interferometry. BS : beam splitter, HWP : half wave plate, PBS : polarizing beam splitter, PD : photodiode, AMP : amplifier, EOPM : electro-optic phase modulator, PM Fiber : polarization maintaining fiber, SMF : single mode fiber, SBC: Soleil-Babinet compensator, FPBS: fiber polarizing beam splitter.

The optical setup for the measurement is shown in Figure 2.8. The optical pulses are taken from a femto-second laser oscillator at central wavelength of 1560 nm and coupled into optical fiber. The optical beam is divided using a fiber beam splitter into two paths. One path is directed into the polarization MZI after preparing the polarization states (horizontal and vertical) of the input optical pulse in a way that gives interference pattern with highest visibility. The polarization MZI consists of the EOPM, the calcite wedges and a specific length of PM fiber. By taking proper length of PM fiber and adjusting the thickness of the calcite wedges, one can manage and compensate the delay time between polarization components in the polarization MZI. The optical pulse at the output of the interferometer is directed into a polarizing beam splitter through a fiber polarization controller (FPC). Adjusting the FPC provides high visibility of the fringes resulting from interference between polarization states. By using a photodiode after the PBS and an oscilloscope, one can measure the intensity changes at the output of the inteferometer. The other path from the input laser oscillator is directed into a free space delay line and then coupled into the fast photodiode that produces modulating voltage signal. The voltage signal is amplified with a high-power amplifier (Mini-Circuits ZVE-3W-183+, 5-18 GHz, 3W) to deliver RF modulating signal to the EOPM. By changing the optical path length of the optical pulse incoming to the fast photodiode, different part of the RF modulating signal, as depicted in Figure 2.7, is synchronized with the optical pulse that results different phase modulation impact on the optical pulse.

In this temporal phase modulation process, one of the polarization states in the EOPM is mainly modulated and the polarization state is attenuated. So the modulated and the unmodulated polarization components are interfered using the PBS. The intensity of the output of the interferometer is described by the following relation in the time domain

$$I = I_H + I_V + 2\sqrt{I_H I_V}\cos\left[\Phi_{MZI} + \phi_{EOPM}(t)\right], \tag{2.27}$$

where I_H and I_V are the intensities of the horizontal and vertical polarization components before the polarizing beam splitter and t is the delay between optical pulse and modulating RF signal. And two interfering polarization components have a constant phase difference which results from the MZI and also a time dependent phase which comes from temporal phase modulation process Φ_{EOPM}. The intensity of the output is measured using a photodiode with bandwidth of 1 GHz. Note that the initial broadband optical pulses were filtered, to get spectral bandwidth about 1 nm, by using bandpass filter to avoid low visibility. Actually for the large bandwidth pulses, different spectral components are experienced different phase. So the reduced spectral bandwidth gives higher visibility. And by introducing phase shift with the wedges one can change the intensity from maximum (bright fringe) to minimum

(dark fringe).

2.6 Retrieving temporal phase modulation signal

The whole measured photodiode pulse as shown in Figure 2.4 has duration of 2 ns but we only take main part of the photodiode signal containing maxima and minima of the pulse with duration of about 200 ps to be characterized which is shown in Figure 2.7. The delay line in the optical setup gives possibility to scan the delay between optical pulse and RF modulating signal. An automated measurement setup was developed to record the temporal interference of modulated and reference pulses at output of the polarization MZI. Measured interference signal as a function of time is shown in Figure 2.9.

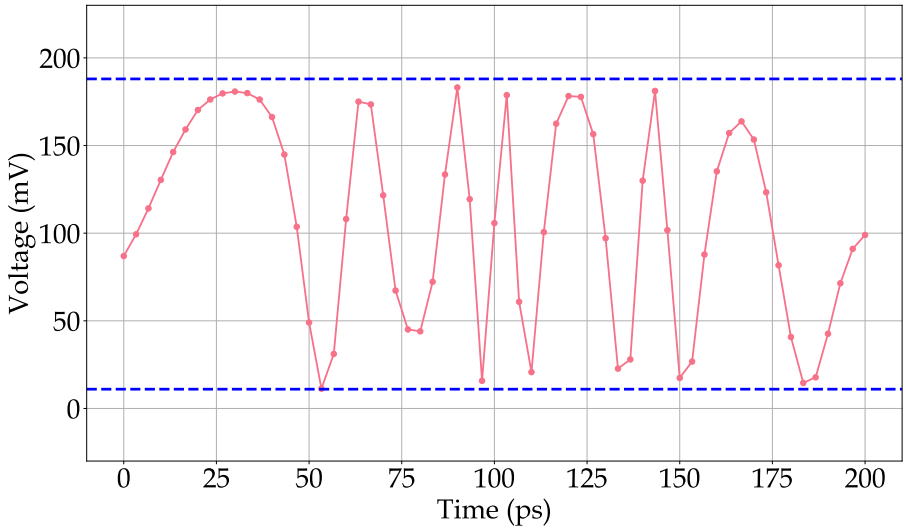

Figure 2.9: Measured interference signal between modulated and unmodulated optical pulses from two arms of the polarization MZI. The red line is used to guide the eye.

By scanning the delay time between the optical pulse and the RF modulating signal, time-varying temporal phase is applied, it results intensity change between bright and dark fringes of the interferometer. The measured interference signal can be described with the following formula [61, 62]

$$V(t) = V_0 + V_{pp} \cos\left[\varphi(t)\right], \tag{2.28}$$

where V_0 is mean voltage changes of the interference signal, V_{pp} is the peak-to-peak voltage that is correspond to fringe gap between bright and dark fringes, and $\varphi(t)$ is

the temporal phase profile that is going to be retrieved. The temporal phase profile can be calculated from the interference signal as

$$\varphi(t) = \arccos\left[\frac{V(t) - V_0}{V_{pp}}\right]. \tag{2.29}$$

The peak-to-peak amplitude, V_{pp}, of the photodiode pulse is about $\sim$ 20 V that is larger than half-wave voltage of the EOPM ($\sim$ 3.77 V), hence interference signal is wrapped as shown in Figure 2.10 (red line). After unwrapping, one can reconstruct the applied RF modulating signal as illustrated in Figure 2.10 (blue line).

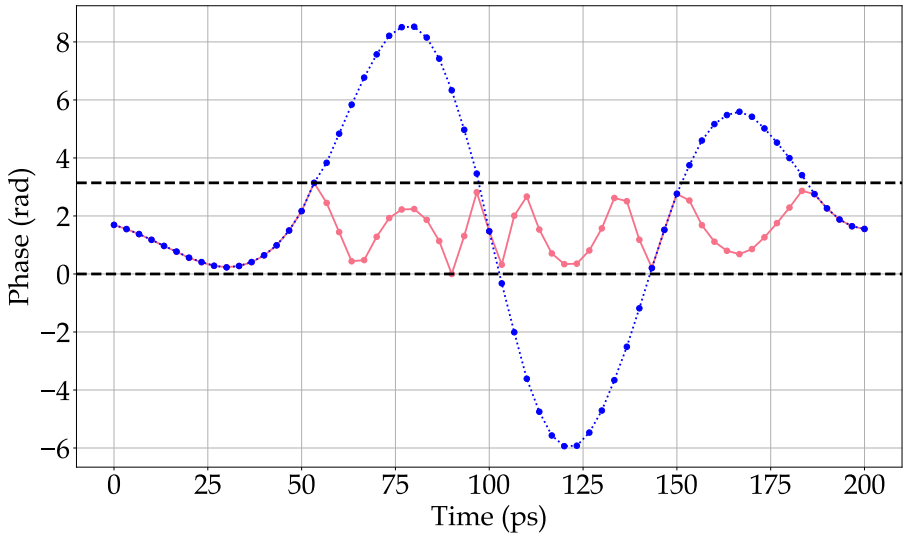

Figure 2.10: Measured retrieved phase temporal modulation signal resulting from temporal interferometry. Wrapped (red line) and unwrapped (blue line) retrieved temporal phase profile.

The reconstructed electronic waveform gives information about temporal phase applied at any individual point in time. So this enables us to characterize temporal phase modulation pattern in time domain and gives ability to study some features such as timing jitter which cannot be properly measured in spectral domain due to slow action of spectrum analyzers. This technique was further developed by Filip Sośnicki to enable characterization of timing jitter and amplitude noise of the RF signals.

Chapter 3

Measuring the temporal envelope of a quantum light pulse

3.1 Introduction

Coupling an electromagnetic field with an appropriate spectral and temporal features to vibrational and rotational motions of molecules promises a highly sensitive and informative probe that enables broad studies in physics, chemistry, biology and medicine [63]. Knowing and measuring the temporal and spectral properties of these effects gives an accurate information about such interactions. In this regard, ultrashort optical pulses have became essential for probing the dynamics of molecular systems and precision metrology [64, 65]. Apart from all these application, there has been significant interest in using ultrashort pulses in quantum technologies, such as quantum control of ultrafast processes in molecules [66], quantum computing [67, 68] and quantum sensing [69]. For all these applications, measuring the temporal intensity profile of an ultrashort optical pulse is a crucial characterization capability.

Up to date, the most well-developed techniques, based on intensity autocorrelation, use nonlinear optical effects such as second harmonic generation to characterize the ultrashort optical pulse [20]. But these techniques are only able to measure temporal duration and intensity profile of the optical pulse. There are also other well-developed techniques such as FROG [33] and SPIDER [37] that can not only measure the intensity profile of the optical pulse but also give information on phase profile as discussed in the first chapter. The main disadvantage regarding these technique is that they require to record traces of spectrum in order to extract the phase information that means using a spectrometer is a necessity. In addition, these methods still are not applicable in quantum regime due to using nonlinear interaction that can destroy quantum state of single photons. In this regard, developing new technique that is applicable in quantum technologies is a crucial requirement. In addition, characterizing the

ultrashort pulses in some wavelength regions are still challenging. This also requires developing techniques which are applicable for spectroscopic measurements where there is major difficulty because of the lack of efficient detectors and spectrometers.

In this chapter, an electro-optic and interferometric technique for measuring the temporal energy envelope of short single photon pulses based on tunable electro-optic spectral shearing interferometery is proposed. This method is the time-frequency Fourier analogue of Fourier-transform spectrometry that we call it, Fourier-transform chronometry. Unlike the traditional autocorrelations methods, introduced in Chapter 1, that rely on nonlinear techniques to measure short pulses, this method is a coherent and linear operation that allows to be employed to quantum light. In this interferometric method, the optical pulse is employed to measure itself. The optical pulse propagates through a balanced Mach-Zehnder interferometer where a tunable spectral shear is applied to one arm of the interferometer. The frequency of the optical pulse in this arm is scanned with respect to its replica in the reference arm by applying a well defined equally spaced spectral shear. Then a photodiode at the output of the interferometer is used to measure the integrated energy per pulse as a function of the spectral shear. This measurement yields an interference fringe pattern in the spectral domain. One can take the Fourier transform of the interference fringes to obtain the energy envelope of the optical pulse in time domain.

3.2 Conceptual description of the electro-optic Fourier transform chronometry

In this section, a new interferometric method for measuring temporal profile of short pulses is described that is called Fourier transform chronometry. This technique is time-frequency Fourier transform of the Fourier transform spectrometry (FTS) that is a well-known technique for measuring spectral profile of light. The FTS, as shown in Figure 3.1, is basically an Michelson interferometer in which a tunable time shift is applied in one arm of the interferometer by changing position of the movable mirror over some range. Consider an electric field from laser source that is splitted into two arms of the interferometer. One beam is reflected from the fixed mirror, $E(t)$, and other beam is delayed by, τ, and reflected from the movable, $E(t+\tau)$, then both beams are interfered at the beam splitter.

$$\Gamma(\tau) = \langle E(t)E(t+\tau)\rangle \tag{3.1}$$

By changing the tunable temporal shift, field autocorrelation is measured and the interference signal at the output of the interferometer is recorded as a function of temporal shift using a photodiode. One can take Fourier transform to obtain the

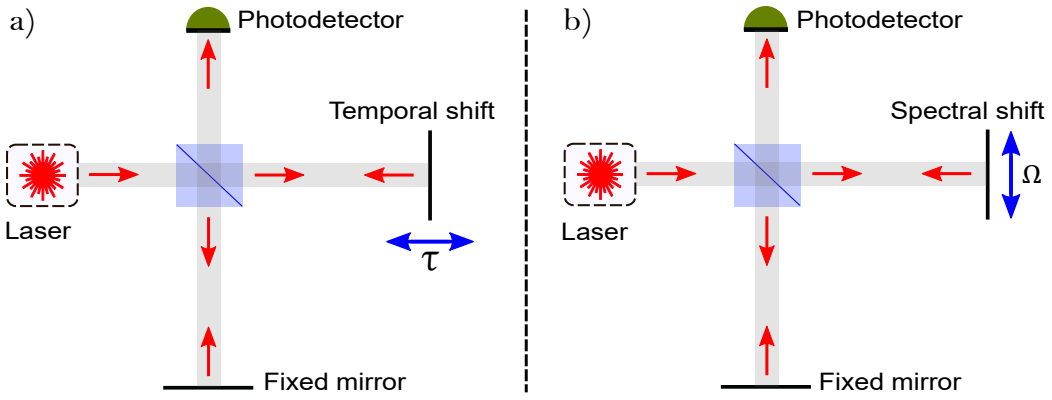

Figure 3.1: Schematic of autocorrelation of optical field in time and frequency domains. a) schematic of Fourier transform spectrometry, b) schematic of Fourier transform chronometry

intensity profile of the light in spectral domain.

$$|\tilde{E}(\omega)|^2 = \mathcal{F}\{\Gamma(\tau)\}. \tag{3.2}$$

Based on the FTS method, here, the Fourier Transform Chronometry (FTC) is introduced. It can be viewed as interchanging the roles of time and frequency in FTS where instead of applying the temporal shift in one arm of the interferometer, a tunable spectral shift, Ω, is applied in the FTC scheme as illustrated in Figure 3.1. In fact, in the FTC, frequency autocorrelation of the field is performed as

$$\tilde{\Gamma}(\Omega) = \langle \tilde{E}(\omega)\tilde{E}(\omega+\Omega)\rangle \tag{3.3}$$

Similar to the FTS technique, the interference signal at the output of the interferometer is recorded as a function of spectral shift using the photodiode. By taking the Fourier transform of the interference signal, the temporal profile of the light pulse can be obtained.

$$|E(t)|^2 = \mathcal{F}\{\tilde{\Gamma}(\Omega)\}. \tag{3.4}$$

To implement the FTC technique, a tunable spectral shear needs to be prepared. This will be done using electro-optic temporal phase modulation process where by applying linear temporal phase to a electro-optic phase modulator, the optical pulse will experience spectral shift in the frequency domain as discussed in Chapter 2.

3.3 Theoretical description of the electro-optic Fourier transform chronometry

The theoretical basis of FTC closely parallels that of FTS, with time and frequency variables swapped and the role of the tunable delay substituted for tunable spectral shear in one arm of the interferometer. The following section, theoretical description of the FTC technique, is based on a note prepared by Alex O. C. Davis that has not been published.

A pulsed optical mode can be represented as a modulation of a carrier wave with frequency ω_0 as following

$$E(t) = \varepsilon(t) \exp\left[i\omega_0(t - t_0)\right], \tag{3.5}$$

where $\varepsilon(t)$ is a slowly-varying temporal mode function which we will assume is centred on $t = 0$. A spectral shear can be imparted by the modulation of the field with an additional phase term that is linear in time, $\exp\left[i\Omega(t - t_0)\right]$. In a refractive medium, this modulation can be achieved by a linear inclination in the index which co-propagates with the pulse [57]. The reference time $t = t_0$ is the zero crossing of this linear phase modulation: if this is displaced from the pulse centre of energy ($t_0 \neq 0$), the sheared pulse will also acquire a global phase offset of Ωt_0 relative to the unsheared reference pulse. The effect of the spectral shear can then be represented as changing the frequency of the carrier wave, $\omega_0 \to \omega_0 + \Omega$ as illustrated in Figure 3.2.

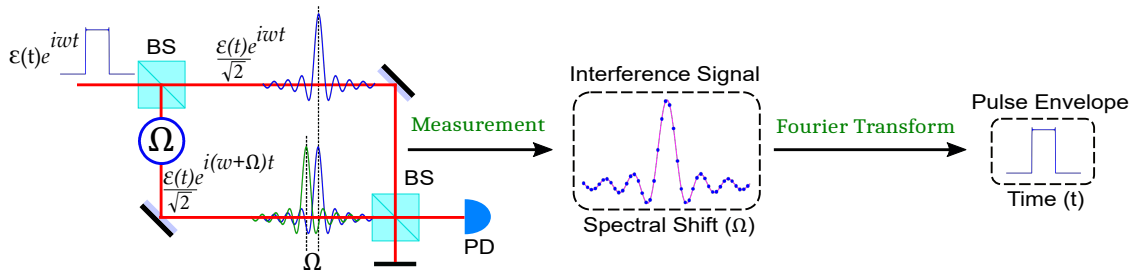

Figure 3.2: Schematic of the Fourier transform tunable electrooptic spectral shearing interferometry. BS, beam splitter; PD, photodiode

The electric field at one output of the interferometer may therefore be written [70]

$$E_\Omega(t) = \frac{1}{\sqrt{2}}\Big\{\varepsilon(t) \exp\left[i\omega_0(t - t_0)\right] + \varepsilon(t) \exp\left[i(\omega_0 + \Omega)(t - t_0)\right]\Big\}. \tag{3.6}$$

The intensity at the output is then

$$I_\Omega(t) \equiv |E_\Omega(t)|^2 = I_0(t)\Big\{1 + \frac{1}{2}\exp\left[i\Omega(t-t_0)\right] + \frac{1}{2}\exp\left[-i\Omega(t-t_0)\right]\Big\}, \tag{3.7}$$

where $I_0(t) \equiv |\varepsilon(t)|^2$ has some characteristic duration ΔT. For single-picosecond and femtosecond pulses ΔT is too short to be resolvable to detectors. In other words, the integration time for the detector is much longer than the envelope of the pulse. Hence all that is accessible is the integrated energy per pulse at an output port of the interferometer as a function of Ω:

$$\begin{aligned}\mathcal{E}(\Omega) &\equiv \int I_\Omega(t)\mathrm{d}t \qquad (3.8)\\ &= \mathcal{E}_0 + \frac{1}{2}\int\Big\{I_0(t)\exp\left[i\Omega(t-t_0)\right] + I_0(t)\exp\left[-i\Omega(t-t_0)\right]\Big\}\mathrm{d}t\\ &= \mathcal{E}_0 + \frac{1}{2}\exp\left[-i\Omega t_0\right]\mathcal{F}^{-1}\Big\{I_0(t)\Big\} + \frac{1}{2}\exp\left[i\Omega t_0\right]\mathcal{F}^{-1}\Big\{I_0(-t)\Big\},\end{aligned}$$

where $\mathcal{E}_0 \equiv \int I_0(t)\mathrm{d}t$ and $\mathcal{F}$ $(\mathcal{F}^{-1})$ denotes the (inverse) Fourier transform with respect to $\{t, \Omega\}$. We then calculate the Fourier transform of $\mathcal{E}(\Omega)$ with respect to Ω to obtain the pseudo-temporal intensity:

$$\bar{I}(T) \equiv \mathcal{F}\{\mathcal{E}(\Omega)\} \tag{3.9}$$

$$= \mathcal{E}_0\delta(T) + \frac{I_0(T-t_0)}{2} + \frac{I_0(-T+t_0)}{2}, \tag{3.10}$$

where $\delta(T)$ is the Dirac delta function. Hence, if $t_0 \gg \Delta T$, the distinct side-peaks can be isolated and directly identified with the temporal intensity distribution $I_0(t)$ of the original pulse. The time reference t_0 determines the fringe spacing in the interferogram $\mathcal{E}(\Omega)$, and hence the peak separation in $\bar{I}(T)$. In FTS, if the delay over which the interferometer is scanned is shorter than the optical period, then there is no prospect of seeing a full interference fringe and hence isolating the variational term from the d.c. term. Similarly, if t_0 is too small relative to the range over which the shear is scanned, then there will not be a full cycle of interference at the output over the scan of Ω. The zero-crossing of the temporal phase must be offset from the centre of the pulse by some amount exceeding the inverse of the maximum shear. This is illustrated in Figure 3.3. Its analogue in FTS is the centre frequency of the pulse.

In practice, $\mathcal{E}(\Omega)$ can only be measured over some finite range $\Delta\Omega$, so the terms in Equation 3.10 are convolved with a point-spread function with width $\sim 1/\Delta\Omega$. For the peaks to be distinct we therefore also require $t_0 \gg 1/\Delta\Omega$.

For a maximum achievable spectral shear of hundreds of gigahertz, this condition implies t_0 of several picoseconds. In practice it is difficult to sustain maximum

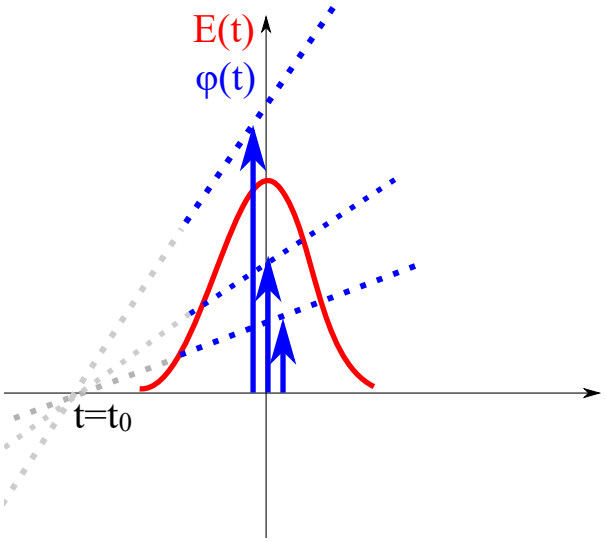

Figure 3.3: In practice, the temporal phase (blue dotted lines) only needs to approximate its correct form over the duration of the pulse: outside this range (grey dotted lines) it can follow an arbitrary profile. The correct form can be obtained by locking the linear temporal phase to the centre of the pulse and then applying a global constant phase that is proportional to Ω (solid blue arrows).

spectral shear over such a duration. Fortunately, the temporal phase only needs to resemble a linear ramp (with some offset) over the period where the pulse has significant intensity. We achieve this by locking the linear part of the ramp to the centre of the pulse and effecting the nonzero value of t_0 by applying a global phase offset proportional to Ω (modulo 2π). Ideally, this would be a global offset phase that would be independent of frequency, e.g. by an achromatic phase shifter. In the experiment, I used calcite wedges in the form of Babinet–Soleil compensator to apply this global offset phase as shown in Figure 3.9.

3.4 Implementation of tunable spectral shifting interferometry

In this section, experimental realization of the tunable spectral shearing interferometry is described. To implement such an optical setup, a Mach-Zehnder interferometer is used where a tunable spectral shift is applied in one arm of the interferometer as shown in Figure 3.4. An optical pulse is split into two arms of the interferometer in which one arm acts as reference and the arm has an electro-optic phase modulator

(EOPM) that the test arm.

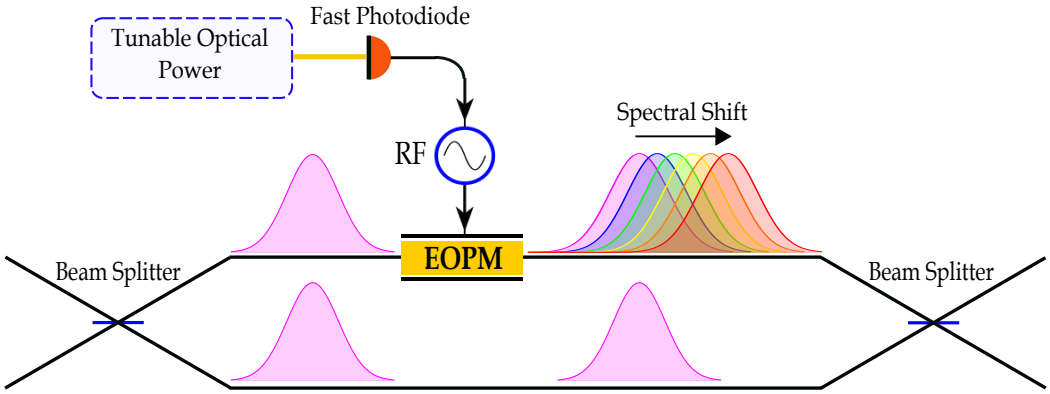

Figure 3.4: Conceptual schematic for implementation of electro-optic tunable spectral shearing interferometry.

The required spectral shift is imparted using the EOPM. To perform the spectral shift, a linear temporal phase is required to be applied the modulator as discussed in subsection 2.4.1. In this scheme, the EOPM is modulated by amplified voltage signal from a high bandwidth photodiode that has been characterized and presented in section 2.6. The linear part of the photodiode's voltage signal is temporally synchronized with the optical pulse passing through the modulator that results the spectral shift of the optical pulse in the spectrum. The introduced spectral shift is controlled by applied optical power that is fed to the photodiode. The interference signal at the output of the interferometer is measured as a function of the spectral shear.

3.4.1 Controlling the spectral shift

To establish the optical setup for performing the tunable spectral shearing interferometry, the first task is to prepare a tunable linear temporal phase profile. Considering Equation 2.25, the temporally varying phase is depend on voltage signal that is applied to the EOPM. By controlling the slope of the linear part of the voltage signal (amplified signal from the photodiode), one can modify the applied temporal phase to the modulator that results the spectral shift in the spectral domain. The spectral shear is proportional to the slope of the linear temporal phase. By increasing the slope of the linear temporal phase, increasing the optical power to the fast photodiode, one can apply a larger spectral shift to the optical pulse. In Figure 3.5, the temporal phase profile as a function of the applied optical power to the photodiode is illustrated.

As seen in Figure 3.5, the slope of the linear part of the phase profile, located around 100 ps, is small when the applied optical power to the photodiode is low.

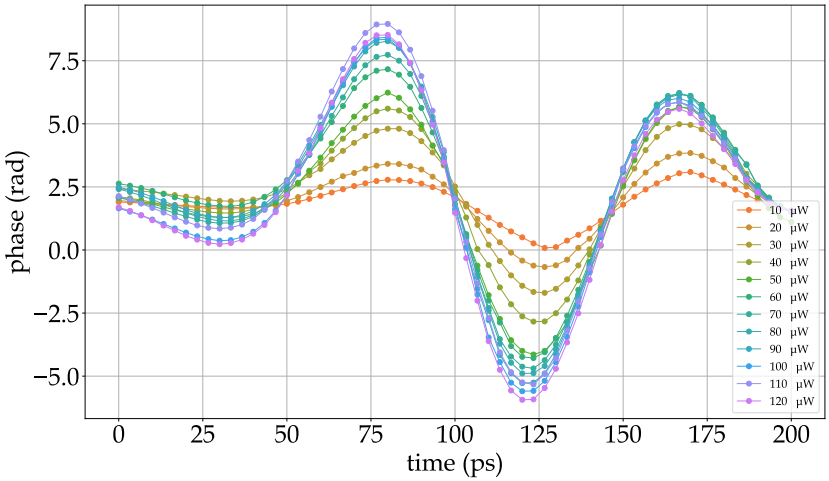

Figure 3.5: Retrieved temporal phase modulation signal measured by temporal interferometry. The temporal phase profile changes as applied input optical power to the fast photodiode increases.

This slope increases when a higher optical power, for example 120 μW, is applied. The temporal phase profiles, presented in the figure, was retrieved by temporal interferometry technique as it was described in section 2.6. By looking at the changes in Figure 3.5, one can find that the response of the photodiode is not linear. In order to control the applied spectral shift, it is required to calibrate the input optical power to the photodiode to get an uniform changes of applied spectral shift. Figure 3.7 illustrates the nonlinear change of the introduced spectral shift as function of applied power to the photodiode. This show that the photodiode gets saturated around 120 μW and does't introduce more spectral shift for a higher input power.

3.4.2 Calibrating applied spectral shift

As mentioned in the introduction section, this measurement technique relies on the Fourier transform of the spectral interference fringe pattern. So it is crucial to apply an equally spaced spectral shift to avoid noise in the Fourier domain. This requires calibration of the nonlinear response of the fast photodiode with respect to the applied input power. For this purpose, a set of half-wave plate (HWP) and polarizing beam splitter (PBS) is employed to control the applied optical power to the high bandwidth photodiode as shown in Figure 3.6. As discussed in the previous subsection, the photodiode's response nonlinearly changes with the applied power to the photodiode that needs to be calibrated to achieve equally spaced spectral shift since the uneven sampling of data increases the noise in the Fourier domain and results in accuracy degradation [71].

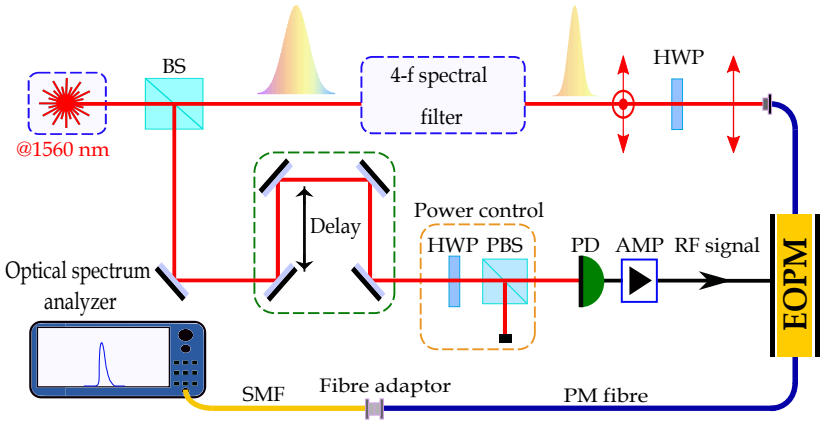

Figure 3.6: Optical setup for calibrating the applied spectral shift. BS : beam splitter, HWP : half wave plate, PBS : polarizing beam splitter, PD : photodiode, AMP : amplifier, EOPM : electro-optic phase modulator, PM Fiber : polarization maintaining fiber, SMF : single mode fiber

The calibration was done by using the optical setup depicted in Figure 3.6 where optical pulses with bandwidth of 0.5 nm were prepared by employing a 4-f spectral filter. Then they are directed into the EOPM after setting the polarization of the light along one of polarization axes of the EOPM at which the temporal phase modulation is applied. The linear part of the RF voltage signal is synchronized to the optical pulses passing through the EOPM using an optical delay line. By modifying the HWP rotation, shown in power control section of the optical setup, it is possible to adjust proper increment of the applied optical power in order to obtain a linear increase of the spectral shift. The shifted optical pulse is monitored by an optical spectrum analyzer to find required rotation of the HWP at each spectral shift step. This calibration was done to implement equally spaced spectral shift with steps of 0.01 nm. In Figure 3.7, the calibrated spectral shift as a function of applied optical power to the phododiode is shown.

In this figure, the red curve is the calibrated spectral shift that is kept as reference. In practice, there is still non-accuracy of mechanical movement of the HWP that will introduce non-uniformity in the applied spectral shift. To overcome this issue, the applied optical power is monitored during the measurement process to be used for correcting the applied spectral shift based on the reference spectral shift, the red curve, through automated data processing. The blue curve in Figure 3.7 shows an example of deviation of the applied spectral shift from the reference spectral shift profile during the measurement.

Now, limiting factors of this interferometric device for measuring short optical pulses are investigated. Considering the characteristics of the EOPM, the high

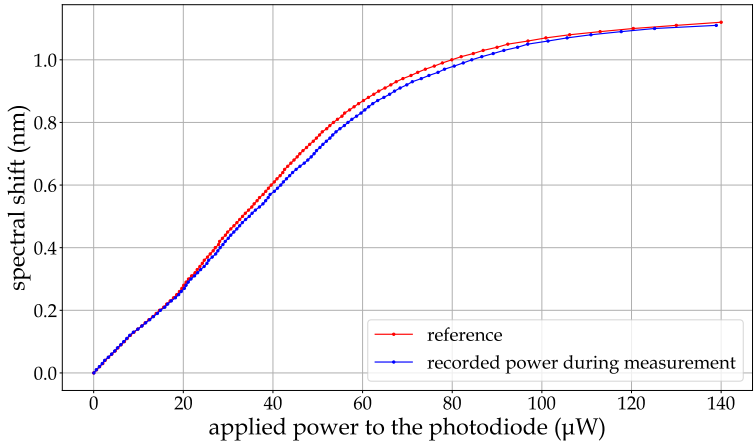

Figure 3.7: Introduced spectral shift as function of applied power to the fast photodiode. The red curve is the reference spectral shift and the blue curve is an example of deviated spectral shift during a typical measurement.

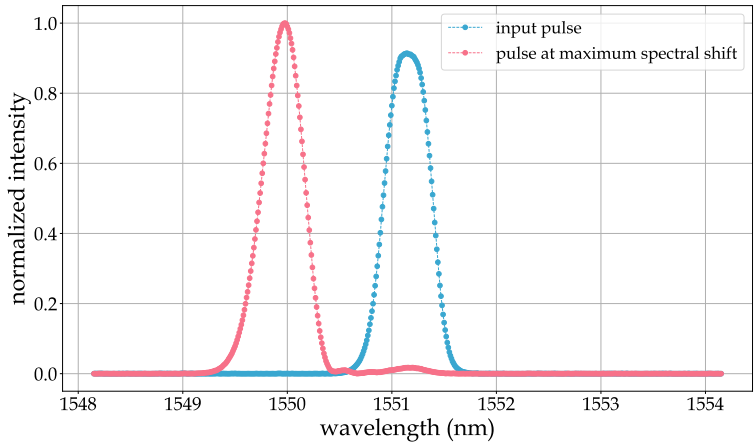

Figure 3.8: Input optical pulse with FWHM of 0.5 nm in the spectral domain (blue line). The optical pulse at maximum spectral shit (red line).

bandwidth photodiode and the amplifier employed in the optical setup, the maximum achievable spectral shift is 1.22 nm that implies that this measurement apparatus can measure the optical pulse with maximum input bandwidth of up to about 0.6 nm. With this criteria, the optical pulse in the test arm of the interferometer can be fully scanned with respect to its replica in the reference arm of the interferometer that defines the maximum bandwidth of the input optical pulse. On the other hand, the minimum bandwidth also can be determined. Taking the linear part of the retrieved temporal phase profile as illustrated in Figure 3.7, one can calculate the time duration of the linear region of the RF modulating signal. The test optical pulse must be

located in and not be exceeded from this linear region so that receives only spectral shift during temporal phase modulation process. The temporal duration of this linear region was measured to be about 25 ps. This linear temporal window defines the maximum temporal width (the minimum spectral bandwidth) of the input test optical pulse that can be sent into the EOPM to have an ideal spectral shift without a significant undesired distortion of the optical pulse.

As mentioned earlier, in this experiment, the optical pulse with bandwidth of 0.5 nm was considered which ensures that the optical pulse remains in the linear part of the RF modulating signal. In Figure 3.8, the blue line indicates the spectrum of the input optical pulse. This figure also illustrates the optical pulse after imparting maximum achievable spectral shift that results from applying optical power of 120 μW to the high bandwidth photodiode.

3.5 Interferometric optical setup with incorporated phase shifter

After preparing a tunable spectral shear, now, a polarization based interferometer is developed to be used for measuring short optical pulses. The interferometer was implemented based on interfering of polarization components of light that was elaborated in subsection 2.5.2. For this experiment, an interferometric optical setup as shown in Figure 3.9 was established in which an optical pulse from a femtosecond laser at 1550 nm is taken and directed into a 4-f spectral filter to prepare an optical pulse with 0.5 nm bandwidth. Then the optical pulse is sent through a polarization-based Mach-Zehnder interferometer to measure the temporal energy envelope of ultrashort optical pulses. In such a scheme, optical pulses with diagonal polarization components are directed into the EOPM. The polarization components propagate through birefringent materials including the EOPM and polarization maintaining fibers so they experience a delay. This delay can be compensated by swapping polarization components and using a proper thickness of birefringent material such as a calcite Babinet–Soleil compensator. In order to perform phase modulation, an arriving RF signal ($\sim$ 10 GHz) is required. Here an amplified electronic signal from the high bandwidth photodiode ($\sim$ 12.5 GHz) was used, as explained in subsection 3.4.2, to apply desired linear temporal phase profile to the optical pulses [72]. A portion of the optical pulses is split off to feed the high bandwidth photodiode. As shown in Figure 3.9, a variable delay line is employed to synchronize the linear part of the RF modulating signal to the optical pulse. The applied spectral shift is also tuned using the HWP and the PBS before the high bandwidth photodiode.

In practice, the change of slope of the applied temporal phase changes the spectral shift but does not introduce an appropriate value of the phase shift in the inter-

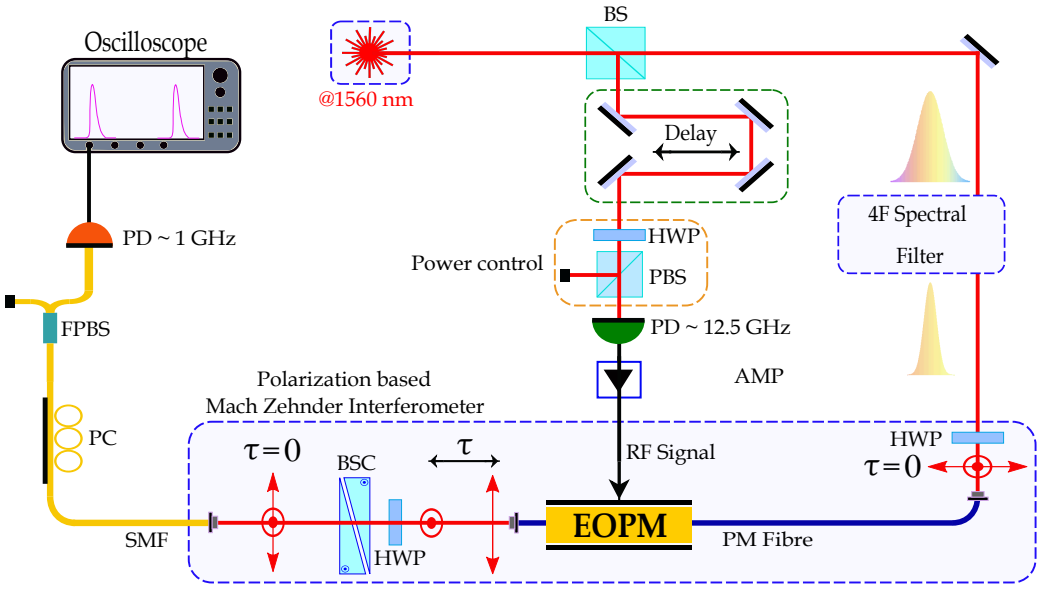

Figure 3.9: Interferometric optical setup with incorporated phase shifter. BS : beam splitter, HWP : half wave plate, PBS : polarizing beam splitter, PD : photodiode, AMP : amplifier, EOPM : electro-optic phase modulator, PM Fiber : polarization maintaining fiber, SMF : single mode fiber, BSC : Babinet–Soleil compensator, PC : polarization controller, FPBS : fiber polarizing beam splitter

ferometer necessary for obtaining dense interference fringes that is required to get information through data analysis. So one needs to apply a global constant phase shift which is proportional to the spectral shear. This can be done using the incorporated phase shifter in the interferometer i.e. the Babinet–Soleil compensator (BSC) that will be explained in subsection 3.5.1. Note that combination of the EOPM, the BSC and a piece of PM fiber constitute the polarization MZI in which all these elements are made of birefringent material. By adjusting the polarization states of the light pulse using the HWP in the interferometer and taking sufficient thickness of the calcite wedges, one can compensate the delay time, τ, between polarization components of the light pulse to get a balanced interferometer as indicated in Figure 3.9 as described earlier in subsection 2.5.2. Another point is that the EOPM applies the temporal phase into one of the polarization components and attenuates the other polarization component. To get the highest interference visibility at the output of the interferometer, one needs to balance the power ratio of the polarization components by adjusting the HWP at the input of the interferometer (just before the EOPM) and also adjusting the polarization controller just before the fiber polarizing beam spliter. Then, another photodiode (Thorlabs DET01CFC, bandwidth 1.2 GHz) and an oscilloscope are used to measure

intensity changes at the output of the interferometer.

3.5.1 Phase shifter based on Babinet–Soleil compensator

The polarization-based interferometer used in the experiment consists of an EOPM and a calcite Babinet–Soleil compensator in which the calcite wedges are used to compensate the delay between diagonal polarization components but they can simultaneously used to introduce a phase shift. One needs to precisely control the movement of the wedges to produce a global constant phase shift, which is proportional to the spectral shear, after each change in the slope of the linear temporal phase. The movement of wedges leads to phase shift between interferometer's arms which results in bright and dark fringes at the output of the interferometer. Such a consecutive and controlled movements leads to a fringe pattern at the output of the interferometer. The amount of the global constant phase shift should not be too large such that we miss a fringe through the measurement. A smaller global constant phase shift gives clear fringes but it leads to a longer measurement process that is undesirable as the interferometer becomes unstable in long run measurement. So the global constant phase shift was chosen in a way that avoids down sampling in interference fringe pattern and allows a faster measurement process.

One important point regarding the movement of the calcite wedges is the uniformity of the introduced phase shift in consecutive movements of the wedges. In order to verify the uniformity of the introduced phase shift, the intensity at the output of the interferometer was measured as function of the movement of the calcite wedges as illustrated in Figure 3.10. In this investigation, there was no phase modulation process so that we can only measure the introduced phase shift that comes from movement of wedges in the interferometer.

The calcite wedges used in the Babinet–Soleil compensator usually work for a wide range of wavelengths (i.e., about hundred nanometer), so the obtained retardance has weak wavelength dependence. In addition, changing the thickness of the calcite wedges may effect the introduced phase shift. So this needs to be checked over the range of the change of the wedges' thickness. In the experiment, it is required to change the wedges' thickness for a total range of 0.5 mm by steps of 0.00625 mm. This constant step is correspond to the global constant phase shift which is proportional to the required spectral shear of 0.01 nm. One can unwrap the fringe pattern to obtain the phase profile over the wedges' movement range as shown by blue line in Figure 3.11.

For equal movements of the wedges, a linear phase profile with constant phase changes is expected. However, introduced retardance is not changed uniformly for equal movement of the wedges. Also there might be an unequal movement for the wedges due to mechanical action for moving the wedges. In Figure 3.11, the blue line

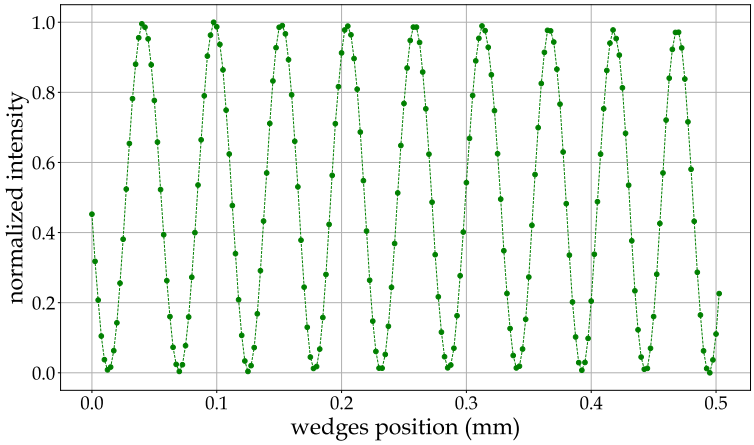

Figure 3.10: Phase changes between dark and bright fringes of the interferometer as a function of movement of the calcite wedges (phase shifter)

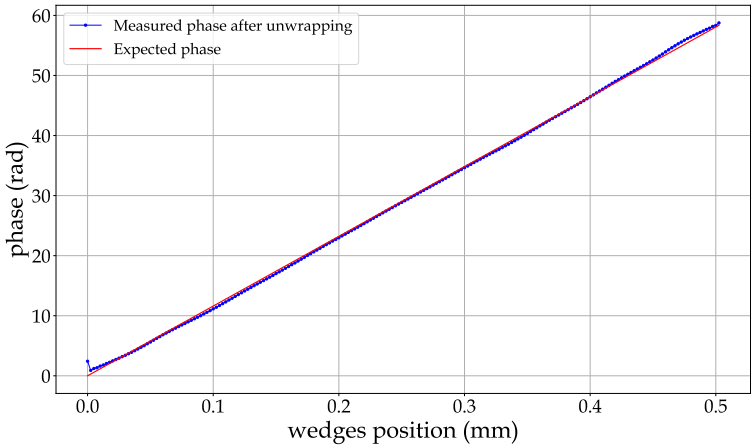

Figure 3.11: Unwrapped phase profile over movement of the calcite wedges (phase shifter)

shows the measured introduced phase after unwrapping while the red line indicates the expected linear increase of the phase change. For the equal movements of the wedges, a constant value of 0.29 rad is expected for the phase change at every step (red line) while the measured phase profile shows non-uniform phase change (blue line). For this measurement, the standard deviation of differential values for the measured phase changes gives about 3 percent relative error. This includes errors that comes from introduced retardance because of wedges' thickness change and possible unequal movement of the wedges. It is relatively small error that can be neglected.

3.6 Measurement procedure

The experiment was done in the conditions that the interferometer is set in its balanced case and the optical pulse is placed in the centre of the linear part of the electronic RF signal using the fiber-coupled variable delay line. Then the linear temporal phase is imprinted by the RF signal applied to the EOPM which results in a spectral shear. The optical setup is shown in Figure 3.9. At first, the optical power to the high bandwidth photodiode is set to almost zero power so that there is no spectral shear. In this case, both optical pulses from two arms of the interferometer have full overlap in spectral domain. The output of the interferometer is also set at bright fringe by using the phase shifter. The spectral shift is consecutively increased by 0.01 nm steps. This was done in a controlled manner using predefined rotations of the HWP that applies required optical power on the high bandwidth photodiode to apply equally spaced spectral shift. In each step, the optical pulse in one arm of the interferometer is spectrally shifted by 0.01 nm with respect to its replica in the other arm of the interferometer. Note that after each step of spectral shift, a global constant phase shift which is proportional to the spectral shift is applied using the phase shifter. The integrated energy per pulse at one output port of the interferometer is measured using a photodiode and recorded by an oscilloscope. This process is sequentially repeated until the spectrally sheared pulse scans its replica so that there is almost no overlap between pulses from arms of the interferometer in spectral domain. Figure 3.8 shows the optical pulse with maximum spectral shift (red line) and without spectral shift (blue line). For the whole measurement procedure, I wrote a Python code to control and move the optical devices (half-wave plate and phase shifter) and also to communicate with electronic devices (oscilloscope, spectrometer and time tagger). This made it possible to automatically perform measurement and do the data collection and processing.

3.7 Measuring temporal duration of the pulsed classical light

For this experiment, the optical pulse with input spectral bandwidth of 0.5 nm was considered. And total spectral shear of 1.22 nm was applied to the optical pulse in one arm of the interferometer, in sequential steps of 0.01 nm, to scan the optical pulse with respect to its replica in the other arm of the interferometer. Figure 3.12 shows the measured intensity at the output of the interferometer as function of spectral shear. As it is seen in the figure, the fringe visibility decreases with increasing spectral shift due to the reduction in pulse overlap in the spectral domain. In this experiment,

the spectral shift was performed only in one direction (blue shift) that results fringe pattern for half of the optical pulse. Then we mirror the pattern to get full fringe pattern that is illustrated in Figure 3.13.

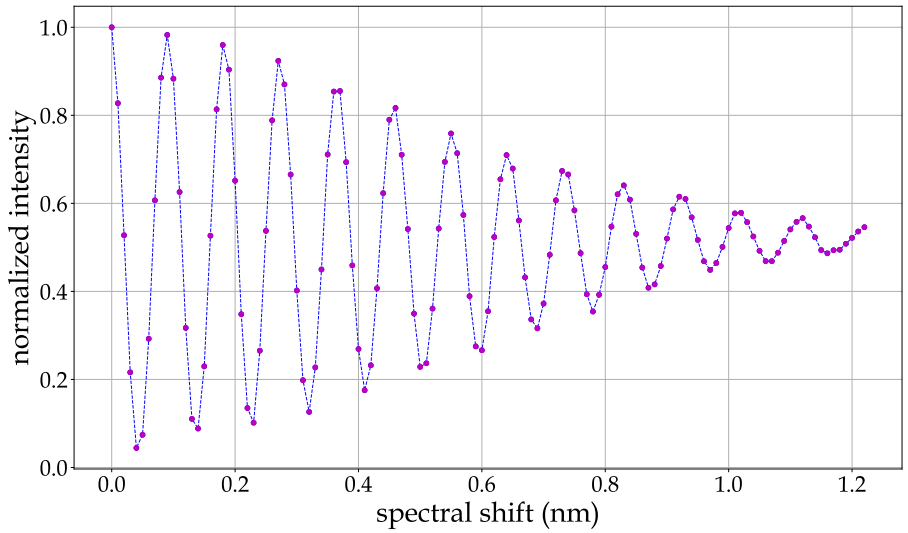

Figure 3.12: Measured interference signal as a function of spectral shift

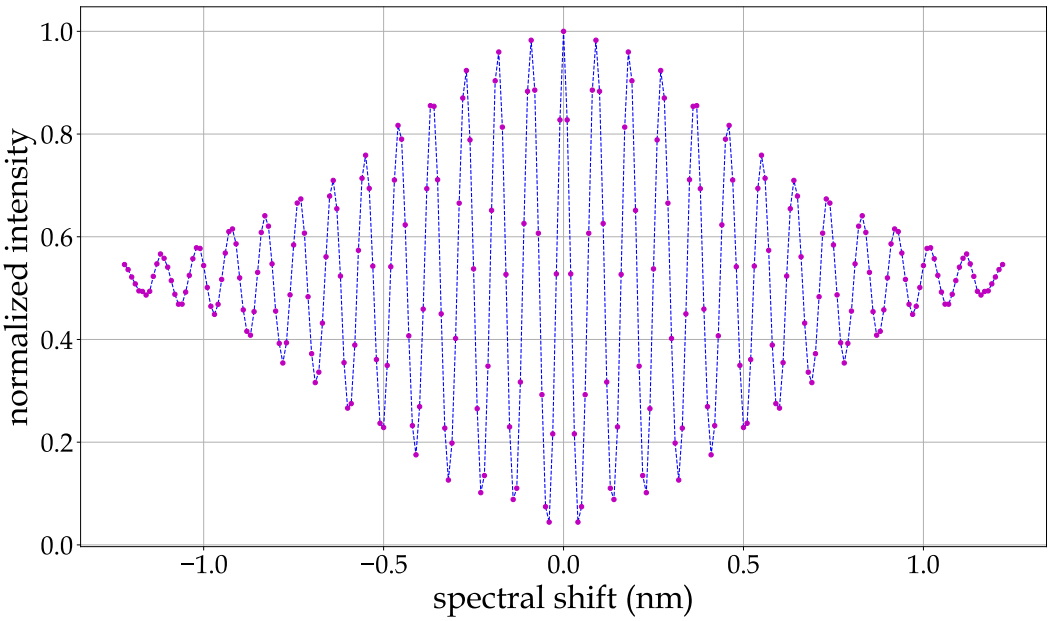

Figure 3.13: Full interference signal in which the negative side is the mirror of the measured data. The blue line is used to guide the eye.

In order to measure the temporal energy envelope of the optical pulse, one needs to

take a Fourier transform of the interference fringes. By taking a fast Fourier transform of the fringe pattern and defining the proper time scale, the temporal profile of the optical pulse is achieved as shown in Figure 3.14.

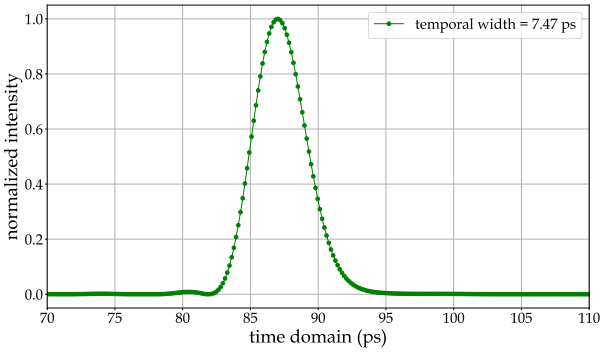

Figure 3.14: Energy envelope of the measured optical pulse in temporal domain

From the temporal intensity of the optical pulse, the calculated root mean square (RMS) temporal width of the optical pulse is 7.48 $\pm$ 0.02 ps which is relatively close to theoretical expectations for the optical pulse with 0.5 nm spectral bandwidth calculated based on the RMS pulse width calculation. The measurement was performed over a range of input bandwidths, measuring the change in temporal duration of classical optical pulses as indicated by the green points in Figure 3.15 in which input bandwidth is taken from 0.5 nm to 0.6 nm. Considering characteristics of the employed EOPM, V_π = 3 V, and the RF modulating signal, the maximum spectral shift is limited to about 1.2 nm. In order to fully scan the optical pulse in the spectrum, it is not possible to take an input spectral width larger than 0.6 nm with the present setup. On the other hand, the lower limit of the input bandwidth is 0.5 nm that ensures us that the temporal distribution of the optical pulse remains in the linear region of RF modulating signal. As shown in Figure 3.15, the results indicate that increasing the input bandwidth leads to the expected decrease in temporal duration. The measurement was repeated four times to estimate the relative error in temporal width measurement.

This measurement was also done by a direct approach where the temporal pulse duration of the classical pulse was experimentally measured using an optical complex spectrum analyzer (APEX Technologies AP2681A) as shown by black points in Figure 3.15. The difference in the measured temporal width in comparing between results of the interferometric and direct measurement approaches comes from residual distortion of the optical pulse spectrum when the spectral shear is applied, as it is confirmed by the theoretical simulation in the next subsection.

To present the shape of the input optical pulse with 0.5 nm bandwidth in time and frequency domain, the spectral profile (measured by an optical spectrum ana-

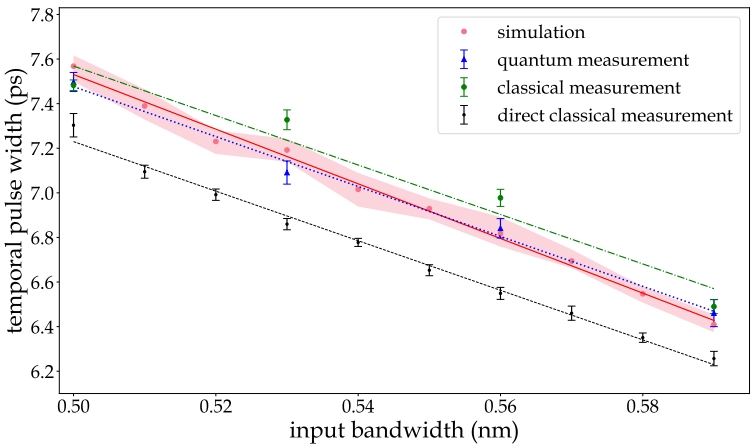

Figure 3.15: Impact of input bandwidth change on temporal width of the classical (green points) and quantum (blue points) light pulse—experimental data along with linear fits as shown by green dash-dotted and blue dotted lines respectively. Red points: theoretical simulation. The temporal pulse width is calculated based on the RMS pulse width calculation. The red shaded area shows the variation of temporal pulse width for up to 10 percent error in the applied spectral shift. The direct measurement of the temporal duration of the classical pulses using the optical complex spectrum analyzer is shown by black points along with linear fit as indicated by the black dashed line.

lyzer) and temporal profile (measured by the optical complex spectrum analyzer) is presented in Figure 3.16.

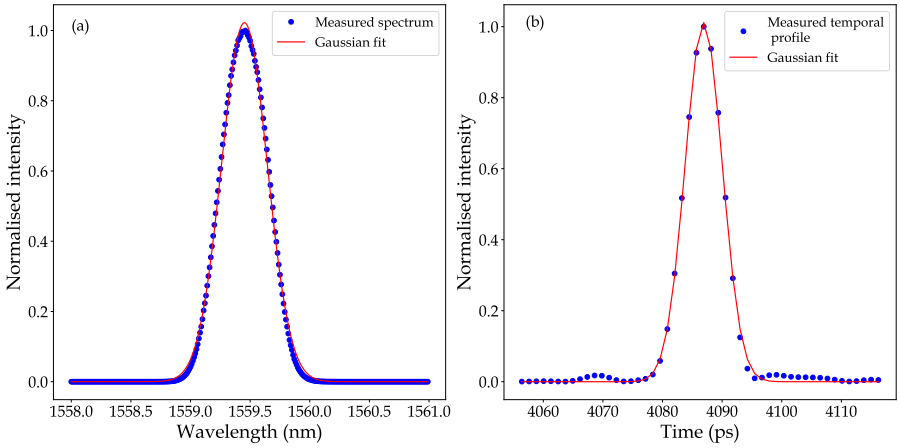

Figure 3.16: Measured spectral (a) and temporal (b) profiles of the input optical pulse.

3.8 Simulation of Fourier transform chronometry

The theoretical simulation of pulse duration measurement was done using experimental input spectra, shown in Figure 3.16(a). As it is seen in the optical setup, this input optical pulse in spectrum, $E(\omega)$, propagates through several dispersive elements consist of PM fibers, the modulator and the calcite wedges that result in slight broadening of the optical pulse. In the simulation, a dispersion corresponding to about 10 meters of single mode fiber is applied to the optical pulse as

$$E_{\mathrm{D}}(\omega) = E(\omega) \exp\left[-i\Phi_{\mathrm{GDD}}\frac{\omega^2}{2}\right] \tag{3.11}$$

where Φ_{GDD} is the group delay dispersion that is defined by $\Phi_{\mathrm{GDD}} = \beta_2 z$. And β_2 is the group velocity dispersion (GVD) coefficient that is equal to about $\beta_2 = -21.7 ps^2/km$ for single mode fiber. The next step of the simulation is to apply temporal phase profile to the dispersed optical pulse, $E_{\mathrm{D}}(\omega)$. For this purpose, the experimentally determined temporal phase profile (retrieved by direct electro-optic sampling technique as discussed in section 2.6) is multiplied with the optical pulse in temporal domain. By taking the Fourier transform of the optical pulse in the spectrum, $E_{\mathrm{D}}(\omega)$, the optical pulse in temporal domain is obtained as

$$\tilde{E}_{\mathrm{D}}(t) = \mathcal{F}\{E_{\mathrm{D}}(\omega)\}, \tag{3.12}$$

The optical pulse after temporal phase modulation is defined as

$$E_{\mathrm{PM}}(t) = \tilde{E}_{\mathrm{D}}(t) \exp\left[i\phi(t - t_0)\right], \tag{3.13}$$

where $\phi(t - t_0)$ is the applied phase profile in which t_0 is determined in a way to synchronize the linear region of the RF modulating signal to the optical pulse. This linear temporal phase leads to spectral shift in the spectral shift as discussed earlier. To simulate the tunable spectral shearing procedure, one needs to vary the slope of the applied linear temporal phase that is done by multiplying a factor, n, to the phase term. This factor is changed in uniform steps between 0 and 1 to act as a phase shifter. So by modifying Equation 4.16, the temporal phase is varied to get the tunable spectral shift as

$$E^n_{\mathrm{PM}}(t) = \tilde{E}_{\mathrm{D}}(t) \exp\left[i\ n\ \phi(t - t_0)\right] \tag{3.14}$$

The next step of the simulation is to get the interference signal while the spectral shift is varied, in the test arm of the interferometer $E^n_{\mathrm{PM}}(t)$, to scan the optical pulse with respect to its replica, in the reference arm of the interferometer $\tilde{E}_{\mathrm{D}}(t)$. By adding the two optical pulses from both arms of the interferometer, the interference signal at the output of the interferometer is expressed as

$$E^n_{\text{total}}(t) = \tilde{E}_{\text{D}}(t) + E^n_{\text{PM}}(t) \tag{3.15}$$

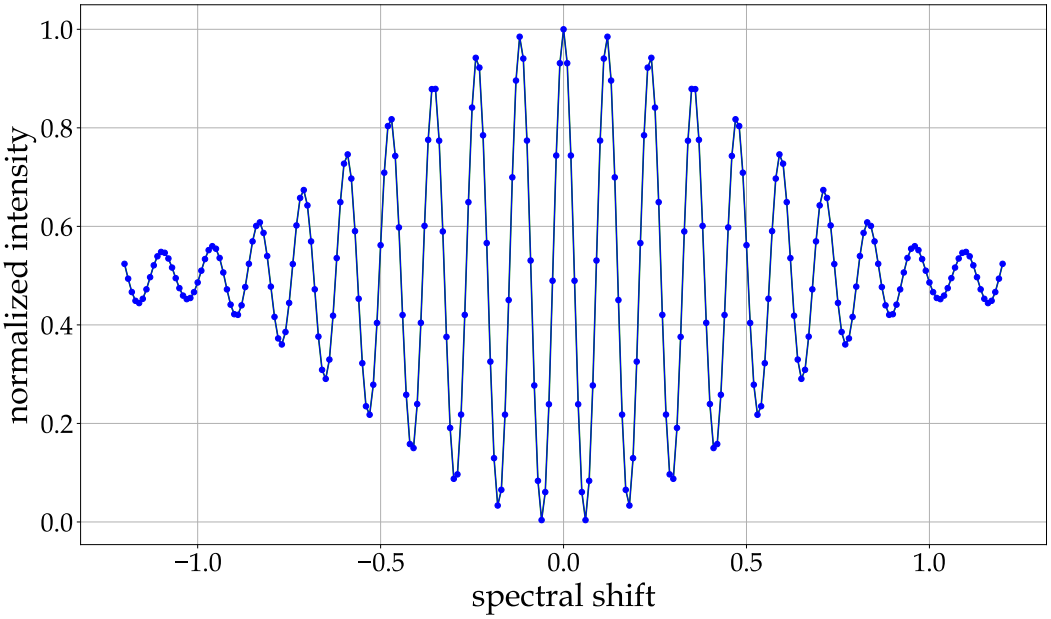

Figure 3.17: Simulation of interference signal as a function of spectral shift

Finally, the intensity profile of the pulse is calculated as

$$I^n(t) = |E^n_{\text{total}}(t)|^2 \tag{3.16}$$

The interference signal as a function of spectral shift as illustrated in Figure 3.17. Now, by taking Fourier transform of the interference signal, the intensity profile of the pulse in the temporal domain is achieved as shown in Figure 3.18. The temporal pulse width is calculated based on second-moment method as presented in subsection 1.2.1.

The simulation is repeated over a range of input bandwidth (measured input spectrum) to compare the trend of temporal width changes with experimental measurements as shown by red points in Figure 3.15. In this figure, the red shaded area shows the variation of temporal pulse width for up to 10 percent error in the applied spectral shift. This difference between the measured temporal width and the theoretical expectations may come from the optical pulse distortion when the spectral shear is applied. This distortion is seen in Figure 3.8 where the optical pulse with maximum shift (red) is distorted respect to the input optical pulse without spectral shift (blue). This error was considered in the simulation as indicated in Figure 3.15 where the red shaded area shows the variation of temporal pulse width for up to 10 percent error in the applied spectral shift.

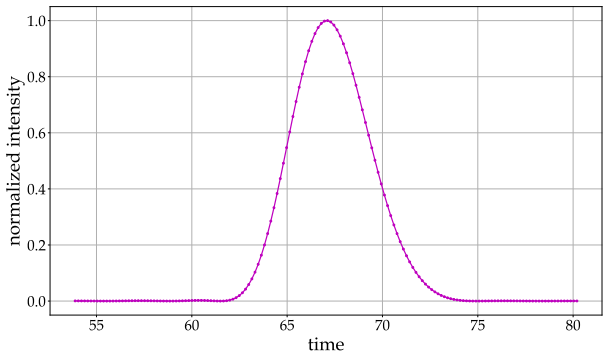

Figure 3.18: Energy envelope of the simulated optical pulse in temporal domain

3.9 Measuring temporal duration of the dispersed optical pulse

In order to verify the validity of this electro-optic method to measure the temporal profile of the short optical pulses, the impact of adding dispersion to the optical pulse is investigated. In this approach, the same spectral bandwidth of the optical pulse is sent through specific length of optical fiber which leads to pulse broadening in temporal domain without change in spectral domain. This increase in temporal width should be correspond to the amount of added dispersion. The Figure 3.19 shows the effect of adding different lengths of optical fiber on temporal width of the optical pulse.

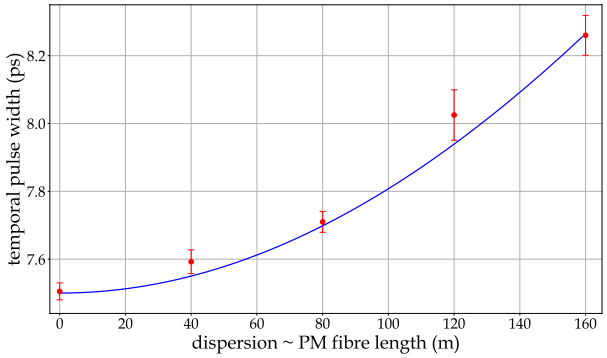

Figure 3.19: Impact of dispersion on temporal width of the optical pulse

This measurement was performed for different lengths of optical fibers added in the optical setup. The optical fibers were added in the optical setup just before the interferometer. Note that we used PM fibers as dispersive medium instead of single mode fiber (SMF). The PM fibers improve stability of the measurement. Since the

polarization-based interferometer has been used in this experiment, it helps to keep polarization state of the optical pulse unchanged at the input of the interferometer. This measurement was done for three cases by adding 40 m, 80 m, 120 m and 160 m of the PM fibers in the setup. Each case was repeated four times in order to investigate error in measuring the temporal width of the optical pulse.

As shown in Figure 3.19, result indicates that adding dispersion leads to increase in temporal width of the optical pulse. This increase should follow nonlinear trend for small amount of dispersion (it is nonlinear for dispersion corresponding to less than about 1 km of SMF). Considering the formula of the optical pulse broadening passing through the dispersive medium as

$$T(z) = T_0\sqrt{1 + (\frac{z}{L_D})^2} \tag{3.17}$$

The temporal width at given point, z, after propagating along optical fiber [23] is calculated. In this formula, $L_D = \frac{T_0^2}{|\beta_2|}$ is dispersion length where β_2 is group velocity dispersion and T_0 is initial temporal duration of the optical pulse. In this calculation, the initial temporal width of the optical pulse was taken equal to 7.48 ps (the measured temporal width without added dispersion). The measured temporal widths after adding PM fiber (dispersion) in the setup are consistent with the theoretical model. Note that no fitting has been done in the theoretical calculation.

3.10 Measuring temporal duration of the heralded single photon pulse

To generate single photons, the optical pulses (central wavelength of 1560 nm) from an erbium femtosecond oscillator (Menlo Systems C-Fiber HP, repetition rate of 80 MHz) are frequency-doubled by the built-in second harmonic generation module of the Menlo Systems. The up converted optical pulses are spectrally filtered and directed into a bulk 10 mm long periodically poled potassium titanyl phosphate (PPKTP) nonlinear crystal where photon pairs through a type-II collinear spontaneous parametric down-conversion process are generated [49]. I used the single photon source that was built by Michał Mikołajczyk and connected it as input source to the optical setup, Figure 3.9, that I built to measure temporal duration of classical light pulses. As mentioned in section 1.9, for preparing pure single photons, I adjusted the spectral bandwidth of the pump beam, 1.7 nm, of the single photon source in a way to get uncorrelated photon pairs. In addition, spectral filtering also was done to get narrowband, 0.5 nm, single photon pulses. The optical setup for measuring temporal duration of quantum light pulses is illustrated in Figure 3.20 in which the

orthogonally polarized photon pairs are coupled into a single mode polarization maintaining fiber and split using a fiber beam splitter. One photon is sent into the 4-f spectral filter where its bandwidth is limited to 0.5 nm and then goes through the polarization-based Mach-Zehnder interferometer. The other photon is directed straight to a single photon detector to act as a heralding photon. Both photons are detected with niobium nitride superconducting nanowire single photon detectors (SNSPDs, Single Quantum) and time-tagged for time-resolved coincidence counting using a Swabian Instruments Time Tagger Ultra.

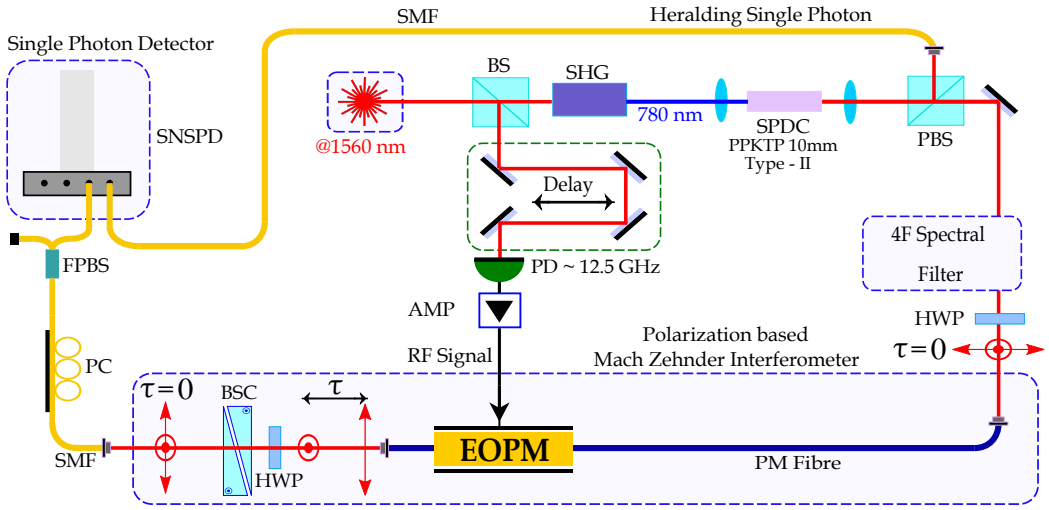

Figure 3.20: Interferometric optical setup for quantum single photon measurement. BS : beam splitter, SHG : second harmonic generation, SPDC : spontaneous parametric down conversion, HWP : half wave plate, PBS : polarizing beam splitter, PD : photodiode, AMP : amplifier, EOPM : electro-optic phase modulator, PM fiber : polarization maintaining fiber, SMF : single mode fiber, BSC : Babinet–Soleil compensator, PC : polarization controller, FPBS : fiber polarizing beam splitter, SNSPD : niobium nitride superconducting nanowire single photon detectors.

For the single photon experiment, quantum pulsed light with spectral bandwidth in the range of 0.5 nm was prepared. The Figure 3.21 shows the measured coincidences as a function of spectral shear. For this experiment, the number of coincidences was measured over a coincidence window of 10 ns to count photons in a period less than the repetition rate (12.5 ns) of the pulsed laser. Preparing the input bandwidth of 0.5 nm required a significant amount of spectral filtering that significantly decreased the number of coincidences, so an acquisition time of 12 seconds per data point was used for photon counting. In order to acquire the temporal energy envelope of the single photon pulse, the Fourier transform of the interference fringes was taken and

the temporal envelope of the single photon is shown in Figure 3.22.

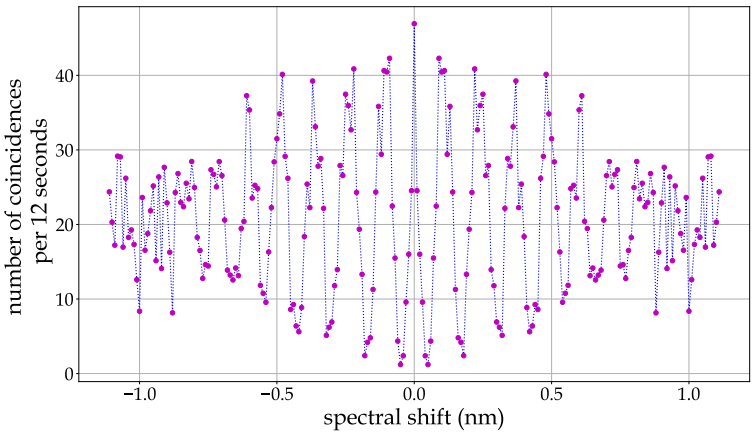

Figure 3.21: Fringe pattern resulting from single photon coincidences versus spectral shift (negative side is the mirror of positive side). The blue line is used to guide the eye.

From the temporal profile, we calculate a temporal width of 7.50 $\pm$ 0.04 ps for the single photon which is close to the measured temporal width of the classical optical pulse. The measurement was done for a range of input bandwidths to see the temporal width change of the single-photon pulse. The blue points in Figure 3.15 indicate the decrease in temporal duration of the single-photon pulse while the input spectral bandwidth is increased. This trend matches with results of the classical measurement as shown by green points in Figure 3.15.

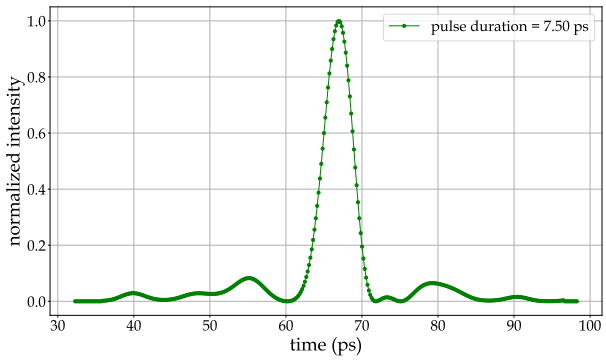

Figure 3.22: Energy envelope of the measured single photon pulse in temporal domain

3.11 Experimental limitations

In the experiment, we considered an optical pulse with 0.5 nm bandwidth. This bandwidth is limited by linear region of the electronic signal from the fast photodiode. Choosing a narrower bandwidth (larger temporal width) would result in pulse distortion so that the optical pulse will be affected by the nonlinear region of the electronic signal. There is also limitation for taking broader bandwidth as it requires a larger spectral shear. Since the total spectral shear of 1.22 nm can only be applied by our optical system, we do not take a broader optical bandwidth for the input optical pulse. To achieve more spectral shear, one can either apply larger temporal phase amplitude to modulate the optical pulse or use a EOPM with lower half-wave voltage.

The main limiting factor in quantum regime experiment is small number of single photon counts that is due to spectral filtering to reach the target bandwidth of 0.5 nm. This can be improved by using a longer nonlinear crystal in the single photon source that could generate photon pairs with narrower spectral bandwidth [73]. This would require less spectral filtering that results in more singe photon counts.

3.12 Chapter summary

The energy envelope of the ultrashort classical and quantum light pulse was measured using tunable electro-optic spectral shearing interferometry technique. I measured the temporal width of the optical pulse that is in agreement with theoretical expectation. Validity of the technique was confirmed by investigating the effect of added dispersion into the optical pulse. By keeping the same input spectral bandwidth, temporal width was measured for different lengths of dispersive medium added to the setup. The measured temporal width after adding dispersion shows temporal broadening in agreement with the theoretical model.

This technique does not require nonlinear interaction that makes it applicable for measuring single photon pulses. And it only employs a photodiode to record interference signal whereas other techniques like SPIDER and FROG rely on spectrometer. Not requiring a spectrometer is potentially advantageous for single-photon signals, as well as in exotic spectral regions, where high-resolution spectrometers are not easily available.

Chapter 4

Dispersion engineering for time-frequency transformation

In the second chapter, an active approach for optical pulse shaping and measurement of optical pulses based on electro-optic phase modulation was introduced where the optical pulse spectrally was modified through quadratic and linear temporal phase modulation process. In the current chapter, a passive optical device for temporal shaping of optical pulse is presented based on fiber Bragg grating structures. These structures will be designed in a way to engineer dispersion profile of a propagating optical pulse and temporally and spectrally shape it. The research work presented in this chapter was done in the framework of scientific collaboration between Quantum Photonics Lab at the University of Warsaw and Optoelectronic Research Centre (ORC) at the University of Southampton. I did two research visits at Southampton. In my first visit, I was trained to fabricate fiber Bragg grating structures and I also made optical setup based on optical frequency domain reflectometry to characterize the fabricated grating samples. Then, in my second visit, I fabricated several samples with different spectral and temporal specifications.

4.1 Introduction

In recent years, there have been significant efforts to realise miniaturization of large free-space optical setups into a small optical circuits. There is an ongoing research to find a suitable platform for photonic waveguides. Silica based waveguides [74] have been one of the promising platforms for integrated photonics due to their low loss over a large spectrum from ultra violet to the near infra-red and also its well established fabrication process. In addition, silica waveguides in the form of interferometric configuration have been developed to create functionalities that are required for optical information processing. The other interesting platform is based

on lithium niobate [75, 76] material that due to its intrinsic high non-linear response offers functionalities such as frequency conversion of optical signals. Furthermore, semiconductor based platforms such as Silicon and Indium Phosphide [77, 78] have also been considered as good candidates for integrated photonics due to their integration compatibility with available detectors and sources in these platforms. These platforms offer high stability, reliability and compatibility with optical fiber networks [79]. These materials have high refractive index that produce narrow waveguides with large confinement factor. However, this results in a small mode diameter that makes a huge mismatch when are coupled into optical fiber. This mismatch leads to a significant loss when coupling into and out of the waveguides. For example, the mode size for a standard optical fiber (SMF-28) is about two orders of magnitude larger compared to a typical silicon waveguides [80]. Considering this coupling issue and also high intrinsic loss of most of these platforms around telecommunication wavelength of 1550 nm, developing photonic elements by optical fibers with special functionalities can be an operational solution as the optical fiber is the best optical data carrier for long distance transmission link in both classical and quantum applications.

By discovery of photosensitivity of fiber-optic, a new capabilities to make fiber-optic based photonic devices were identified [81]. This discovery made it possible to modify refractive index profile of an optical fiber to achieve interesting functionalities of the optical fiber. By performing such a modification in the core of the optical fiber, Bragg grating structures can be made for telecommunication and sensing applications. One important application that is the main goal of this chapter is to make chirped grating structures for dispersion compensation and optical pulse shaping. By placing the Bragg gratings inside the fiber-optic and controlling the period and refractive index profile of such a grating structures in the space domain, one can engineer a desired spectral response of the grating structure. This capability has opened a way to make basic elements such as spectral filters, mirrors and laser cavities. Furthermore, Fiber Bragg Gratings (FBG)s have found application in sensing to detect environmental effects like strain and temperature in which such effects can change the period and refractive index of the FBG.

In this chapter, fabrication procedure of linear chirped FBG structures will be presented and then the fabricated samples will be characterized by building optical frequency domain reflectometry setup. Furthermore, other characterization techniques will be considered to validate the spectral and temporal response of the fabricated samples. Finally, I will discuss designing non-linear chirped FBG that can compensate a non-linear dispersion profile.

4.2 Modelling of fiber Bragg grating structures

FBGs are structures with periodic change of refractive index in the fiber core. This refractive index modulation acts like a selective mirror for the wavelength that satisfies the Bragg condition. Such structures function similar as dielectric mirrors in which an alternating sequence of layers of two different optical materials are used to reflect a specific wavelength based on the Bragg condition.

A similar effect can be implemented in the fiber core by modifying its refractive index to make grating structures inside the optical fiber as shown in Figure 4.1. In this case, an incident wave to the structure will either be reflected or be transmitted through the structure. The structure of refractive index modulation can be engineered in a way to selectively reflect specific wavelengths of the incident wave.

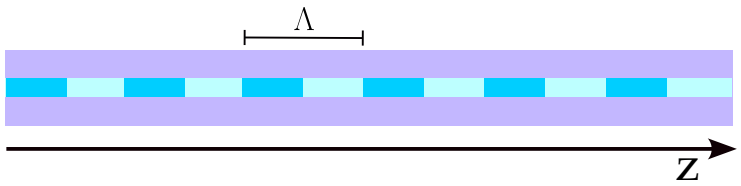

Figure 4.1: Schematic representation of FBG structure.

For the Bragg grating structure with grating period of Λ, the grating's wave vector is defined in Equation 4.1 that gives the Bragg condition in Equation 4.2 in which λ_{Bragg} is the central wavelength of the reflected light, and n is the effective refractive index of the fiber core.

$$k_{grating} = \frac{2\pi}{\Lambda} \tag{4.1}$$

$$\lambda_{Bragg} = 2n\Lambda \tag{4.2}$$

By designing the grating's period and length, together with the strength of the refractive index modulation inside the fiber core, one can control reflectivity level and shape of the grating over a specific range of wavelengths. These parameters have been indicated in Figure 4.2, where z is the axis along the fiber length that optical wave propagates. This figure illustrates the dependency of the effective refractive index of the fiber as a function of the distance z along the grating. The optical fiber has an initial refractive index, n_0, before grating fabrication but it has a higher average refractive index, n_{avg}, after fabrication process.

In Figure 4.2 (b), the $\Delta n_{dc}(z)$ is the average refractive index change ('dc' offset) and the $\Delta n_{ac}(x, y)$ is the maximum value of refractive index change (modulation depth).

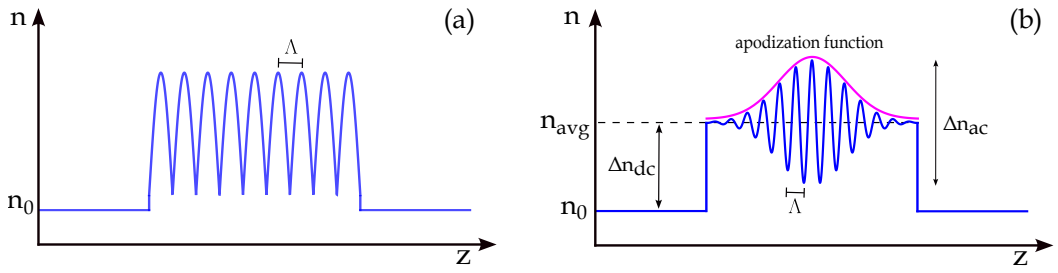

Figure 4.2: Refractive index profile along the fiber length. (a) Uniform index modulation of FBG and (b) Apodized index modulation of FBG.

For a Bragg grating structure with a periodic z-dependent perturbation, the refractive index modulation at the given position along the fiber core is given as [46, 82, 83]

$$\Delta n(x,y,z) = \Delta n_{dc}(z) + \Delta n_{ac}(x,y) f(z) \cos\left[\frac{2\pi}{\Lambda} z + \phi(z)\right] \tag{4.3}$$

where $f(z)$ is the grating apodization profile, Λ is the Bragg grating period and the $\phi(z)$ is value of the phase shift in the grating.

By modifying these parameters, one can design a grating structure with different functionalities to temporally and spectrally shape an incident optical wave. In this thesis, our focus will be on designing chirped FBG structures with different bandwidth and dispersion features at different operational wavelengths. In Figure 4.3, general characteristics of a linearly chirped FBG structure are shown. The chirped grating is deigned for a given central wavelength and spectral bandwidth $\Delta\lambda_{chirp}$ that these parameters define the central Bragg period Λ_0, the shortest Bragg period Λ_{short}, and the longest Bragg period Λ_{long}.

$$\Delta\lambda_{chirp} = (\lambda_{long} - \lambda_{short}) = 2n_{eff}\Delta\Lambda_{chirp} \tag{4.4}$$

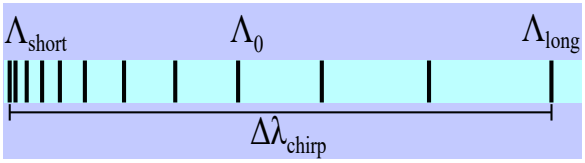

Figure 4.3: Characteristics of chirped gratings

By linearly changing the Bragg period, one can locate Bragg mirrors in the fiber core to reflect a range of wavelengths.

4.2.1 Reflectivity response of chirp fiber Bragg gratings

Response of the grating in the spectral domain can be engineered by modifying the mentioned parameters in the spatial domain over the fiber length.

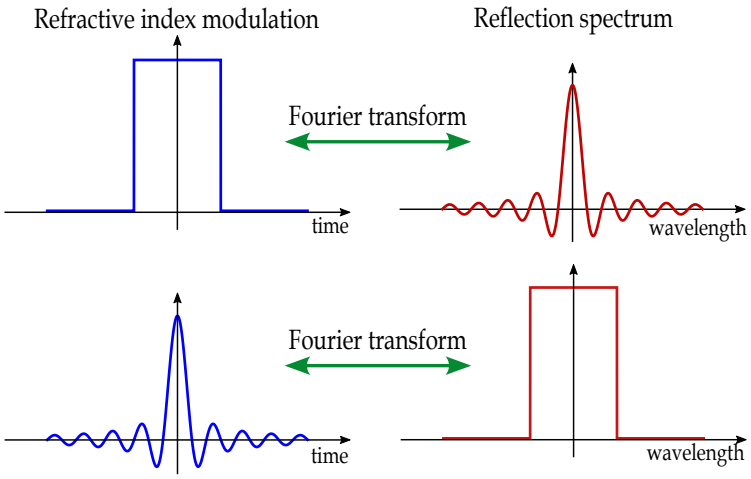

Figure 4.4: Reflection spectrum and refractive index modulation in chirp fiber Bragg gratings

After defining the Bragg period change to achieve target spectral bandwidth of the chirped grating, the next step is to define the shape of the reflectivity profile in the spectrum. By controlling the strength of the refractive index modulation at the given points over the fiber core along with the length of the grating, one can engineer the spectral bandwidth and reflectance of the grating. This can be a complex non-linear relationship, but for weak gratings, those with no saturation effects, the spectral profile is the Fourier transform of the apodization function. The apodization function can be considered as the envelope function of the grating as indicated in Figure 4.2 that defines the shape of the spectral response of the grating [84]. The ideal linear chirped grating has a reflection spectral profile like a rectangular shape that filters a range wavelengths. To get such a reflection spectrum, one needs to apply an apodization profile like a Sinc function, as depicted in Figure 4.4, when refractive index modulation is performed during the UV-writing process. However, in practice, applying such a complicated apodization profile is a challenge as it requires a longer UV-writing process. In this regard, having a constant output power of the argon-ion laser for a long period is one of the main issues. In this thesis, an apodization profile of super gaussian and Hyperbolic tangent functions were considered to be applied as refractive index modulation profile during the UV-writing process. The super gaussian profile has simpler shape and its Fourier transformation gives the closest shape to the rectangular shape.

4.3 Direct UV writing of fiber Bragg gratings

Inscription of fiber Bragg gratings by direct UV writing refers to fabrication technique in which the refractive index of medium is modified by exposure to UV light. In this technique photosensitive glass is used as a medium and placed under the exposure of UV light. By controlling the intensity and exposure time of the UV light, the medium absorbs the UV light and its refractive index changes. In this thesis, this technique is employed for inscription of Bragg grating structures in the fiber core. The direct UV writing technique has been well-developed at the Optoelectronic Research Centre of the University of Southampton, where all of the FBG samples, presented in this thesis, have been fabricated.

In this work, optical fiber are loaded by hydrogen or deuterium, or germanium in order to make them photosensitive. Then the loaded optical fiber is used for inscription of Bragg grating structures.

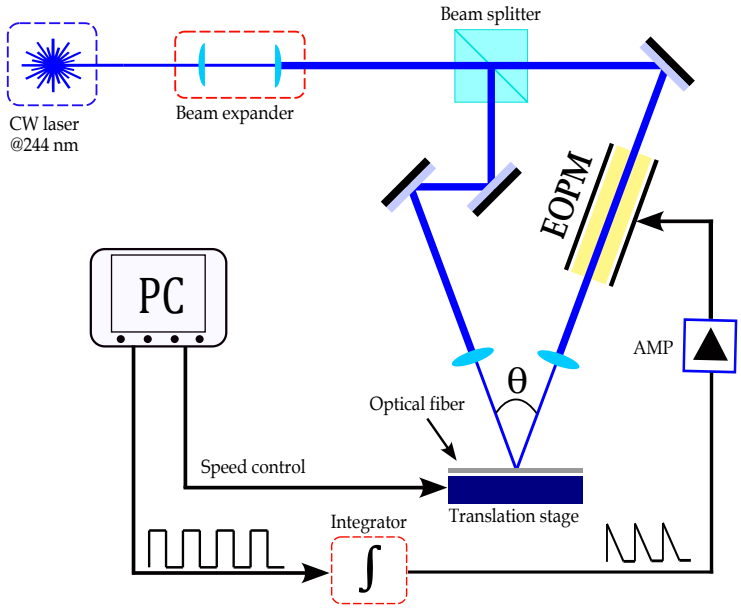

Figure 4.5: Optical interferometric setup for UV writing of fiber Bragg grating structures

The optical setup used for UV writing is based on holographic approach [85] in which a beam splitter is used to divide a single input UV beam into two beams and then brought to be interfered at the fiber core as illustrated in Figure 4.5. These two beams come together at a mutual angle of θ, by adjusting reflections from two UV mirrors. This method allows the Bragg wavelength to be chosen independently of the UV wavelength as [86]

$$\lambda_{Bragg} = \frac{n_{eff}\lambda_{uv}}{n_{uv}\sin\left(\frac{\theta}{2}\right)}, \tag{4.5}$$

where λ_{Bragg} is the Bragg wavelength, n_{eff} is the effective refractive index of the fiber, n_{uv} is the refractive index of silica in the UV, λ_{uv} is the wavelength of the UV light, and θ is the mutual angle of the interfering UV beams.

In the experimental setup, a continuous wave argon-ion laser source at wavelength of 244 nm was used that delivers an optical power of about 50 mW. The UV light beam is expanded to about 10 mm to assist with alignment and focusing of the beam and also to avoid damage of the optical components. A beam splitter is used to split the expanded beam into two arms of the interferometer. A free-space electro-optic phase modulator (EOPM) is placed in one arm of the interferometer and then both beams are focused at the same spot in the fiber core where overlap to create an interference pattern. By modulating the EOPM, the phase of the optical beam in that arm of the interferometer is modified to make a constructive or destructive interference at the focus spot. In Figure 4.6, routes of the beams are indicated with blue lines that are passing through a pin-hole, with $1\mu m$ diameter, where the fiber core will be placed.

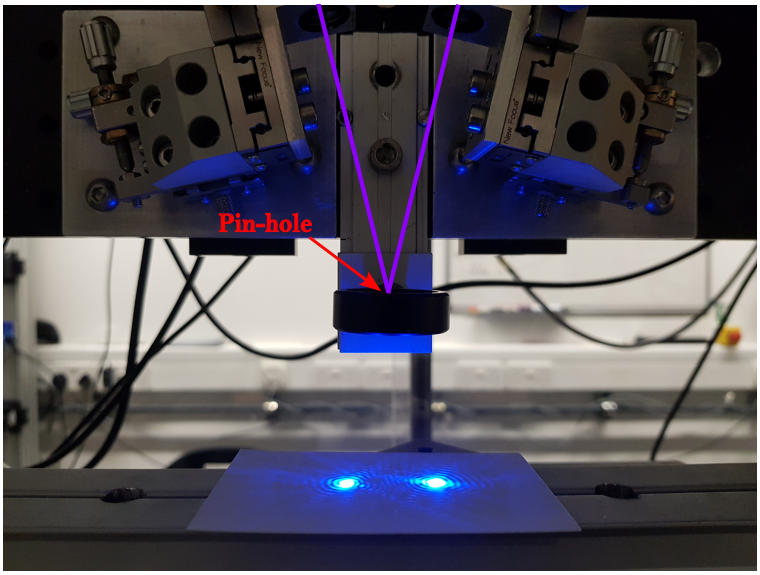

Figure 4.6: Interference pattern of two UV light beams coming from arms of the interferometer. Photo was taken at UV-Writing Lab at the Optoelectronic Research Centre, University of Southampton.

After aligning the beam routes to get the interference pattern, the next step is to put the optical fiber in the location of the pin-hole. The optical fiber is placed on a sub-nanometer-precision air-bearing translation stage, AEROTECH BLM linear

motors high-performance air-bearing system - Model MT240P, that is controlled by a software unit, AEROTECH A3200 Motion Composer. This stage allows for high-precision positioning the fiber core on the interference spot. By moving the stage to the predefined positions, one can locate Bragg gratings in desired location inside the fiber core. Simultaneously, the EOPM can modify the phase in one arm of the interferometr to control applied UV light. The constructive interference at the fiber core leads to more absorption of UV light and consequently more change of refractive index at the given point in the fiber core. The driving voltage applied to the EOPM modifies the intensity of the UV light at the fiber core and therefore it controls the strength of the refractive index modulation over the length of the fiber core.

The optical setup for UV-writing was already built at ORC and I used the programming code to control the translating stage that also has been developed at ORC. For writing every grating sample, I aligned the UV-writing optical setup to get interference pattern and the alignment needs to be checked continuously due to instability of the argon laser source.

4.3.1 Preparing and alignment of optical fiber for UV-writing

Photosensitivity of standard single mode fiber, e.g. SMF-28, is not enough for inscription of Bragg grating. To enhance the photosensitivity of the optical fiber, hydrogen loading is used to sensitise optical fiber with low germanium content [87]. This is done by keeping the optical fiber in hydrogen cell under the high-pressure (between tens to hundreds of bars). For a hydrogen loaded single mode fiber, UV irradiation of the fiber core can lead to increase of refractive index by 0.011 [88]. After taking the pressure off, the hydrogen stays in the fiber for up to a few hours at room temperature and then goes out of the fiber. To avoid degassing the Hydrogen, the optical fiber is kept in nitrogen cell.

To prepare the hydrogen loaded optical fiber for UV-writing, its coating needs to be removed. For smooth removing of the coating, the optical fiber is soaked in acetone for about 15 minutes. Now, it is ready to be mounted on the translation stage. Two sides of the optical fiber is placed on fiber clamps and then a tension of about 0.3 N is applied to make it straight for alignment.

After mounting the optical fiber on the translation stage, the next step is to place the interference spot on the fiber core. The optical fiber should be aligned in X, Y and Z directions so that the interference spot remains on the fiber core over the whole length of the grating while stage is moving to inscribe the Bragg gratings. After alignment, coordinates of the initial point of the grating and also several points in the fiber core is registered in the translation stage's software to be used for movement of the stage during the UV-writing process.

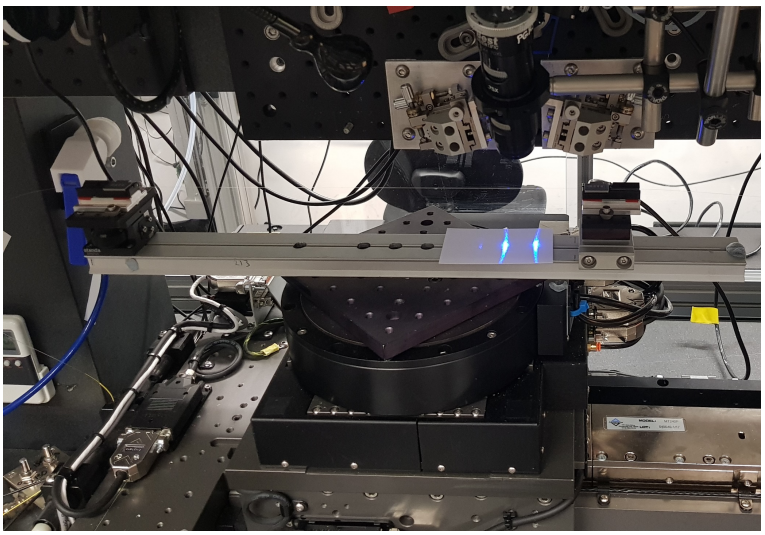

Figure 4.7: Placement of the optical fiber under interference spot of UV light beams. Photo has taken at UV-Writing Lab at the Optoelectronic Research Centre, University of Southampton.

4.3.2 UV-writing process

Considering the optical fiber has been aligned and its positioning registered in the controlling software of the optical setup, the UV-writing process is ready to be initiated. This process is controlled by G-code program, computer numerical control (CNC) programming language, to automate the UV-writing process, developed at ORC. This code controls the movement of the translation stage and the electro-optic phase modulation simultaneously that allows controlling of the Bragg period at predefined locations and apodization profile over the length of the optical fiber. The G-code program generates a rectangular waveform that is fed into an electronic integrator to produce the saw-tooth signal that is then used to drive the modulator via a high voltage amplifier [89]. Whole this process is presented in Figure 4.5.

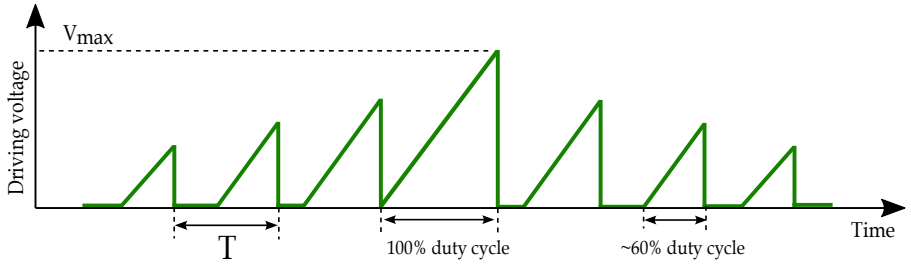

Figure 4.8: Schematic of the sawtooth waveform to drive the EOPM [89]. T: grating period.

The saw-tooth signal determines the local modulation contrast, Δn_{ac}, over each grating period as depicted in Figure 4.8. By controlling the duty cycle at each grating period, one can modify the refractive index change at the given location on the fiber core. A duty cycle of 100 % provides the strongest refractive index change. In this way, the predefined apodization profile is applied over the spatial domain in the fiber core that defines the desired reflection profile in the spectral domain.

In addition, movement speed of the translation stage is also defined in the G-code program to control the applied energy density in the fiber core, also known as the fluence. By defining the speed, Bragg period, duty cycle and power of the laser in the G-code program, one can control the UV-writing process.

4.4 Characterization setup for measuring reflectivity of the grating structures

After writing a FBG, the first task is to check spectral reflection profile of the grating. In Figure 4.9 the optical setup configuration used for characterization of grating structure is shown. A broadband laser source is connected to a 2x2 fiber coupler, 50:50 beam splitter, in which one of the output arms is terminated using refractive index matching gel while the other output is connected to the device under test (DUT). The reflected signal from the DUT comes back into the beam splitter and then proceeds into an optical spectrum analyzer. Note that the end of the DUT is also terminated to avoid reflection from fiber facet.

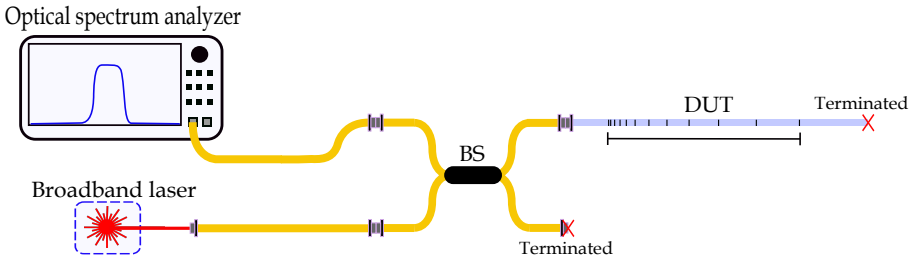

Figure 4.9: Characterization setup for measuring reflectivity of the grating structures. BS: beam splitter, DUT: device under test.

This measurement gives the spectral profile of the DUT. To obtain the reflectivity, one needs to calibrate the reflection spectrum respect to a known reference reflectivity. A useful reference is the 3.5 % Fresnel reflection from the cleaved far end of the fiber to calibrate the actual reflection from the grating [86]. This is done by disconnecting the DUT and measuring spectral reflection from the FC ferrule connector of the fiber

coupler. The reflection spectrum from this flat fiber facet, the Fresnel reflection, is considered as a reference reflectivity [84].

4.5 Fabrication of chirped fiber Bragg grating

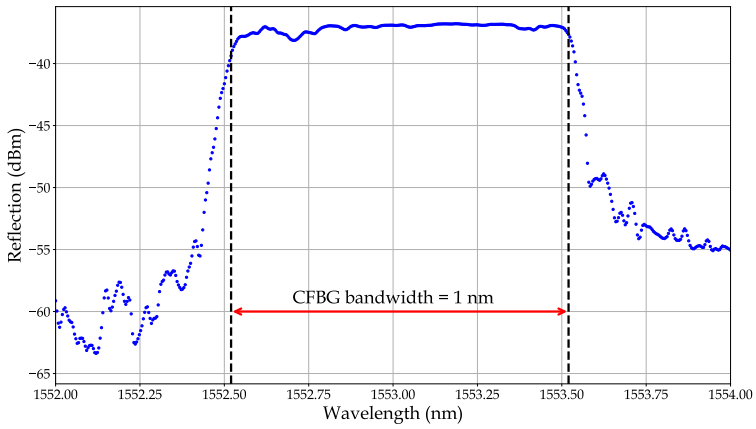

Figure 4.10: Reflection profile of chirped FBG with 1 nm bandwidth designed at 1550 nm

The grating was designed for the central wavelength of 1550 nm, while the spectral reflectivity of the grating shows a different central wavelength for the sample. This is due to the applied tension to the fiber during UV-writing process. To use the sample at exact designed wavelength, one needs to apply similar tension to the sample to get designed spectral response.

4.6 Phase and temporal response of Bragg grating structures

In section 4.4, the characterization technique of the grating structures was presented that only gives information about spectral response of the grating. To obtain information about refractive index change and phase transfer function over length of a grating structure, the interferometric of Optical Frequency Domain Reflectometry (OFDR) is used.

4.6.1 Characterization of grating structures by optical frequency domain reflectometry (OFDR)

The OFDR technique works in the frequency domain and uses tunable continuous wave laser source as a local oscillator to swept over a certain wavelength band. Backreflections from the Device Under Test (DUT) beat with the local oscillator, and are detected by a photodiode. The optical frequency of the local oscillator is swept so that reflections from points at different distances along the DUT correspond to different beat frequencies on the detector. By taking Fourier transform of the obtained reflections in the frequency domain, one can acquire the corresponding reflections in the time domain (different distances along the DUT). Depending on spectral range of the frequency sweeping, the OFDR measurement technique is able to give a sub-millimeter resolution over several tens of meters.

4.6.2 Configuration of the OFDR optical setup

Figure 4.11 shows the schematic of the OFDR optical setup that is comprised of a tunable laser source (TLS) and two fiber optic interferometers. The main interferometer does the measurement on the DUT and the auxiliary interferometer operates as trigger for data logging. The output of the TLS is split into a reference arm and a test arm where the DUT is placed. Note that the optical path lengths of the reference and test arms should be same. The interference between the beams coming from the reference arm and test arm is detected with a photodetector while the wavelength of the TLS is swept. Interference fringes are detected and related to the optical amplitude and phase response of the DUT. The collected interference fringes in the spectral domain can be processed using the Fourier transform into the time domain. So in the time domain, reflections as a function of spatial position along the DUT can be reconstructed.

In the actual optical setup, that I built at Optoelectronic Research Centre at the University of Southampton, an Agilent 8164B Lightwave Mainframe measurement system was employed that hosts an Agilent 81600B Tunable Laser Source (TLS), and three Agilent 81636B Fast Optical Power Sensor. This mainframe ensures simultaneous data logging at all plugged power meters and the tunable laser so that sweeping wavelength is registered and then the system waits until its corresponding power value at all power meters also gets registered. I developed a piece of Python code to communicate with all devices (TLS and power meters) and automate the experimental measurement and perform the data processing.

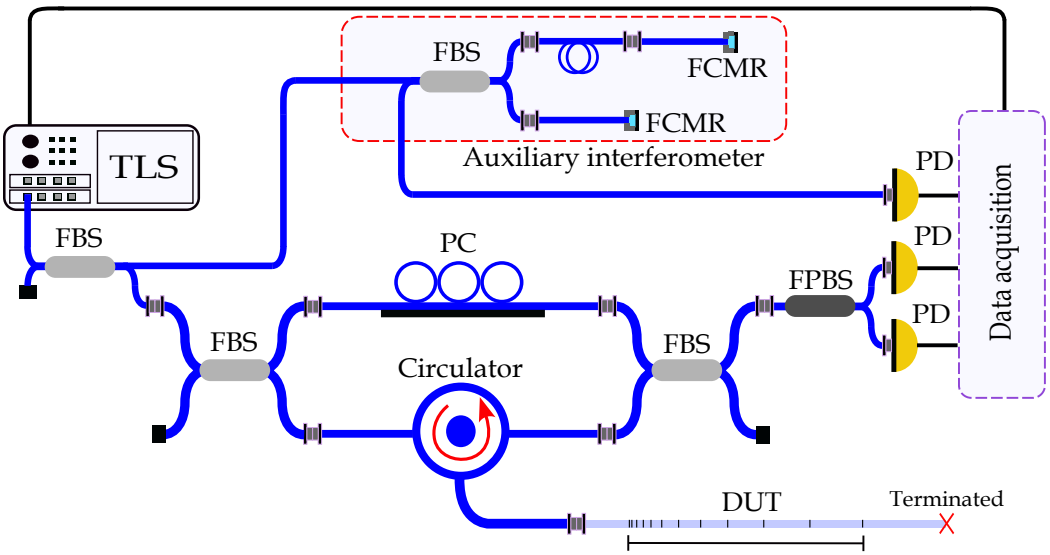

Figure 4.11: Configuration of optical setup of the optical frequency domain reflectometry. FBS: fiber beam splitter, DUT: device under test, TLS: tunable laser source, PC: polarization controller, FPBS: fiber polarization beam splitter, PD: photo-diode, FCMR: fiber-coupled mirror reflector.

4.6.3 Measurement procedure by the OFDR

In this section, temporal response of the sample, the chirped FBG sample presented in section 4.5, is characterized using the OFDR scheme. I developed a piece of Python code that controls the devices and collects the data and then it process the acquired data. Here I explain about the data collection procedure and then how data processing is done in the Python code. The tunable laser is scanned over 10 nm bandwidth around 1550 nm to acquire back reflections from different points in the DUT. The wavelength sweeping was done in continuous mode with steps of 10 pm at speed of 1 nm per second. In an ideal case, the scanning process should be linear to avoid noise in Fourier domain due to unequal spacing in frequency scanning. But in practice, the optical frequency sweep is not perfectly linear. To overcome this issue, we can monitor the instantaneous frequency, $\nu(t)$, during the measurement process so that we can then eliminate the error due to the nonlinear frequency sweeping. This is done by using an auxiliary interferometer with a fixed time delay, τ, between the two arms of the auxiliary interferometer to monitor the frequency sweep. In the experimental setup, a piece of optical fiber with length of 40 cm was placed in one arm of the auxiliary interferometer to introduce this time delay. Figure 4.12 illustrates steps to obtain the instantaneous frequency from the auxiliary interferometer.

The interference signal from the auxiliary interferometer is detected by a photodi-

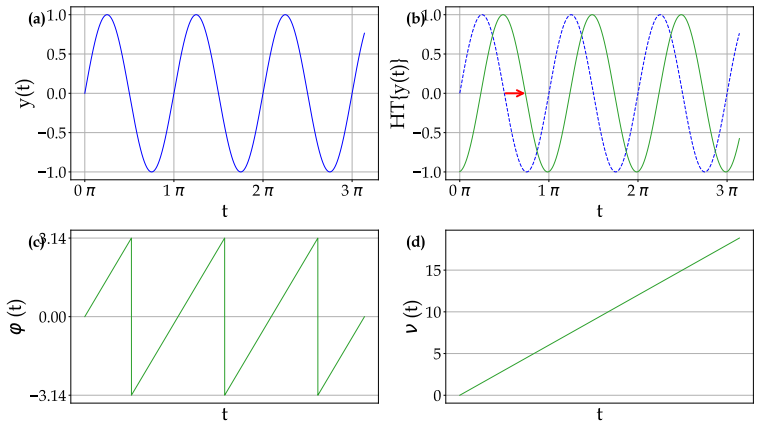

Figure 4.12: The procedure to acquire the instantaneous frequency from the auxiliary interferometer. Measured interference signal at the output of the auxiliary interferometer (a), Hilbert transform of the initial interference signal (b), wrapped phase acquired from auxiliary beating signal (c), instantaneous frequency (d).

ode. The measured intensity by the power sensor can be described as [90]

$$y(t) = A_0 \sin\left[2\pi\tau\nu(t) + \phi_0\right], \tag{4.6}$$

where the A_0 is the voltage amplitude and the ϕ_0 is the constant phase of an auxiliary beating signal. To achieve the phase argument of the interference signal, the Hilbert transformation can be used. The Hilbert transform $HT\{y(t)\}$ of the measured sinusoidal wave function $y(t)$ is same as the measured signal $y(t)$, except that the phase of the waveform is shifted by $\pi/2$. Therefore we have

$$HT\{y(t)\} = A_0 \cos\left[2\pi\tau\nu(t) + \phi_0\right]. \tag{4.7}$$

The phase $\phi(t)$ of the auxiliary beating signal with a single reflection point, reflection from mirror, can be obtained as

$$\phi(t) = 2\pi\tau\nu(t) + \phi_0 = \arctan\left[\frac{y(t)}{HT\{y(t)\}}\right], \tag{4.8}$$

and considering that the instantaneous frequency is defined as temporal derivative of the oscillation phase

$$\nu(t) = \frac{1}{2\pi}\frac{d\phi(t)}{dt}, \tag{4.9}$$

the instantaneous frequency can be achieved as

$$\nu(t) = \frac{1}{2\pi\tau}(\arctan[\frac{y(t)}{HT\{y(t)\}}] - \phi_0), \tag{4.10}$$

where τ is the optical path difference of the two arms of the auxiliary interferometer. For a path length difference of optical fiber, L, and refractive index of fiber core, n, the nonlinear swept frequency is obtain as

$$\nu(t) = \frac{1}{2\pi}\frac{c}{nL}(\arctan[\frac{y(t)}{HT\{y(t)\}}] - \phi_0). \tag{4.11}$$

This measured nonlinear frequency sweep by the auxiliary interferometer can be used along with data interpolation and resampling techniques to modify the step interval of the instantaneous frequency sweeping in the main interferometer to make equal step intervals. Therefore, this method can compensate degradation of spatial resolution when Fourier transformation is taken.

Figure 4.13 shows the Fourier transform of the beating signal with respect to the fiber length with nonlinear sweeping and after correction of non-linearty in frequency sweeping.

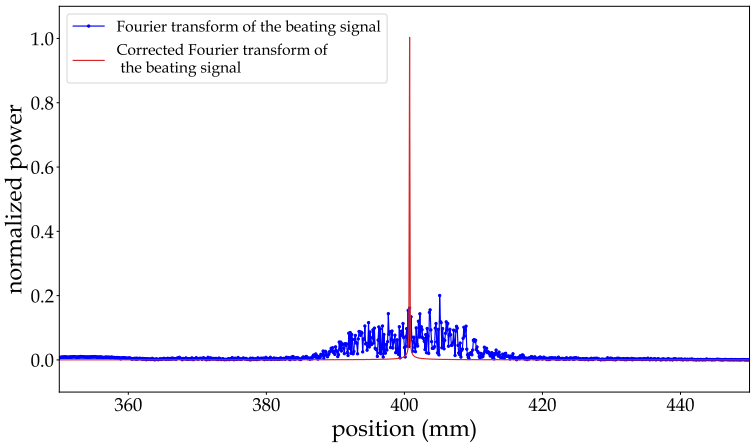

Figure 4.13: Fourier transform of the beating signal from the auxiliary interferometer as function of position along the optical fiber. Before (blue line) and after (red line) correcting the non-linearity of sweeping frequency.

As seen in Figure 4.13, after the correction, a clear resonance appears around 400 mm on the spatial domain of the optical fiber that indicates the position of the fiber-coupled mirror reflector (FCMR) and is matched with the introduced time delay added into one arm of the auxiliary interferometer.

The sample is placed in one arm of the main interferometer through an optical circulator as shown in Figure 4.11. While TLS is scanned over 10 nm aroun 1550 nm,

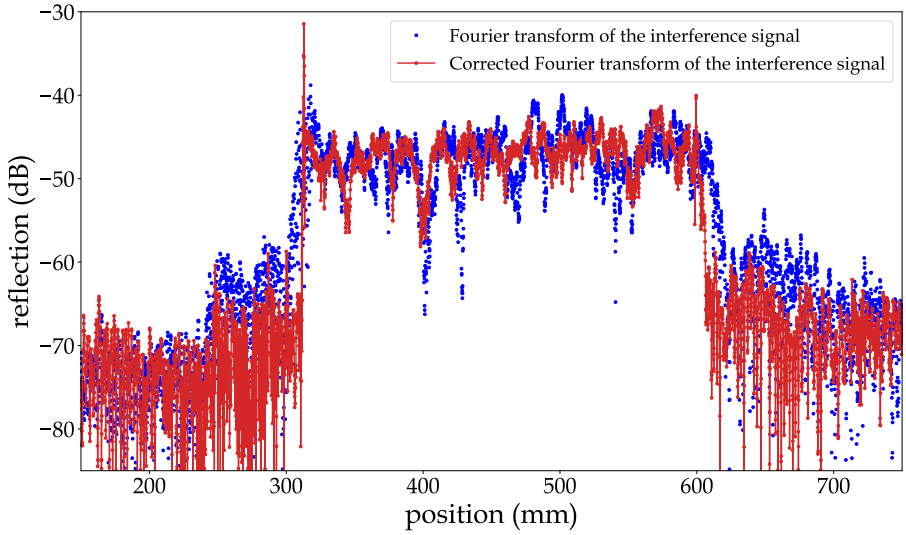

Figure 4.14: Fourier transform of the interference signal from the main interferometer as function of position along the optical fiber. Before (blue points) and after (red points) correcting the non-linearity of sweeping frequency.

the reflected beam from different points over the DUT is interfered with the reference beam. At the end, polarization states of the interference signal is split using a polarizing beam splitter (PBS) and then their intensity changes are recorded by two power sensors. A polarization controller is also placed in the other arm of the main interferometr to adjust the polarization of the light in the interferometer to get equal intensity for both polarization states. Intensity variations at all three power sensors are recorded simultaneously.

In the next step, the interference signal measured at the output of the main interferometer is analyzed. The corrected frequency sweep acquired by the auxiliary interferometer is used to re-sample the measured intensities at the output of the main interferometer. Summation of interference fringes associated to both polarization states gives the total interference signal from the chirped FBG. By taking the Fourier transform of the total interference signal and calculating its absolute value, the reflectivity of the grating is obtained.

So far the reflectivity of the chirped FBG as a function of the sweeping wavelength has achieved. The next step is to define the spatial domain corresponding to the spectral bandwidth of the grating. The measured data points acquired by frequency sweeping over the specific spectral range is corresponding to the spatial local Rayleigh backscattering signals from the DUT. The scanning range defines the spatial resolution in the Fourier domain and is given by [91]

$$dx = \frac{c}{2n\Delta\nu}, \tag{4.12}$$

where n is the refractive index of the fiber core and $\Delta\nu$ is the scanning spectral bandwidth. The refractive index equal to 1.444 was considered for the optical fiber. Note that the both forward and backward propagation of the optical beam in the DUT is considered to calculate the travel distance. The reflectivity of the chirped FBG presented in section 4.5 as function of the spatial domain is illustrated in Figure 4.14, in which reflectivity of the grating before (blue points) and after (red points) correcting the non-linearity in frequency sweeping is shown.

As promised earlier in the current section, the OFDR technique is able to give information about temporal response of the grating structures. To get the phase information of the grating, the phase angle of the Fourier transform needs to be calculated. After unwrapping the acquired data, the phase transfer function over the length of the grating is achieved. Finally, by taking the derivative of the phase profile, one can calculate the group delay profile over the spatial domain of the chirped grating as shown in Figure 4.15. The group delay introduced by the chirped grating is about 2.67 ns that is expected as the length of the grating sample is 28.5 cm. For this length of the optical fiber, the maximum group delay of 2.7 ns can be achieved.

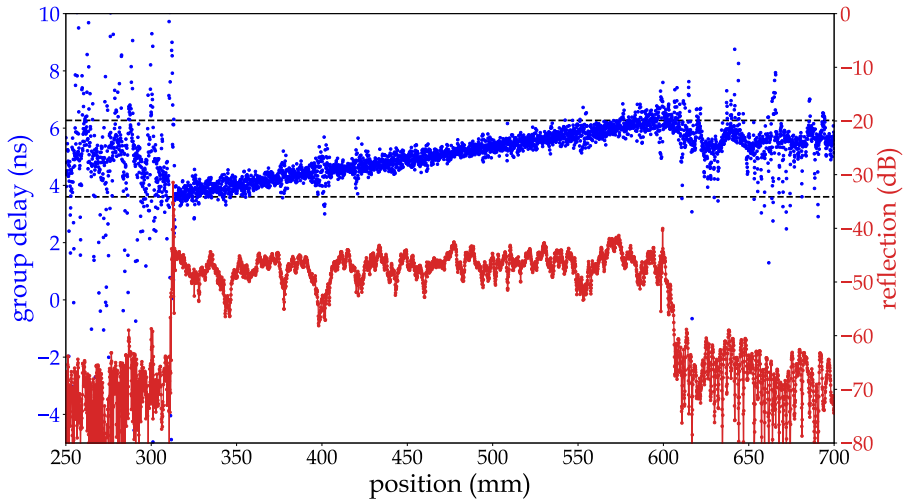

Figure 4.15: Group delay (blue points) and reflection profiles (red points) of the chirped FBG with 1 nm bandwidth designed at 1550 nm, presented in section 4.5, measured by OFDR technique.

To confirm the validity of the performance of the developed OFDR optical setup, I investigate other techniques to get and compare the reflectivity and group delay profiles.

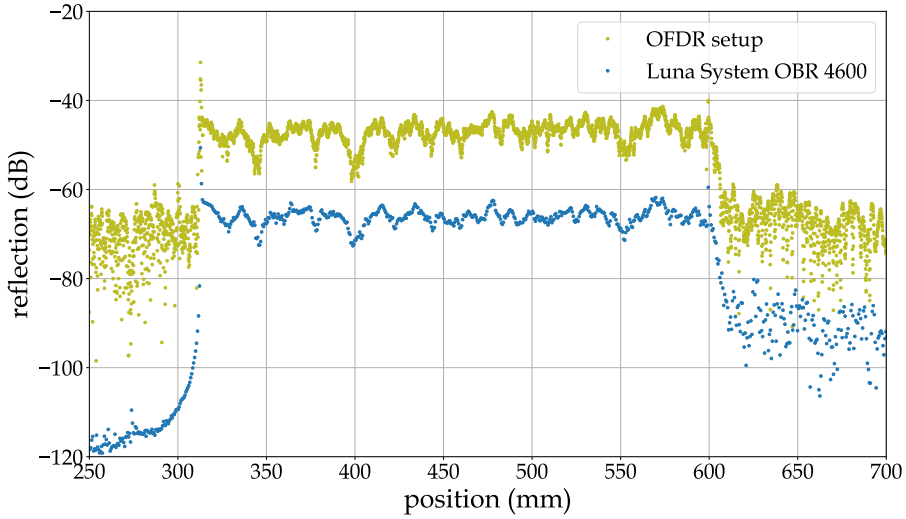

Figure 4.16: Reflection profile of the chirped FBG, presented in section 4.5, measured by OFDR setup (green points) and commercial Luna System (blue points).

I performed these measurements using a commercially available instrument, Luna Systems OBR 4600, that works based on the OFDR technique. I had a short visit at the Optical Fiber Technology Laboratory at the Maria Curie-Skłodowska University to use the Luna System. In this measurement, wavelength was swept with steps of 1.2 pm over a spectral range of 87 nm around the central wavelength of 1550 nm. Figure 4.16 illustrates the reflectivity of the chirped FBG sample as a function of position along the fiber length acquired by the OFDR setup and Luna System. In this plot, the measured reflectivity with the Luna System, indicated with blue points, was shifted along the position axis to match it with the measured reflectivity with the OFDR setup as shown with green points. Comparing both measurements shows similar reflectivity profile for the chirped FBG sample. The difference in reflectivity level may come from different setting of the two apparatus and also non-simultaneous performing of the measurement. The measurement with the OFDR setup was performed right after fabrication of the sample, hydrogen is still exist in the sample, while the measurement by Luna system was performed a few months later.

To verify the temporal response of the sample, group delay of the chirped FBG was also measured using the Luna System. In Figure 4.17, the group delay profile as a function of wavelength is depicted. The group delay of 2.68 ns was measured that is with agreement with the delay measured by the OFDR setup. This measurement also confirms the designed spectral bandwidth of the chirped FBG that is 1 nm as indicated in the figure. There is a slight mismatch between the spectral region shown in Figure 4.17 and Figure 4.10 that is due to different applied strain to the optical

fiber during the measurement process. By applying more strain to the optical fiber, one can shift the spectral response of the grating structures written in the fiber core to reach its designed central wavelength of 1550 nm.

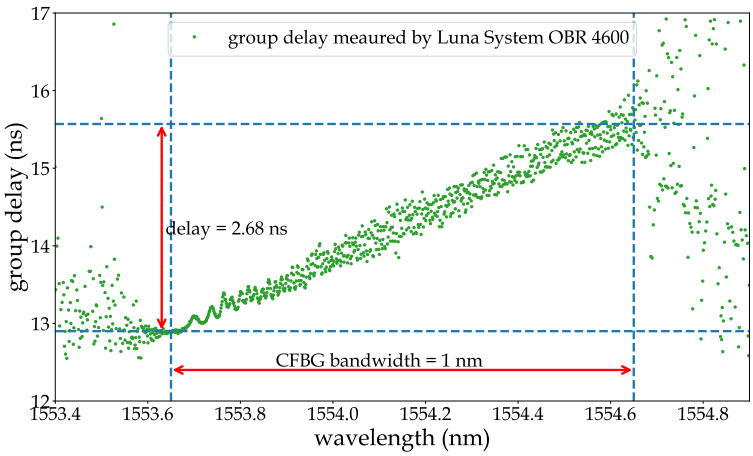

Figure 4.17: Group delay profile of the chirped FBG, presented in section 4.5, measured by Luna System.

Further characterization of the chirped FBG sample was done using another commercial instrument, Agilent Photonic Dispersion and Loss Analyzer 86038B, that employs different approach to measure the group delay and reflectivity profiles. The measurement performed at the Institute of Microelectronics and Optoelectronics at the Warsaw University of Technology. This instrument employs a standard method for group delay measurement based on the modulation phase shift technique [92] in which the shift in the phase of a sinusoidal optical signal, induced by traveling in the DUT, is measured as the laser wavelength is swept. This allows determination of the relative group delay as a function of wavelength. The device was set to sweep by 50 pm wavelength steps. The group delay and reflectivity measurements resulting from this method are plotted in Figure 4.18.

The group delay of 2.63 ns was measured that is in agreement with the value measured by the OFDR technique. Investigating the spectral range that the group delay changes and the reflectivity profile also confirms the 1 nm bandwidth of the chirped FBG sample.

4.7 Fabrication of chirped FBG at 2070 nm

In this section, a custom chirped FBG at the wavelength region of 2 micron is fabricated and characterized based on mentioned methods in the current chapter. The target chirped FBG is designed to introduce a dispersion of 300 ps/nm with

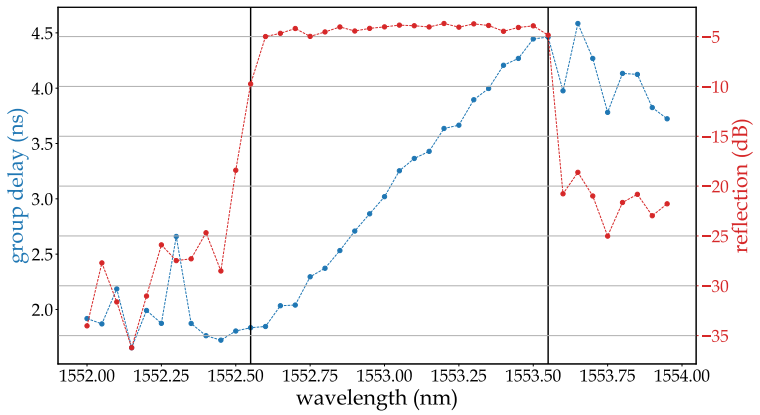

Figure 4.18: Group delay (blue points) and reflection profiles (red points) of the chirped FBG, presented in section 4.5, measured by Agilent Photonic Dispersion and Loss Analyzer 86038B.

a spectral bandwidth of 8 nm at the central wavelength of 2070 μm. Based in the desired grating parameters, one can calculate the length of the chirped FBG.

The UV-writing optical setup is able to inscribe gratings with maximum length of optical fiber of about 28.5 cm. Such a chirped FBG can introduce a maximum delay of about 2.74 ns. Considering the refractive index of the fiber core to be equal to 1.443, one can calculate the length of the chirped FBG sample.

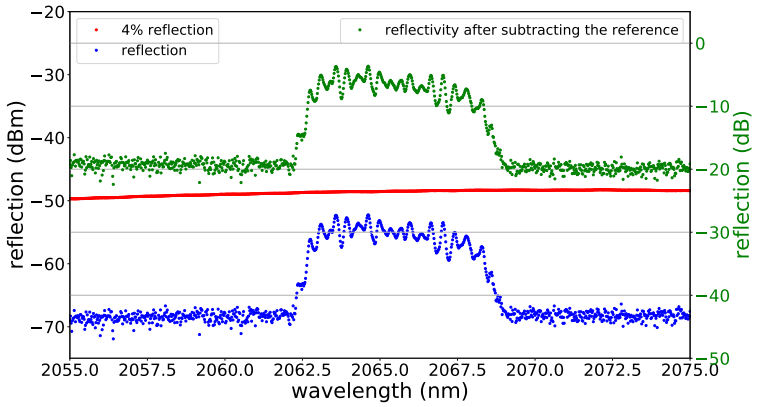

Figure 4.19: Reflectivity measurement of the chirped FBG with bandwidth of 8 nm designed at 2070 nm.

For the target dispersion and spectral bandwidth of the chirped grating, the required delay is is about 2.4 ns. To realize such a delay, the required length of the optical fiber to be used for the UV-writing is calculated that is about 249 mm. This length of Hydrogen loaded single mode fiber , (SM2000, core diameter: 8 μm,

cladding diameter: 125 μm, numerical aperture : 0.18, mode field diameter : $\sim$ 9 μm), with operational wavelength of 2000 nm was prepared and aligned in the UV-writing optical setup. The spectral response of the fabricated grating sample is plotted in Figure 4.19. As explained in section 4.4, for characterizing the spectral response of the grating samples, 4 % Fresnel reflection from one end of the fiber coupler is measured as indicated by red points in Figure 4.19. Then the grating sample is connected to the same end of the fiber coupler, the other end of the fiber coupler has already been terminated by the refractive index matching gel, to measure the spectral reflection profile as indicated by blue points in Figure 4.19. By subtracting the measured spectral reflection profile from the 4 % reference, the actual reflectivity is acquired as shown by green points that is below the 0 dB. This means the reflectivity of the chirped FBG sample is very week. It can be inferred that the Hydrogen loading is not enough to make the fiber core sensitive to UV light absorption.

To make grating structures with stronger reflectivity, one solution is to use optical fiber with higher concentration of doped components that increase photo-sensitivity of the fiber core to the UV light. We choose an ultra-high numerical aperture (UHNA) optical fiber (UHNA7 Nufern, core diameter: 2.4 μm, cladding diameter: 125 μm, numerical aperture : 0.41, mode field diameter : $\sim$ 3 μm) that has higher Germanium doped concentration [93].

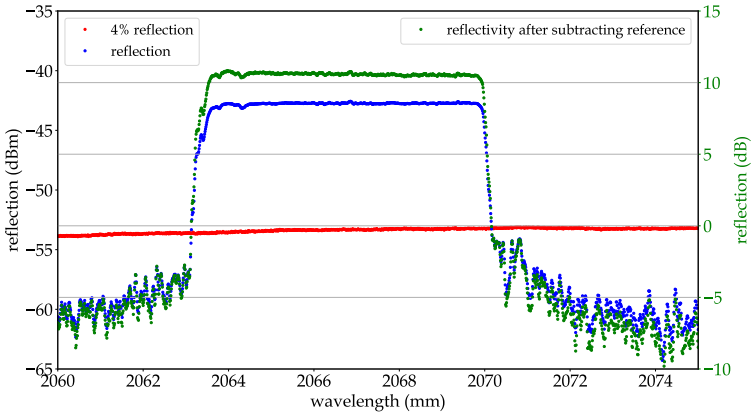

Figure 4.20: Reflectivity measurement of the chirped FBG with bandwidth of 8 nm designed at 2070 nm. The grating was written on UHNA7 optical fiber.

Another chirped FBG sample made of UHNA7 optical fiber with similar specifications as mentioned earlier in the current chapter was fabricated by Rex H. S. Bannerman at the University of Southampton. I characterized the sample to observe the spectral response of the chirped FBG sample as illustrated in Figure 4.20. The reflectivity of the is almost flat over the entire $\sim$ 8 nm bandwidth of the grating. The actual reflectivity of the sample, after subtraction from the 4 % reference, is plotted

by green points. It indicates about 11 dB reflectivity for the chirped FBG sample that is equal to about 12.5 times power gain. Considering the 4 % reference reflection, the actual reflectivity the grating is about 50 %.

We further characterize the grating sample to verify its temporal response by measuring the group delay introduced by the grating.

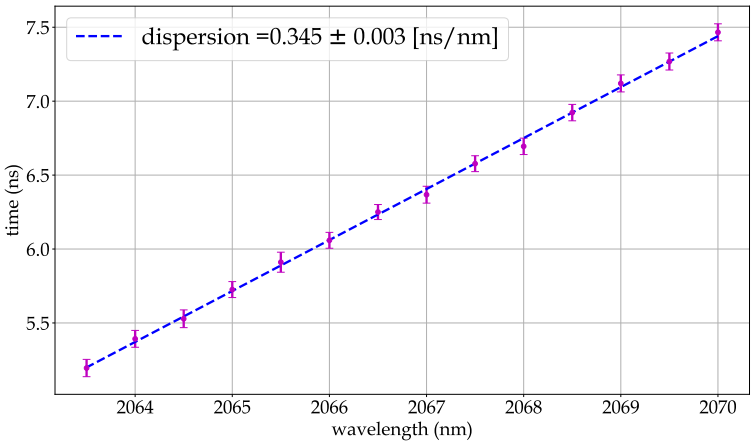

Figure 4.21: Group delay measurement of the chirped FBG with bandwidth of 8 nm designed at 2070 nm. The grating was written using UHNA7 optical fiber.

The developed OFDR setup is operational in telecomme wavelength region so it can not be used to characterize the gratings at wavelength of 2070 nm. For measuring the group delay, a 4-f spectral filter operating at 2 μm wavelength was developed to prepare narrowband band pulses to perform time of flight measurement. This method allows to measure reflected pulses from different locations along the grating length respect to a reference time. The group delay measurement was performed by Michał Mikołajczyk as plotted in Figure 4.21. By fitting the blue dashed-line to the measured points, one can calculate the introduced dispersion that is equal to about 345 ps/nm. The measured value is relatively close to the designed dispersion value of the 300 ps/nm.

4.8 Designing non-linear chirped Bragg grating

In this section, initial investigation is done to develop a non-linear grating to compensate an arbitrary dispersion profile. The goal is to fabricate custom chirped FBG structure to compensate a non-linear dispersion resulting from electro-optic phase modulation (EOPM) process when the modulator is driven by a sinusoidal temporal phase. In this case, the optical pulse passing thorough the modulator receives

a non-linear dispersion pattern that can be perfectly compensated by a dedicated structure of chirped FBG so that the introduced aberration is eliminated. Such a non-linear chirped FBG can be used along with the quadratic temporal phase modulation profile, presented in subsection 2.5.4, to make the time-lensing system with enhanced performance [94].

The goal is to find the nonlinear dispersion profile that compensate the temporal phase modulation in the time-lensing system. To fabricate the nonlinear dispersion profile, one needs the group delay profile as function of wavelength. The group delay is defined as:

$$t_g(\omega) = \frac{\partial \varphi(\omega)}{\partial \omega}. \tag{4.13}$$

where $\varphi(\omega)$ is the spectral phase that contains time versus frequency information. It is worth to mention that it would be a mistake to find the group delay directly from the temporal phase profile. Although the temporal phase contains frequency versus time information but we should remember that $t_g(\omega)$ is not the inverse of $\omega(t)$ [25].

4.8.1 Procedure to obtain nonlinear dispersion profile from arbitrary temporal phase

Here, I present simulation calculations to obtain the nonlinear dispersion profile. First step is to prepare a temporal phase profile, 10 GHz sinusoidal electronic signal with amplitude of 10 radians, that is applied by the EOPM. A Gaussian pulse in time domain, $E(t)$, as input optical fieled into the EOPM is considered as

$$E(t) = \exp\left[-4\ln 2\frac{t^2}{T^2}\right], \tag{4.14}$$

where T is the temporal FWHM of the input optical field. In the simulation, the temporal FWHM intensity of about 6 ps was considered that is equivalent to spectral FWHM intensity of 0.6 nm. The the temporal phase profile in the form of sinusoidal RF signal is applied to the input optical field.

$$\phi(t) = A\sin\left(2\pi f_{\mathrm{RF}} t\right), \tag{4.15}$$

where f_{RF} is the modulation frequency and A is amplitude of the sinusoidal signal. The temporal FWHM of the input pulse is defined such that covers quadratic part of the sinusoidal RF signal as illustrated in Figure 4.22. This ensures that the whole temporal phase profile is encoded in the travelling Gaussian pulse in the EOPM. The optical pulse after temporal phase modulation, $E_{\mathrm{PM}}(t)$, is expressed as

$$E_{\mathrm{PM}}(t) = E(t)\exp\left[i\phi(t - t_0)\right], \tag{4.16}$$

the delay time t_0 is adjusted to synchronize the quadratic part of the sinusoidal pulse to the optical pulse.

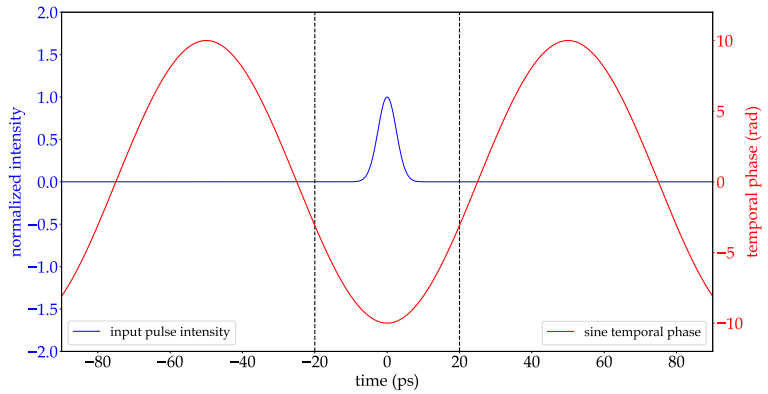

Figure 4.22: Input pulse intensity (blue line) and sinusoidal temporal phase profile used to modulate the EOPM (red line).

To acquire the dispersion profile that can compensate the imparted sinusoidal temporal phase, one can extract the spectral phase, $\varphi(\omega)$, from the modulated optical pulse. Then the group delay and group delay dispersion (GDD) profiles can be calculated from the acquired spectral phase. Considering the electric optical field after applying the temporal phase modulation, Equation 4.16, and taking Fourier transform, one can obtain the modulated optical pulse in frequency domain as

$$\tilde{E}_{\mathrm{PM}}(\omega) = \mathcal{F}\{E(t)\}. \tag{4.17}$$

From the complex optical field in the frequency domain, one can acquire the spectral phase. Figure 4.23 shows the spectral phase profile after unwrapping.

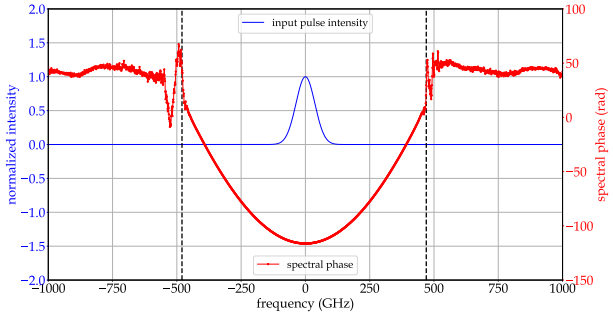

Figure 4.23: Spectral phase profile.

Next step is to achieve the group delay profile from the acquired spectral phase. The group delay is calculated by taking the derivative of the spectral phase respect to the angular frequency:

$$\tau_g = \frac{\partial \varphi(\omega)}{\partial \omega}. \tag{4.18}$$

By considering the region of interest where the quadratic-like phase appears in the spectral phase profile, one can find the group delay profile as illustrated in Figure 4.24. Note that the re-scaling has been performed to get the group delay profile over wavelength range, central wavelength of 1560 nm, corresponding to the frequency bandwidth of the calculated spectral phase.

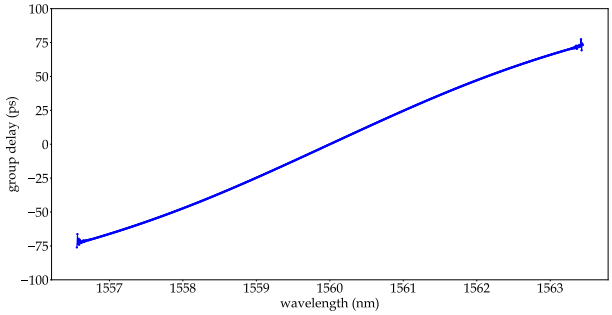

Figure 4.24: Group delay profile.

The GDD profile can also be calculated from the acquired group delay by taking its derivative respective to the angular frequency:

$$\text{GDD} = \frac{\partial \tau_g}{\partial \omega} = \frac{\partial^2 \varphi(\omega)}{\partial \omega^2}. \tag{4.19}$$

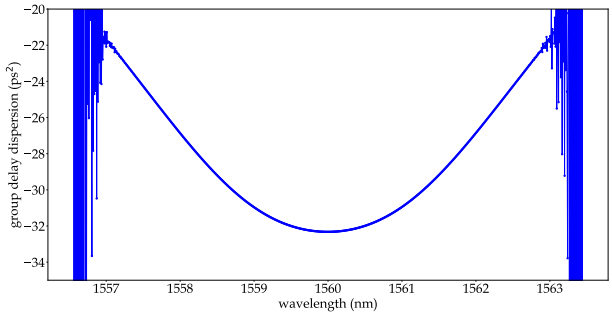

Figure 4.25: Group delay dispersion profile.

4.8.2 Simulation of time lens system using nonlinear dispersion profile

Now the GDD profile is employed as dispersive element in the simulation code of sinusoidal time lens system. We consider a Gaussian optical pulse in the spectrum as

$$E(\omega) = \exp\left[-4\ln 2\frac{\omega^2}{W^2}\right]. \tag{4.20}$$

where W is spectral bandwidth of the input Gaussian pulse. To implement the time lens system, we first apply a dispersion to the optical pulse to temporally disperse the pulse and then a quadratic-like temporal phase is imparted to spectrally compress or expand the optical pulse. The acquired nonlinear dispersion profile, in the previous section, is applied to the input optical pulse in the spectral domain as

$$E_{\mathrm{D}}(\omega) = E(\omega)\exp\left[-i\Phi_{\mathrm{GDD}}\frac{\omega^2}{2}\right], \tag{4.21}$$

where Φ_{GDD} is the group delay dispersion. The next step of the simulation is to apply temporal phase profile to the dispersed optical pulse. By taking the Fourier transform of the optical pulse in the spectrum, $E_{\mathrm{D}}(\omega)$, the optical pulse in temporal domain is obtained as

$$\tilde{E}_{\mathrm{D}}(t) = \mathcal{F}\{E_{\mathrm{D}}(\omega)\}, \tag{4.22}$$

now the sinusoidal temporal phase profile, amplitude of 10 radians and frequency of 10 GHz, is applied to the dispersed optical pulse in temporal domain to spectrally compress it. This requires to synchronise the minima of the sinusoidal signal with the central frequency of the optical pulse by introducing time shift.

$$\tilde{E}_{\mathrm{out}}(t) = \tilde{E}_{\mathrm{D}}(t)\ \exp\left[i\phi(t)\right], \tag{4.23}$$

where

$$\phi(t) = A\sin\left(2\pi f_{\mathrm{RF}}(t - t_0)\right), \tag{4.24}$$

where t_0 is determined in a way to synchronize the minima of the sinusoidal RF modulating signal to the optical pulse. Finally, by taking Fourier transform of the output optical pulse, $\tilde{E}_{\mathrm{out}}(t)$, one can observe the effect of the time-lensing system in the spectral domain as shown by red line in Figure 4.26.

In the simulation, for the input Gaussian pulse, input intensity with FWHM of 2.5 nm at central wavelength of 1560 nm was considered that is equivalent to frequency bandwidth of 308 GHz as shown by black line in Figure 4.26. This is roughly the maximum input bandwidth that one can make sure the optical pulse does not exceed the region indicated with vertical dashed lines in the spectral phase profile as shown in Figure 4.23. For the time-lensing system with modified GDD profile, the FWHM intensity of the spectrally compressed pulse was calculated about 17 GHz as illustrated by red line in Figure 4.26. This corresponds to about 18 times spectral compression factor.

To evaluate the performance of the nonlinear GDD profile used in the time-lensing system, one can compare it with the case that the linear dispersion profile, parabolic

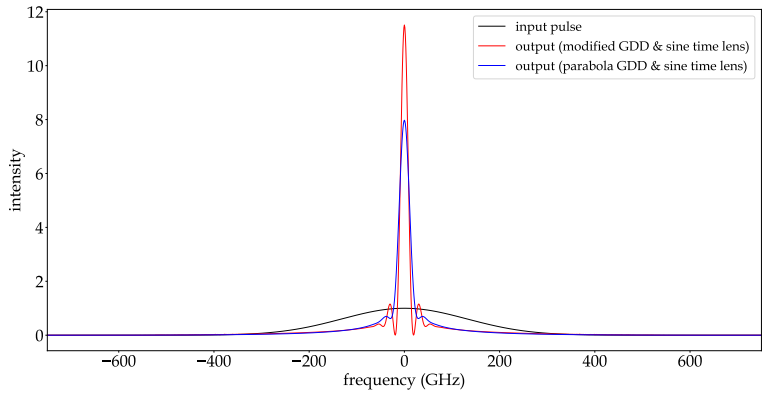

Figure 4.26: Input optical pulse (black line) and spectrally compressed pulse by using parabolic GDD profile, linear dispersion (blue line) and modified GDD profile, nonlinear dispersion, (red line).

GDD, is used. In experiment, this can be done by employing a piece of optical fiber. As mentioned in the first chapter, to define the dispersion introduced by a piece of optical fiber, the formula $\Phi_{GDD} = \beta_2 z$ is considered in which z is the length of the optical fiber and β_2 is the group velocity dispersion (GVD) coefficient that is equal to about β_2 = -21.7 ps^2/km for single mode fiber. In this simulation, 1.2 km of optical fiber was considered. This length of fiber disperses the input pulse to roughly match the time aperture of the applied sinusoidal temporal phase. For the time-lensing system with linear dispersion profile, the FWHM intensity of the spectrally compressed pulse was calculated about 25 GHz as shown by blue line in Figure 4.26 which is equal to about 12 times spectral compression factor.

Comparing the performance of time-lensing system with linear and nonlinear dispersion profiles indicates that our designed (nonlinear) dispersion profile has $\sim$ 34 percent improvement in spectral compression factor. On can also investigate the amplitude enhancement in the system. Starting with normalized amplitude of the input pulse, for the case that linear dispersion is used, the enhancement is $\sim$ 8 whereas this value is $\sim$ 11.5 in the case that the nonlinear dispersion profile is used. The enhancement values also indicate $\sim$ 31 percent improvement when the nonlinear dispersion is employed.

4.8.3 Chapter summary and outlook

In this chapter, first, the procedure for designing and fabrication of fiber Bragg grating (FBG) structures was introduced where an interferometric optical setup was employed to apply desired modulation of refractive index in the fiber core. I used an existing UV-writing optical setup to fabricate several samples of chirped FBGs at central

wavelength of 1560 nm and 2070 nm with different temporal and spectral responses. To evaluate the performance of the fabricated samples, I have built an optical setup based of optical frequency domain reflectometry to characterize the fabricated chirped FBG samples at 1560 nm wavelength. Furthermore, I developed a simulation code to acquire the nonlinear dispersion profile that can compensate sinusoidal temporal phase profile in the time-lensing system. This nonlinear dispersion profile is going to be fabricated.

Future work will be to design and fabrication of a chirped FBG sample can compensate the resulting temporal phase profile from the photodiode that was presented in subsection 2.5.4. This will enable us to make nonlinear chirped FBG structures that can shape light pulses in arbitrary manner in both time and frequency domains [95].

Chapter 5

Conclusion

In this thesis, active and passive approaches for time-frequency transformation of optical pulses were investigated that are not only applicable in classical regime but also can be applied to single photon wave packets. Investigated methods opened new ways toward spectral and temporal shaping and measurement of short pulse that are crucial necessity to quantum information processing, communication and meteorology applications. First, the active manipulation of optical pulses using electro-optic effect and phase modulation process was investigated to temporally and spectrally shape short optical pulses. Second, the passive optical elements based on fiber Bragg gratings were fabricated to shape the temporal and spectral characteristics of the optical pulses.

For the first approach, it was demonstrated that linear or quadratic temporal phase can be applied to optical pulse to induce a spectral shift or perform spectral bandwidth manipulation, respectively. The phase is induced using an electro-optic phase modulator (EOPM) which is driven by an amplified signal from a high-bandwidth photodiode while the optical pulse is phase locked to the modulating voltage signal. The photodiode pulse was characterized to use it for spectral compression and spectral shifting applications. The main advantages of using modulation driving signal from a photodiode are that it does not require reference signal and reduces cost in comparison using function generator to prepare driving signal. Furthermore, this approach can be implemented in different wavelength range depending on operational wavelength of the EOPM.

As an application, it also was demonstrated that this electro-optic approach can be employed to measure single photon pulse envelope. To realize this goal, an interferometric optical setup was developed and the linear temporal phase was employed to implement the measurement scheme. Considering the Fourier transform property, applying a linear temporal phase to the optical pulse corresponds to a spectral shift of the pulse in the frequency domain, the frequency autocorelation of the

optical pulse was performed to determine the temporal envelope of the optical pulse. Using this property along with tunable electro-optic spectral shearing interferometery method, made it possible to measure time duration of both classical and quantum light pulse. This novel technique can measure short optical pulses without time resolved detection and is central wavelength independent and intrinsically free of photon noise.

For the second approach, passive optical elements were fabricated based on chirped fiber Bragg grating (FBG) structures to be employed as dispersive element. Several chirped FBG samples were engineered to temporally and spectrally shape optical pulses at wavelengths of 1560 nm and 2070 nm. To fabricate the samples, an interferometric technique was employed for point by point inscribing the grating structures in the fiber core under interference of UV light beams. This fabrication technique allowed to inscribe gratings with arbitrary refractive index modulation profile and also arbitrary apodization profile. By controlling these parameters, custom grating structures with desired spectral and temporal specifications were fabricated. These samples were characterized in terms of their temporal and spectral performances via different techniques. In this context, optical frequency domain reflectivity technique was developed to monitor the effective refractive index change along the fiber and to measure group delay profile. In addition, initial investigation was done to develop non-linear grating to compensate an arbitrary dispersion profile. Simulation calculations was performed to design a non-linear chirped FBG that can compensate a non-linear dispersion profile.

Bibliography

[1] Pieter Kok et al. "Linear optical quantum computing with photonic qubits". In: *Reviews of Modern Physics* 79.1 (Jan. 2007), pp. 135–174. URL: https://doi.org/10.1103/revmodphys.79.135 (cit. on p. 1).

[2] Hugues de Riedmatten et al. "Tailoring photonic entanglement in high-dimensional Hilbert spaces". In: *Physical Review A* 69.5 (May 2004). URL: https://doi.org/10.1103/physreva.69.050304 (cit. on p. 2).

[3] Alex Hayat et al. "Multidimensional quantum information based on single-photon temporal wavepackets". In: *Optics Express* 20.28 (Dec. 2012), p. 29174. URL: https://doi.org/10.1364/oe.20.029174 (cit. on p. 2).

[4] Peter C. Humphreys et al. "Linear Optical Quantum Computing in a Single Spatial Mode". In: *Research in Optical Sciences*. OSA, 2014. URL: https://doi.org/10.1364/qim.2014.qth2a.4 (cit. on pp. 2, 3).

[5] E. Knill, R. Laflamme, and G. J. Milburn. "A scheme for efficient quantum computation with linear optics". In: *Nature* 409.6816 (Jan. 2001), pp. 46–52. URL: https://doi.org/10.1038/35051009 (cit. on p. 2).

[6] Joseph M. Lukens and Pavel Lougovski. "Frequency-encoded photonic qubits for scalable quantum information processing". In: *Optica* 4.1 (Dec. 2017), p. 8. URL: https://doi.org/10.1364/optica.4.000008 (cit. on pp. 2–4).

[7] B. Brecht et al. "Photon Temporal Modes: A Complete Framework for Quantum Information Science". In: *Physical Review X* 5.4 (Oct. 2015). URL: https://doi.org/10.1103/physrevx.5.041017 (cit. on pp. 2, 4).

[8] J. D. Franson. "Bell inequality for position and time". In: *Physical Review Letters* 62.19 (May 1989), pp. 2205–2208. URL: https://doi.org/10.1103/physrevlett.62.2205 (cit. on p. 2).

[9] J. Brendel et al. "Pulsed Energy-Time Entangled Twin-Photon Source for Quantum Communication". In: *Physical Review Letters* 82.12 (Mar. 1999), pp. 2594–2597. URL: https://doi.org/10.1103/physrevlett.82.2594 (cit. on p. 2).

[10] I. Marcikic et al. "Time-bin entangled qubits for quantum communication created by femtosecond pulses". In: *Physical Review A* 66.6 (Dec. 2002). URL: https://doi.org/10.1103/physreva.66.062308 (cit. on p. 2).

[11] John M. Donohue et al. "Coherent Ultrafast Measurement of Time-Bin Encoded Photons". In: *Physical Review Letters* 111.15 (Oct. 2013). URL: https://doi.org/10.1103/physrevlett.111.153602 (cit. on p. 3).

[12] Damien Stucki et al. "Fast and simple one-way quantum key distribution". In: *Applied Physics Letters* 87.19 (Nov. 2005), p. 194108. URL: https://doi.org/10.1063/1.2126792 (cit. on p. 3).

[13] Nurul T. Islam et al. "Provably secure and high-rate quantum key distribution with time-bin qudits". In: *Science Advances* 3.11 (Nov. 2017). URL: https://doi.org/10.1126/sciadv.1701491 (cit. on p. 3).

[14] Joseph M. Lukens. "Quantum information processing with frequency-bin qubits: progress, status, and challenges". In: *Conference on Lasers and Electro-Optics*. OSA, 2019. URL: https://doi.org/10.1364/cleo_at.2019.jtu4a.3 (cit. on p. 3).

[15] Michael Kues et al. "On-chip generation of high-dimensional entangled quantum states and their coherent control". In: *Nature* 546.7660 (June 2017), pp. 622–626. URL: https://doi.org/10.1038/nature22986 (cit. on pp. 3, 4).

[16] Stéphane Clemmen et al. "Ramsey Interference with Single Photons". In: *Physical Review Letters* 117.22 (Nov. 2016). URL: https://doi.org/10.1103/physrevlett.117.223601 (cit. on p. 3).

[17] Marco Liscidini and J. E. Sipe. "Scalable and efficient source of entangled frequency bins". In: *Optics Letters* 44.11 (May 2019), p. 2625. URL: https://doi.org/10.1364/ol.44.002625 (cit. on p. 4).

[18] Poolad Imany et al. "50-GHz-spaced comb of high-dimensional frequency-bin entangled photons from an on-chip silicon nitride microresonator". In: *Optics Express* 26.2 (Jan. 2018), p. 1825. URL: https://doi.org/10.1364/oe.26.001825 (cit. on p. 4).

[19] Vahid Ansari et al. "Tailoring nonlinear processes for quantum optics with pulsed temporal-mode encodings". In: *Optica* 5.5 (May 2018), p. 534. URL: https://doi.org/10.1364/optica.5.000534 (cit. on pp. 4, 5).

[20] *Ultrashort Laser Pulse Phenomena*. Elsevier, 2006. URL: https://doi.org/10.1016/b978-0-12-215493-5.x5000-9 (cit. on pp. 7, 50).

[21] Vıctor Torres-Company, Jesús Lancis, and Pedro Andrés. "Space-Time Analogies in Optics". In: *Progress in Optics*. Elsevier, 2011, pp. 1–80. URL: https://doi.org/10.1016/b978-0-444-53886-4.00001-0 (cit. on pp. 9, 10, 37, 40).

[22] *Nonlinear Fiber Optics*. Elsevier, 2013. URL: https://doi.org/10.1016/c2011-0-00045-5 (cit. on p. 11).

[23] *Nonlinear Fiber Optics*. Elsevier, 2013. URL: https://doi.org/10.1016/c2011-0-00045-5 (cit. on pp. 12, 71).

[24] B.E.A. Saleh and M.C. Teich. *Fundamentals of Photonics*. Wiley series in pure and applied optics. Wiley India, 2007. ISBN: 9788126537747. URL: https://books.google.pl/books?id=kfUUzgEACAAJ (cit. on pp. 12, 35).

[25] Rick Trebino. *Frequency-Resolved Optical Gating: The Measurement of Ultrashort Laser Pulses*. Springer US, 2000. URL: https://doi.org/10.1007/978-1-4615-1181-6 (cit. on pp. 13–15, 17, 18, 97).

[26] *Nonlinear Optics*. Elsevier, 2003. URL: https://doi.org/10.1016/b978-0-12-121682-5.x5000-7 (cit. on pp. 13, 30, 35).

[27] K. Sala, G. Kenney-Wallace, and G. Hall. "CW autocorrelation measurements of picosecond laser pulses". In: *IEEE Journal of Quantum Electronics* 16.9 (Sept. 1980), pp. 990–996. URL: https://doi.org/10.1109/jqe.1980.1070606 (cit. on p. 15).

[28] J. A. Armstrong. "Measurement of picosecond laser pulse widths". In: *Applied Physics Letters* 10.1 (Jan. 1967), pp. 16–18. URL: https://doi.org/10.1063/1.1754787 (cit. on p. 15).

[29] Ian A. Walmsley and Christophe Dorrer. "Characterization of ultrashort electromagnetic pulses". In: *Advances in Optics and Photonics* 1.2 (Apr. 2009), p. 308. URL: https://doi.org/10.1364/aop.1.000308 (cit. on pp. 15, 16, 33).

[30] Andrew M. Weiner. *Ultrafast Optics*. Wiley, Oct. 2008. URL: https://doi.org/10.1002/9780470473467 (cit. on p. 15).

[31] Norbert Wiener. "Generalized harmonic analysis". In: *Acta Mathematica* 55.0 (1930), pp. 117–258. URL: https://doi.org/10.1007/bf02546511 (cit. on p. 16).

[32] A. Khintchine. "Korrelationstheorie der stationren stochastischen Prozesse". In: *Mathematische Annalen* 109.1 (Dec. 1934), pp. 604–615. URL: https://doi.org/10.1007/bf01449156 (cit. on p. 16).

[33] Daniel J. Kane and Rick Trebino. "Single-shot measurement of the intensity and phase of an arbitrary ultrashort pulse by using frequency-resolved optical gating". In: *Optics Letters* 18.10 (May 1993), p. 823. URL: https://doi.org/10.1364/ol.18.000823 (cit. on pp. 19, 50).

[34] Claude Rullière, ed. *Femtosecond Laser Pulses*. Springer New York, 2005. URL: https://doi.org/10.1007/b137908 (cit. on p. 19).

[35] K. W. DeLong et al. "Frequency-resolved optical gating with the use of second-harmonic generation". In: *Journal of the Optical Society of America B* 11.11 (Nov. 1994), p. 2206. URL: https://doi.org/10.1364/josab.11.002206 (cit. on p. 19).

[36] Victor Wong and Ian A. Walmsley. "Analysis of ultrashort pulse-shape measurement using linear interferometers". In: *Optics Letters* 19.4 (Feb. 1994), p. 287. URL: https://doi.org/10.1364/ol.19.000287 (cit. on p. 20).

[37] C. Iaconis and I. A. Walmsley. "Spectral phase interferometry for direct electric-field reconstruction of ultrashort optical pulses". In: *Optics Letters* 23.10 (May 1998), p. 792. URL: https://doi.org/10.1364/ol.23.000792 (cit. on pp. 20, 50).

[38] Christophe Dorrer and Inuk Kang. "Highly sensitive direct characterization of femtosecond pulses by electro-optic spectral shearing interferometry". In: *Optics Letters* 28.6 (Mar. 2003), p. 477. URL: https://doi.org/10.1364/ol.28.000477 (cit. on pp. 21, 33).

[39] Alex O. C. Davis et al. "Measuring the Single-Photon Temporal-Spectral Wave Function". In: *Physical Review Letters* 121.8 (Aug. 2018). URL: https://doi.org/10.1103/physrevlett.121.083602 (cit. on p. 21).

[40] P. Maine et al. "Generation of ultrahigh peak power pulses by chirped pulse amplification". In: *IEEE Journal of Quantum Electronics* 24.2 (Feb. 1988), pp. 398–403. URL: https://doi.org/10.1109/3.137 (cit. on p. 21).

[41] F. J. Duarte, ed. *Coherence and Ultrashort Pulse Laser Emission*. InTech, Dec. 2010. URL: https://doi.org/10.5772/543 (cit. on p. 21).

[42] M. Matsumoto and H.A. Haus. "Stretched-pulse optical fiber communications". In: *IEEE Photonics Technology Letters* 9.6 (June 1997), pp. 785–787. URL: https://doi.org/10.1109/68.584990 (cit. on p. 21).

[43] Ming Lai, Shui T. Lai, and Casimir Swinger. "Single-grating laser pulse stretcher and compressor". In: *Applied Optics* 33.30 (Oct. 1994), p. 6985. URL: https://doi.org/10.1364/ao.33.006985 (cit. on p. 22).

[44] Vikrant Chauhan et al. "Single-diffraction-grating and grism pulse compressors". In: *Journal of the Optical Society of America B* 27.4 (Mar. 2010), p. 619. URL: https://doi.org/10.1364/josab.27.000619 (cit. on p. 22).

[45] D. Pastor et al. "Design of apodized linearly chirped fiber gratings for dispersion compensation". In: *Journal of Lightwave Technology* 14.11 (1996), pp. 2581–2588. URL: https://doi.org/10.1109/50.548158 (cit. on p. 23).

[46] T. Erdogan. "Fiber grating spectra". In: *Journal of Lightwave Technology* 15.8 (1997), pp. 1277–1294. URL: https://doi.org/10.1109/50.618322 (cit. on pp. 23, 78).

[47] K. Okamoto and T. Hosaka. "Polarization-dependent chromatic dispersion in birefringent optical fibers". In: *Optics Letters* 12.4 (Apr. 1987), p. 290. URL: https://doi.org/10.1364/ol.12.000290 (cit. on p. 25).

[48] Govind P. Agrawal. *Fiber-Optic Communication Systems*. Wiley, Oct. 2010. URL: https://doi.org/10.1002/9780470918524 (cit. on pp. 26, 27).

[49] P. G. Evans et al. "Bright Source of Spectrally Uncorrelated Polarization-Entangled Photons with Nearly Single-Mode Emission". In: *Physical Review Letters* 105.25 (Dec. 2010). URL: https://doi.org/10.1103/physrevlett.105.253601 (cit. on pp. 27, 71).

[50] Kiyoshi Kato and Eiko Takaoka. "Sellmeier and thermo-optic dispersion formulas for KTP". In: *Applied Optics* 41.24 (Aug. 2002), p. 5040. URL: https://doi.org/10.1364/ao.41.005040 (cit. on p. 28).

[51] Evan Meyer-Scott et al. "Limits on the heralding efficiencies and spectral purities of spectrally filtered single photons from photon-pair sources". In: *Physical Review A* 95.6 (June 2017). DOI: 10.1103/physreva.95.061803. URL: https://doi.org/10.1103/physreva.95.061803 (cit. on p. 29).

[52] C. J. McKinstrie et al. "Quantum-state-preserving optical frequency conversion and pulse reshaping by four-wave mixing". In: *Physical Review A* 85.5 (May 2012). URL: https://doi.org/10.1103/physreva.85.053829 (cit. on p. 33).

[53] J. P. Heritage, A. M. Weiner, and R. N. Thurston. "Picosecond pulse shaping by spectral phase and amplitude manipulation". In: *Optics Letters* 10.12 (Dec. 1985), p. 609. URL: https://doi.org/10.1364/ol.10.000609 (cit. on p. 34).

[54] Z. Zheng and A. M. Weiner. "Spectral phase correlation of coded femtosecond pulses by second-harmonic generation in thick nonlinear crystals". In: *Optics Letters* 25.13 (July 2000), p. 984. URL: https://doi.org/10.1364/ol.25.000984 (cit. on p. 34).

[55] I.P. Kaminow et al. "Thin-film LiNbOsub3/sub electro-optic light modulator". In: *Applied Physics Letters* 22.10 (May 1973), pp. 540–542. URL: https://doi.org/10.1063/1.1654500 (cit. on p. 35).

[56] Antao Chen and Edmond Murphy, eds. *Broadband optical modulators: science, technology, and applications*. CRC Press, Apr. 2016. URL: https://doi.org/10.1201/b11444 (cit. on pp. 36, 40).

[57] Laura J. Wright et al. "Spectral Shearing of Quantum Light Pulses by Electro-Optic Phase Modulation". In: *Physical Review Letters* 118.2 (Jan. 2017). URL: https://doi.org/10.1103/physrevlett.118.023601 (cit. on pp. 39, 53).

[58] Ilya Y. Poberezhskiy et al. "Electro-optic polymer frequency shifter activated by input optical pulses". In: *Optics Letters* 28.17 (Sept. 2003), p. 1570. URL: https://doi.org/10.1364/ol.28.001570 (cit. on p. 41).

[59] C. Iaconis and I.A. Walmsley. "Self-referencing spectral interferometry for measuring ultrashort optical pulses". In: *IEEE Journal of Quantum Electronics* 35.4 (Apr. 1999), pp. 501–509. URL: https://doi.org/10.1109/3.753654 (cit. on p. 44).

[60] Michał Jachura et al. "Measurement of radio-frequency temporal phase modulation using spectral interferometry". In: *Journal of Modern Optics* 65.3 (Oct. 2017), pp. 262–267. URL: https://doi.org/10.1080/09500340.2017.1387676 (cit. on p. 45).

[61] K. Creath and J. Schmit. "Interferometry | Phase-Measurement Interferometry". In: *Encyclopedia of Modern Optics*. Elsevier, 2005, pp. 364–374. URL: https://doi.org/10.1016/b0-12-369395-0/00820-4 (cit. on p. 48).

[62] Xianyu Su and Wenjing Chen. "Reliability-guided phase unwrapping algorithm: a review". In: *Optics and Lasers in Engineering* 42.3 (Sept. 2004), pp. 245–261. URL: https://doi.org/10.1016/j.optlaseng.2003.11.002 (cit. on p. 48).

[63] Ahmed H. Zewail. "Femtochemistry: Atomic-Scale Dynamics of the Chemical Bond Using Ultrafast Lasers (Nobel Lecture)". In: *Angewandte Chemie International Edition* 39.15 (Aug. 2000), pp. 2586–2631. URL: https://doi.org/10.1002/1521-3773(20000804)39:15%3C2586::aid-anie2586%3E3.0.co;2-o (cit. on p. 50).

[64] A. A. Lanin et al. "Time-domain spectroscopy in the mid-infrared". In: *Scientific Reports* 4.1 (Oct. 2014). URL: https://doi.org/10.1038/srep06670 (cit. on p. 50).

[65] Th. Udem, R. Holzwarth, and T. W. Hänsch. "Optical frequency metrology". In: *Nature* 416.6877 (Mar. 2002), pp. 233–237. URL: https://doi.org/10.1038/416233a (cit. on p. 50).

[66] Jianshu Cao et al. "Quantum biology revisited". In: *Science Advances* 6.14 (Apr. 2020). URL: https://doi.org/10.1126/sciadv.aaz4888 (cit. on p. 50).

[67] Peter C. Humphreys et al. "Linear Optical Quantum Computing in a Single Spatial Mode". In: *Physical Review Letters* 111.15 (Oct. 2013). URL: https://doi.org/10.1103/physrevlett.111.150501 (cit. on p. 50).

[68] Jeremy L. O'Brien. "Optical Quantum Computing". In: *Science* 318.5856 (Dec. 2007), pp. 1567–1570. URL: https://doi.org/10.1126/science.1142892 (cit. on p. 50).

[69] J. M. Donohue et al. "Quantum-Limited Time-Frequency Estimation through Mode-Selective Photon Measurement". In: *Physical Review Letters* 121.9 (Aug. 2018). URL: https://doi.org/10.1103/physrevlett.121.090501 (cit. on p. 50).

[70] Ali Golestani et al. "Electro-Optic Fourier Transform Chronometry of Pulsed Quantum Light". In: *Physical Review Letters* 129.12 (Sept. 2022). URL: https://doi.org/10.1103/physrevlett.129.123605 (cit. on p. 53).

[71] Christophe Dorrer et al. "Spectral resolution and sampling issues in Fourier-transform spectral interferometry". In: *Journal of the Optical Society of America B* 17.10 (Oct. 2000), p. 1795. URL: https://doi.org/10.1364/josab.17.001795 (cit. on p. 57).

[72] F. Sośnicki et al. "Aperiodic electro-optic time lens for spectral manipulation of single-photon pulses". In: *Applied Physics Letters* 116.23 (June 2020), p. 234003. URL: https://doi.org/10.1063/5.0011077 (cit. on p. 60).

[73] Nicola Montaut et al. "High-Efficiency Plug-and-Play Source of Heralded Single Photons". In: *Physical Review Applied* 8.2 (Aug. 2017). URL: https://doi.org/10.1103/physrevapplied.8.024021 (cit. on p. 74).

[74] N. Takato et al. "Silica-based single-mode waveguides on silicon and their application to guided-wave optical interferometers". In: *Journal of Lightwave Technology* 6.6 (June 1988), pp. 1003–1010. URL: https://doi.org/10.1109/50.4091 (cit. on p. 75).

[75] Inna Krasnokutska et al. "Ultra-low loss photonic circuits in lithium niobate on insulator". In: *Optics Express* 26.2 (Jan. 2018), p. 897. URL: https://doi.org/10.1364/oe.26.000897 (cit. on p. 76).

[76] Di Zhu et al. "Integrated photonics on thin-film lithium niobate". In: *Advances in Optics and Photonics* 13.2 (May 2021), p. 242. URL: https://doi.org/10.1364/aop.411024 (cit. on p. 76).

[77] Meint Smit et al. "An introduction to InP-based generic integration technology". In: *Semiconductor Science and Technology* 29.8 (June 2014), p. 083001. URL: https://doi.org/10.1088/0268-1242/29/8/083001 (cit. on p. 76).

[78] D. Liang and J.E. Bowers. "Photonic integration: Si or InP substrates?" In: *Electronics Letters* 45.12 (2009), p. 578. URL: https://doi.org/10.1049/el.2009.1279 (cit. on p. 76).

[79] Katsunari Okamoto. In: *Optical and Quantum Electronics* 31.2 (1999), pp. 107–129. URL: https://doi.org/10.1023/a:1006975415469 (cit. on p. 76).

[80] Martin Papes et al. "Fiber-chip edge coupler with large mode size for silicon photonic wire waveguides". In: *Optics Express* 24.5 (Feb. 2016), p. 5026. URL: https://doi.org/10.1364/oe.24.005026 (cit. on p. 76).

[81] K. O. Hill et al. "Photosensitivity in optical fiber waveguides: Application to reflection filter fabrication". In: *Applied Physics Letters* 32.10 (May 1978), pp. 647–649. URL: https://doi.org/10.1063/1.89881 (cit. on p. 76).

[82] Christophe Martinez and Pierre Ferdinand. "Analysis of phase-shifted fiber Bragg gratings written with phase plates". In: *Applied Optics* 38.15 (May 1999), p. 3223. URL: https://doi.org/10.1364/ao.38.003223 (cit. on p. 78).

[83] Chaotan Sima. "Integrated planar Bragg grating devices for advanced optical communication systems". PhD thesis. University of Southampton, 2013. URL: http://eprints.soton.ac.uk/id/eprint/359836 (cit. on p. 78).

[84] Rex Bannerman. "Microfabrication of waveguide-based devices for quantum optics". PhD thesis. University of Southampton, 2019. URL: http://eprints.soton.ac.uk/id/eprint/455861 (cit. on pp. 79, 85).

[85] G. Meltz, W. W. Morey, and W. H. Glenn. "Formation of Bragg gratings in optical fibers by a transverse holographic method". In: *Optics Letters* 14.15 (Aug. 1989), p. 823. URL: https://doi.org/10.1364/ol.14.000823 (cit. on p. 80).

[86] *Fiber Bragg Gratings*. Elsevier, 2010. URL: https://doi.org/10.1016/c2009-0-16830-7 (cit. on pp. 80, 84).

[87] P.J. Lemaire et al. "High pressure H2 loading as a technique for achieving ultrahigh UV photosensitivity and thermal sensitivity in GeO2 doped optical fibres". In: *Electronics Letters* 29.13 (1993), p. 1191. URL: https://doi.org/10.1049/el:19930796 (cit. on p. 82).

[88] Tomasz Osuch et al. "Enhancement of spectral response of Bragg gratings written in nanostructured and multi-stepped optical fibers with radially shaped GeOsub2/sub concentration". In: *Optics Express* 28.10 (Apr. 2020), p. 14774. URL: https://doi.org/10.1364/oe.390521 (cit. on p. 82).

[89] C. Sima et al. "Ultra-wide detuning planar Bragg grating fabrication technique based on direct UV grating writing with electro-optic phase modulation". In: *Optics Express* 21.13 (June 2013), p. 15747. URL: https://doi.org/10.1364/oe.21.015747 (cit. on p. 83).

[90] Tae-Jung Ahn, Ji Yong Lee, and Dug Young Kim. "Suppression of nonlinear frequency sweep in an optical frequency-domain reflectometer by use of Hilbert transformation". In: *Applied Optics* 44.35 (Dec. 2005), p. 7630. URL: https://doi.org/10.1364/ao.44.007630 (cit. on p. 88).

[91] Zhenyang Ding et al. "Distributed Optical Fiber Sensors Based on Optical Frequency Domain Reflectometry: A review". In: *Sensors* 18.4 (Apr. 2018), p. 1072. URL: https://doi.org/10.3390/s18041072 (cit. on p. 90).

[92] Chams Baker, Yang Lu, and Xiaoyi Bao. "Chromatic-dispersion measurement by modulation phase-shift method using a Kerr phase-interrogator". In: *Optics Express* 22.19 (Sept. 2014), p. 22314. URL: https://doi.org/10.1364/oe.22.022314 (cit. on p. 93).

[93] K. Kieu et al. "Demonstration of Zeno switching through inverse Raman scattering in an optical fiber". In: *Optics Express* 19.13 (June 2011), p. 12532. URL: https://doi.org/10.1364/oe.19.012532 (cit. on p. 95).

[94] Michał Karpiński et al. "Bandwidth manipulation of quantum light by an electro-optic time lens". In: *Nature Photonics* 11.1 (Nov. 2016), pp. 53–57. URL: https://doi.org/10.1038/nphoton.2016.228 (cit. on p. 97).

[95] Michał Karpiński et al. "Control and Measurement of Quantum Light Pulses for Quantum Information Science and Technology". In: *Advanced Quantum Technologies* 4.9 (July 2021), p. 2000150. URL: https://doi.org/10.1002/qute.202000150 (cit. on p. 102).